# Structural Relaxation and Anisotropic Elasticity of Ordered Block Copolymer Melts

Krista G. Schoonover,<sup>†</sup> Gaurav Rawat,<sup>‡</sup> Emily B. Pentzer,<sup>†,‡</sup> and Michael S. Dimitriyev\*,<sup>‡</sup>

†Department of Chemistry, Texas A&M University, College Station, TX 77843, USA

‡Department of Materials Science and Engineering, Texas A&M University, College

Station, TX 77843, USA

E-mail: msdim@tamu.edu

#### Abstract

Block copolymer (BCP) melts play a critical role in the design of thermoplastics, owing in large part to the creation of alternating nano-scale domains of soft and stiff components. Much of thermoplastic design has been focused on the short-time response associated with the dynamical rigidity of rubbery or glassy chains. However, less attention has been paid to the long-time relaxation and rigidity of microphase separated BCP melts or the role that domain morphology plays in modulating near-equilibrium response. We take advantage of the ability of self-consistent field theory (SCFT) to calculate equilibrium properties of BCP melts to explore the anisotropic elastic response of ordered ABA and AB copolymer melts as quasistatic deformation processes. This allows us to determine the anisotropic stiffness of the liquid crystal-like lamellar and columnar phases due to modulations in domain spacing, as well as the full stiffness tensor of the cubic BCC sphere and double gyroid phases. We explore elastic modulus landscapes for both single grain materials and random polycrystals over architectural

parameters and segregation strengths, using AB diblock and ABA triblock melts as key examples. Finally, we re-examine basic assumptions of BCP melts as simple composites, dependence of melt stiffness on domain spacing, and the role of bridging chain conformations in altering melt relaxation, providing evidence for an interplay between mass transport and domain topology that remains to be understood.

## Introduction

Polymer melts play a central role in the landscape of polymer materials owing to their viscoelastic properties, which largely derive from chain entanglements. Despite their ability to store stress over prolonged timescales, they are essentially polymer liquids and thus ultimately flow under applied stress, with their terminal relaxation determined by the time it takes for polymers to reptate past each other. The essential fluidity of polymer melts creates challenges for blended melts due to the propensity for unlike polymers to undergo phase separation; block copolymers (BCPs) would then play the role of compatibilizers, stabilizing blends such that the melt maintains microscopic interfaces creating complex structure that persists for long times.<sup>2</sup> Meanwhile, BCP thermoplastics take advantage of microphase separation between chemically-distinct blocks, resulting in stable, nano-patterned composites.<sup>3</sup> Moreover, the nanostructure is self-assembled, with domain morphology arising from a careful balance of entropic costs due to chain stretching and enthalpic costs coming from block mixing at the intermaterial dividing surface (IMDS)—the interface between domains. The equilibrium phases are periodic and capable of long range order, with predominant equilibrium phases of lamellae (1D layers), cylinders (2D, often hexagonally-packed), spheres (3D, often arranged on a BCC lattice), and bicontinuous networks, though exceptions exist due to blended additives or different polymer architectures. 4,5 The bicontinuous network phases are of particular interest since they consist of labyrinthine domains and IMDSs that span all of the material volume while maintaining a unit cell with predominantly cubic symmetry. Of the network phases, the double gyroid (DG) phase is the most common, and is thought to be optimal compared with competitor double diamond (DD) and double primitive (DP) phases for linear BCP architectures.<sup>6,7</sup>

The equilibrium phases formed by BCPs mirror those found in assemblies of surfactants as well as small-molecule liquid crystals and conventional crystals. Lamellar structures are stacks of parallel interfaces that resemble a smectic A phase, breaking translational symmetry in one dimension, whereas hexagonal packings of cylinders resemble a columnar phase, breaking translational symmetry in two dimensions. Triply-periodic sphere and network phases break translational symmetry in all three dimensions and are thus structurally similar to crystalline solids. Such "crystalline liquids" have unit cells on the scale of  $10^2 - 10^3$  nm that contain thousands of polymer chains, making them much softer than their atomic and molecular crystal counterparts. While the glass and rubber plateau moduli give the characteristic short-time responses due to slow polymer relaxation and entanglements and have been well-characterized, there are open questions regarding the mechanics and dynamics of BCP melts at terminal timescales. Kossuth, et al.  $^8$  presented a schematic of how BCP melt stiffness changes as a function of timescale, as measured in an oscillatory rheometer (reproduced in Fig. 1(a)). While lamellar (1D) and cylinder (2D) phases are expected to flow over long times, with the cylinder phase characterized by a greater storage modulus (G') than the lamellar phase, the 3D phases retain their rigidity for arbitrarily long time, as long as they are well-ordered. This significant difference can be rationalized by the liquid crystalline structure of the 1D and 2D phases where the liquid behavior dictates the loss of rigidity at long timescales, whereas the 3D phases have crystalline order and thus their rigidity is a fundamental consequence of breaking continuous translational symmetry in all dimensions.<sup>9</sup> Nevertheless, the picture is complicated by the distribution of grain orientations in a "polycrystalline" melt and defect mechanics, 10-19 as well as a recently-reported linear instability of cubic DD under extensional deformation. <sup>20</sup> Beyond such symmetry-based heuristics, little is known about the dependence of this terminal rigidity on polymer composition and architecture, despite the large diversity of suitable systems and interests in thermoplastic design

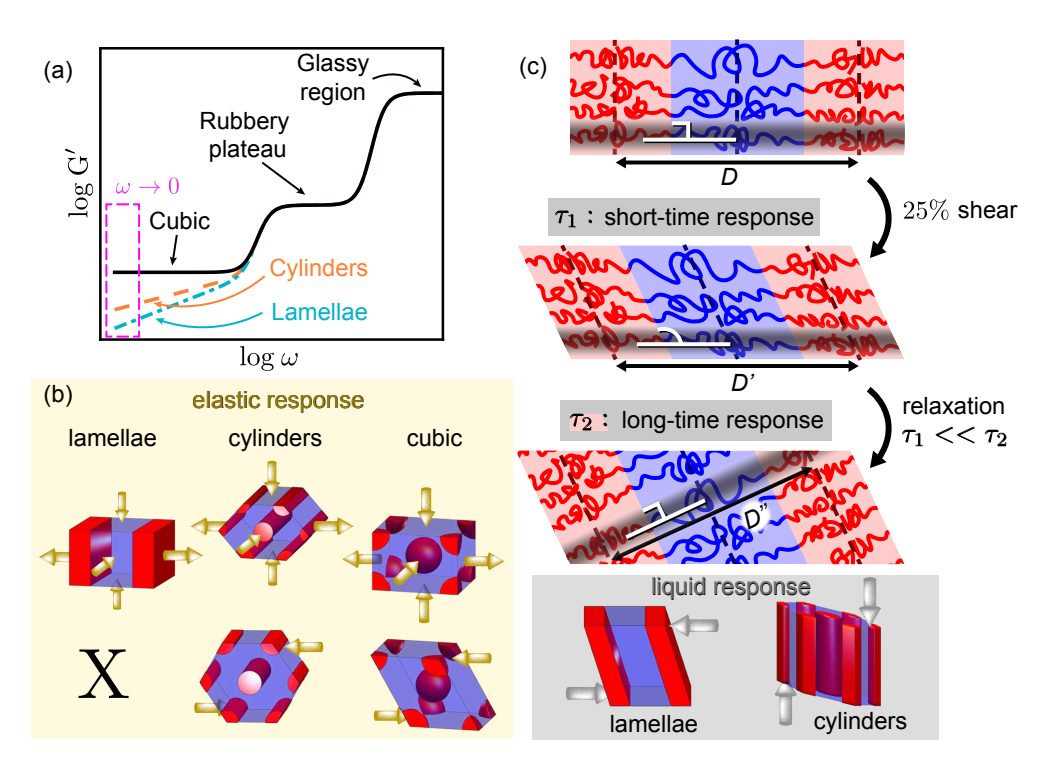


Figure 1: (a) Schematic of relative modulus of different phases for BCPs, this work narrowing in on  $\omega \to 0$ . Anisotropic elasticity is highlighted, showing deformations yielding liquid and elastic responses. (b) The elastic responses under investigation in this work (uniaxial extension and shear). (c) The short and long time response of a shear deformation is shown, highlighting the liquid response for lamellae and cylinders.

for desired applications.

The mechanical design of thermoplastics is often motivated by classic composites where stiff glassy domains are embedded in a soft, rubbery matrix phase. <sup>21</sup> This dynamic rigidity is often at odds with a separate notion of conformational rigidity, which is determined by the Kuhn length  $\ell$ , typically on the order of several to 10s of carbon-carbon bonds (potentially  $10^2$  for certain biopolymers), with key examples including 8.2Å for 1,4-polyisoprene (PI), 9.6Å for 1,4-polybutadiene (PB), 17Å for poly(methyl methacrylate) (PMMA), and 18Å for atactic polystyrene (PS) (see SI Table S1 for a more comprehensive list). <sup>22</sup> For polymers composed of blocks A and B, a conformational rigidity asymmetry parameter  $\epsilon \equiv \ell_A/\ell_B$  designates the relative conformational rigidity of the minority inclusions and majority matrix: for  $\epsilon < 1$ , the A block is stiffer whereas for  $\epsilon > 1$ , the B block is stiffer. <sup>23</sup> Notably, this rigidity describes the infinite time limit response applicable to terminal mechanics, whereas

dynamic rigidity describes the more intuitive short-time response; frequently these responses are inverted, particularly for glassy polymers which tend to have longer Kuhn lengths (lower long-time rigidity) and greater short-time rigidity. Pedagogical BCPs PS-PMMA and PS-PI/PS-PB have elastic asymmetries of about 1 and 2, respectively; in the case of ABA triblock copolymers, the elastic asymmetry changes depending on the block connectivity: for PS-PI-PS,  $\epsilon \approx 2$ , whereas for PI-PS-PI,  $\epsilon \approx 0.5$ , leading to different materials properties. In addition to Kuhn length ratio, the relative amounts of A to B blocks also impact the melt rigidity, where more of the stiffer block yields stiffer overall materials, regardless as to degree of phase separation. <sup>24,25</sup>

Kuhn length also impacts the overall conformation of the polymer, particularly in solution but also in the melt state. Polymer conformations can generally be divided into random coil and rigid rod: the former are typified by a flexible backbone and weak interactions between pendants or side chains (smaller Kuhn length), whereas the latter have some combination of a rigid backbone and bulky or highly interacting pendants or side chains (larger Kuhn length).  $^{26-28}$  In particular, rigid rod polymers may be locked in place by steric bulk of either the backbone or side chains, effectively locking the geometry in place, or have strong interactions between side chains that limit flexibility. More commonly, the rigidity may be conferred by highly conjugated ring systems (termed conjugated polymers), which adopt a planar geometry that prohibits rotational freedom and increases Kuhn length.  $^{29,30}$  A critical number of repeat units (N), typically on the order of at least  $N \sim 10^2 - 10^3$  is required to achieve the desired polymeric properties, from 3D conformation to optical properties to mechanical strength. It is generally more useful to multiply N by the Flory-Huggins interaction parameter  $\chi$  to have a universally applicable segregation strength  $(\chi N)$ , which typically must be greater than 10-15 for microphase separation to occur.

Advancements in synthetic polymer chemistry enable realization of the morphologies described in this Article, as well as more advanced architectures and even greater conformational asymmetry. Controlled polymerizations have enabled the development of well-defined

BCPs, with target molar mass  $(M_n)$  and associated degree of polymerization (N), low dispersity (Đ), and good control over volume fraction of each block as well as block connectivity (i.e., AB vs ABA vs BAB for different monomer types A, B). 31 Most commonly, this synthetic control is used to focus on tailored high  $\chi$  polymers, which enables higher segregation strengths at lower  $N^{32-36}$  or select low  $\chi$  in multiblock copolymers to promote unusual phase behavior and resulting properties.<sup>37</sup> Controlled radical polymerization techniques, including nitroxide-mediated polymerization (NMP), reversible addition-fragmentation chain transfer (RAFT), and atom transfer radical polymerization (ATRP), <sup>38–41</sup> are commonly used to synthesize BCPs via monomers bearing a double bond such that radical polymerization yields a linear all-carbon backbone, typically with pendant groups on every other carbon. More diverse backbone chemistries can be accessed by ring opening polymerization (ROP), in which a cyclic monomer—typically a cyclic lactone or ether—is opened at the electrophilic carbon, embedding an ester or ether group in the carbon backbone. 42,43 A special case of ROP is ring opening metathesis polymerization (ROMP), where a strained cyclic monomer is ring-opened via an embedded double bond. 44,45 The classic example is polynorbornene (PNB), which has a 5-membered ring embedded in the polymer backbone with alternating double bonds which affords enhanced stiffness over a PB counterpart.

The configuration of the double bonds in polymer backbones (i.e., cis or trans) also dictates Kuhn length and physical properties. For example, the conjugated poly(p-phenylenevinylene (PPV), a staple of organic light-emitting diodes (OLEDs) and other electrochemical applications, forms rodlike structures with majority trans double bonds whereas majority cis double bonds leads to more coiled and twisted structures, with each configuration providing unique optical properties. <sup>46</sup> Another class of organic electronic materials are conjugated ladder polymers, which can achieve Kuhn lengths of over 300 nm when fully protonated, but only 13 nm when neutral. <sup>47</sup> Indeed, engineering Kuhn length has been shown to produce unexpected ductility in semiflexible polymer glasses, as Kuhn lengths on the scale of entanglement length allow the polymer to stretch during deformations, as demonstrated by

molecular dynamics simulations. 48

In this Article, we examine how the terminal rigidity of ordered BCP melts are afforded by conformational rigidity asymmetry  $(\epsilon)$ , polymer sequence (ABA vs. AB), and the microphase separated pattern (see Fig. 1). By using SCFT to calculate equilibrium properties of BCP melts, we extract the terminal moduli for lamellar, cylindrical, BCC sphere, and network (i.e., double gyroid) phases of symmetric ABA melts. We show that the stiffness of these melts depart from intuition provided by standard composite theory, i.e., the rule of mixtures. Instead, the extracted moduli show a non-monotonic dependence on composition, with effects arising from both nanoscale patterning and block sequence. The block sequence dependence is rationalized though the domain structure of phase separated melts, wherein ABA molecules can possess both "bridging" conformations that join neighboring minority inclusions through the majority matrix, as well as "looping" conformations. We calculate the polycrystalline average shear moduli, establishing upper (Voigt) and lower (Reuss) bounds for each phase, <sup>49-51</sup> providing a hierarchy of expected moduli and confirming that while 1D and 2D phases have vanishing lower bound moduli, the 3D phases have non-zero lower bounds. By comparing with analogous AB diblock systems with comparable domain spacing, we demonstrate that while both architectures exhibit a similar range of terminal moduli, there are small, yet significant differences. We explore how bridging and looping conformations alter the material stiffness, finding a non-intuitive softening effect arising from bridging conformations. Our results lead us to conclude that both interface shapes and interactions between domains that are mediated by chain behavior near inter-domain slip surfaces (also known as "terminal boundaries" <sup>52</sup>) are key for understanding and engineering the long-time response of BCP melts.

# Terminal rigidity of neat melts

The "terminal rigidity" of BCPs is inherently different from unstructured melts or blends. For homopolymer melts, tensile stress elongates and aligns chains, creating internal stresses that are relieved over the disentanglement timescale.<sup>53</sup> Such melts retain essentially disordered arrangements after relaxing to an equilibrium state: the free energy per chain remains unchanged. By combining multiple chemically-distinct monomers (A vs B), the equilibrium free energy acquires a free energy of mixing  $F_{\rm mix}$  contribution. It is variations to the free energy of mixing that can give rise to rigidity for arbitrarily long times. For polymer blends, the equilibrium state consists of macrophase separated homopolymer domains, where each macroscopic domain has a locally vanishing free energy of mixing. In this case,  $F_{\rm mix} \approx \gamma A$ , where  $\gamma$  is an interfacial free energy density and A is the interfacial area; in equilibrium, the interfacial area is minimized. The only way for deformations to change the equilibrium mixing free energy of a blend is if the area of the interface between immiscible components increases even after relaxation. Regardless if this can be achieved, the deformation free energy  $\Delta F_{\text{mix}}$  would still scale with interface area and thus be sub-extensive with system size, so that any measured stiffness would not be a bulk property of the melt. By contrast, microphase separated melts involve a mixing free energy that is extensive with system size:  $F_{\rm mix} \sim V$ , where V is the melt volume. If the equilibrium state of the melt corresponds to a stable minimum of the free energy of mixing, then any deformation from that equilibrium state will raise the value of  $F_{\text{mix}}$ ; within the linear response approximation, the change in free energy is given by

$$\Delta F_{\text{mix}} = \frac{1}{2} V C_{ijk\ell} u_{ij} u_{k\ell} , \qquad (1)$$

where  $C_{ijk\ell}$  is the linear elastic modulus tensor and  $u_{ij}$  are components of the macroscopic strain tensor **u**. Since the melt is taken to be incompressible, any change in volume must accompany a change in the number of polymer chains within that volume. By considering deformations such that the trace of the strain tensor vanishes (tr **u** = 0), we only consider deformations that maintain a fixed melt volume, fixing the number of chains as expected for a realistic polymer melt.

The question of whether a phase is at a stable free energy minimum can be, to some degree, addressed through the symmetry of the phase in question, namely whether it has directions of continuous translational symmetry. For the 1D lamellae, translational symmetry is broken in one dimension, leaving two symmetric directions along which we expect liquid-like behavior; for 2D cylinders, there is only one remaining translationally-symmetric direction. The 1D and 2D phases are therefore stable with respect to deformations that change their D-spacing, but lack rigidity under certain deformations, resulting in certain zero-valued components of the linear elastic stiffness tensor  $C_{ijk\ell}$ . The intuition behind this is exemplified in Fig. 1(c). As shown, shearing a lamellar structure will tilt chains relative to the IMDS for short times, incurring an entropic penalty. Over long times, if allowed, the chains will flow, re-orienting the IMDSs such that the net effect of the deformation is a rotation of the melt. Since it is possible for the initial D-spacing to be equal to its relaxed value D'', such a shear deformation can be performed without increasing the free energy per chain; thus the lamellar phase lacks a terminal shear rigidity but has a terminal extensional rigidity.

To compute the stiffness tensor components  $C_{ijk\ell}$  for each phase, we take advantage of the ability of SCFT to rapidly calculate the equilibrium mixing free energy per chain. It does this by solving the single-chain partition function within a mean field approximation where the chemical potential is self-consistently determined by single-chain conformations.<sup>5,54</sup> Since this method immediately produces equilibrium predictions, it overcomes the time constraints on molecular dynamics approaches to simulating equilibrium states. Moreover, advances in computing methods, particularly through the use of Anderson acceleration implemented in the open-source PSCF software, <sup>55</sup> have made rapid iteration over multiple phases, polymer architectures, and compositions feasible. Thus, while prior work has either focused on lamellae, <sup>56–59</sup> cylinders, <sup>60</sup> or 3D phases <sup>8,61</sup> for single polymer architectures, we opt to con-

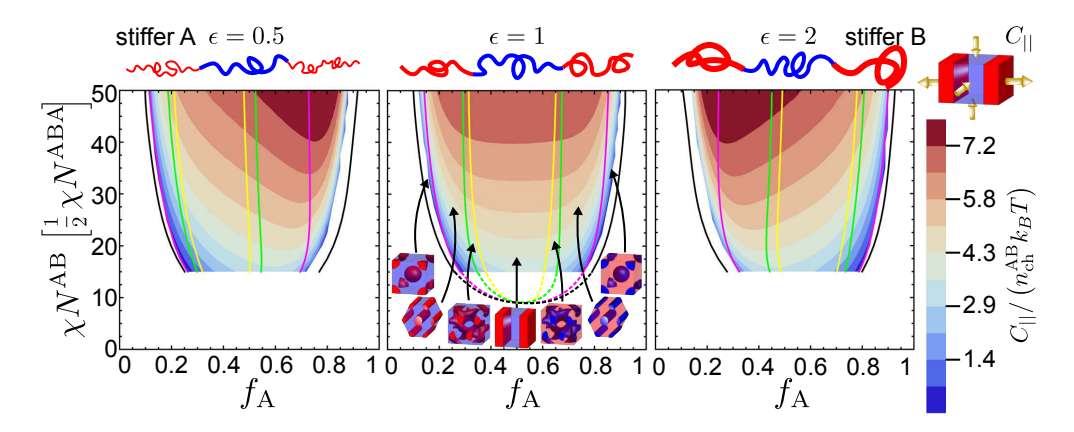


Figure 2: Modulus heat map for 1D lamellar phase for three elastic asymmetries, plotting full region of metastable lamellar phases overlaid by phase diagrams, where the lamellar stability window is between the yellow lines.

sider a more extensive set of structures and molecular parameters. Recently, SCFT-imposed quasistatic deformations were used to study non-affine relaxation modes in bicontinuous networks<sup>62</sup> and demonstrate the instability of cubic DD under extensional strain.<sup>20</sup>

In our approach we first determine the equilibrium unit cell lattice parameters for a symmetric reference structure, then choose a strain protocol, update the lattice parameters, and finally iterate the SCFT equations until the residual error is minimized, obtaining a mixing free energy at fixed strain. The elastic moduli are then determined by fitting a quadratic form to  $\Delta F(\mathbf{u})$ , giving  $\Delta F$  in units of  $n_{\rm ch}k_{\rm B}T$ , where  $n_{\rm ch}=\rho/N$  is the chain density with  $1/\rho$  representing the volume occupied by a statistical segment and N the degree of polymerization. This procedure is discussed in greater detail in SI Section S1. As established in prior studies, we represent symmetric ABA copolymers as "doubled" AB copolymers. Consequently, the degree of polymerization  $N^{\rm ABA}$  for ABA copolymers is taken to be twice that of AB diblocks, i.e.,  $N^{\rm ABA} = 2N^{\rm AB}$ . If the segment density  $\rho$  of both situations is identical, then the density of ABA chains is taken to be half the density of AB chains, i.e.,  $n_{\rm ch}^{\rm ABA} = n_{\rm ch}^{\rm AB}/2$ . This representation allows us to directly compare ABA triblocks to analogous systems of AB diblocks.

### 1D: Lamellar rigidity

For equilibrium lamellar morphologies, the free energy per chain is only a function of the lamellar spacing D; this spacing is determined from the 1D lattice parameter a. Orienting the lamellae along the z-axis, the free energy is given by

$$\Delta F_{\text{mix}} = \frac{1}{2} V C_{||} u_{zz}^2 \tag{2}$$

where  $C_{\parallel}$  describes the longitudinal rigidity of the lamellae and  $u_{zz} = \Delta a/a_0$  is the layer strain. This follows the form of layer elasticity for smectic A liquid crystals, neglecting layer bending,  $^{56,63-65}$  which would require implementation of strain-gradient terms.  $^{66}$  This free energy has an implicit dependence on additional strain components through the incompressibility constraint, tr  $\mathbf{u} = 0$ .

Figure 2 shows the longitudinal modulus  $C_{\parallel}$  plotted as a heat map overlaid on the phase diagram for conformationally symmetric ( $\epsilon=1$ ) and asymmetric ( $\epsilon=0.5,2$ ) cases (independent phase diagrams for ABA shown in SI Figure S1), with SI Figure S2 showing only those regions where lamellae are the most stable phase. Focusing first on the conformationally symmetric case ( $\epsilon=1$ ), we find that the layer stiffness is predominantly determined by  $\chi N$  with little variation with A-block fraction  $f_A$  within the stability window (between the yellow lines). By contrast, conformational asymmetry introduces significant dependence on  $f_A$ , where the greater volume fraction of the stiffer block is stiffer (i.e., high  $f_A$  is stiffer for stiffer A block,  $\epsilon < 1$ ). This monotonic dependence is can be approximated by the rule of mixtures, namely  $C_{\parallel} \sim f_A C_{\parallel}^A + (1-f_A)C_{\parallel}^B$  for suitably extrapolated values of  $C_{\parallel}^A$  and  $C_{\parallel}^B$ , within the lamellar region of the phase diagram. It is interesting to note that the stiffer regions are metastable structures for  $\epsilon \neq 1$ , where there is a greater volume of the stiffer block. This has implications for deformation-induced ordering, for example shear-induced alignment could result in greater long-time rigidity materials.

Comparing modulus diagrams for ABA and AB as illustrated in SI Figure S3, we see that

the general shape and contours of the modulus heat maps are very similar for both ABA and AB, requiring a narrower focus to elucidate differences. Taking a slice at  $\chi N^{AB} = 30$  allows us to compare trends in modulus and free energy across  $f_A$  (see SI Figure S4). ABA triblocks have a slight asymmetry for  $\epsilon = 1$ , with both phase diagram and modulus heat map being slightly offset to the right (higher  $f_A$ ), whereas they are symmetric about  $f_A = 0.5$  for AB diblocks. The longitudinal modulus is greater for ABA than AB with respect to  $f_A$  for all  $\epsilon$ , with minimal difference for  $\epsilon = 0.5$  except for the highest  $f_A$ , and increasing difference with increasing  $\epsilon$ .

Comparing the maximum longitudinal moduli for  $\chi N^{\rm AB}=30$ , we see that both ABA and AB are stiffer for  $\epsilon\neq 1$  by about 10% compared to  $\epsilon=1$ . For ABA, the longitudinal modulus at  $\epsilon=2$  is greater than that at  $\epsilon=0.5$  by about 1%, and the  $f_{\rm A}$  at maximum modulus is further from that at  $\epsilon=1$ . These results indicate that longitudinal modulus for lamellae is more strongly impacted by having stiffer bridging chains ( $\epsilon=2$ ) than stiffer matrix. For AB, the longitudinal modulus is symmetric about  $f_{\rm A}=0.5$  for  $\epsilon=1$  and mirrored for  $\epsilon=0.5$  and 2, respecting the invariance of melt properties under simultaneous exchange of Kuhn lengths  $\ell_{\rm A}\leftrightarrow\ell_{\rm B}$  and A-block fraction  $f_{\rm A}\leftrightarrow f_{\rm B}(=1-f_{\rm A})$ . Additionally, AB moduli are less than those of ABA when normalized by chain density, indicating that doubling  $\chi N$  for ABA compared to AB does not account for the entire difference between the two. Values of  $C_{\rm ||,max}$  and their associated  $f_{\rm A}$  at each  $\epsilon$  for all  $\chi N$  are recorded for ABA and AB in SI Tables S3-4, with a graphical representation depicted in SI Figure S5. The trends discussed for  $\chi N^{\rm AB}=30$  are representative for all  $\chi N$ , with greater  $C_{\rm ||,max}$  for greater  $\chi N$ , located at  $f_{\rm A}$  further from 0.5.

Now consider  $C_{\parallel}$  as a function of  $\chi N$  at fixed  $f_{\rm A}$  (see SI Figure S6), effectively a vertical slice through Figure 2. As discussed in the case of  $\chi N^{\rm AB}=30$ , ABA and AB are both relatively symmetric across  $f_{\rm A}=0.5$  for sufficiently large  $\chi N^{\rm AB}$  at  $\epsilon=1$ , with lines of  $C_{\parallel}$  vs  $\chi N^{\rm AB}$  collapsing for  $f_{\rm A}=0.3,0.5,0.7$ . For  $\epsilon\neq 1$ , the rule of mixtures is generally followed, where stiffness increases with increasing volume fraction of stiff block. Directly comparing

Table 1: Maximum modulus, normalized to units of  $n_{\rm ch}^{\rm AB}k_BT$ , and associated  $f_{\rm A}$  for the given  $\epsilon$  and  $\chi N$  for ABA and AB lamellae.

	ABA $(\chi N = 60)$		$AB (\chi N = 30)$	
$\epsilon$	$C_{  }$	$f_{ m A}$	$C_{  }$	$f_{ m A}$
0.5	5.84	0.71	5.58	0.67
1.0	5.29	0.53	5.07	0.50
2.0	5.90	0.32	5.58	0.33

 $\epsilon$  for a given  $f_A$  shows that the modulus for both ABA and AB remains comparable for all  $\chi N^{AB}$  for  $f_A = 0.5$ , an interesting result given that  $f_A = 0.5$  is on the edge of the stability window for  $\epsilon \neq 1$ . This indicates that having equal volume fractions of the terminal (A) and bridging (B) blocks counteracts the impact of block stiffness with regard to modulus. Alternatively, low  $f_A$  moduli increase from  $\epsilon = 0.5$  to 1 to 2, whereas high  $f_A$  increase from  $\epsilon = 2$  to 1 to 0.5, although some fluctuations occur for low  $\chi N^{AB}$ . Interestingly, regardless as to data separation method (grouped by  $f_A$  for a given  $\epsilon$  or grouped by  $\epsilon$  for a given  $f_A$ ), we find consistency with the expectation from strong-segregation theory  $\epsilon$ 0 that the modulus scales with  $(\chi N^{AB})^{1/3}$  for high enough segregation strengths.

# 2D: Columnar rigidity

The cylindrical (columnar) phase has 2D hexagonal symmetry, so is crystal-like in the plane of the cylinders and liquid-like parallel to the cylinders. Since the elasticity description of 2D materials with hexagonal symmetry is equivalent to that of isotropic materials, the deformation free energy of mixing is simply

$$\Delta F_{\text{mix}} = \frac{1}{2} V \left[ 2\mu_{\perp} (u_{xx}^2 + u_{yy}^2 + 2u_{xy}u_{yx}) + \lambda_{\perp} (u_{xx} + u_{yy})^2 \right]$$
 (3)

where  $\mu_{\perp}$  is the transverse shear modulus and  $\lambda_{\perp}$  is the transverse Lamé parameter.<sup>68</sup> Expressing this in terms of volume-preserving uniaxial deformation along the longitudinal di-

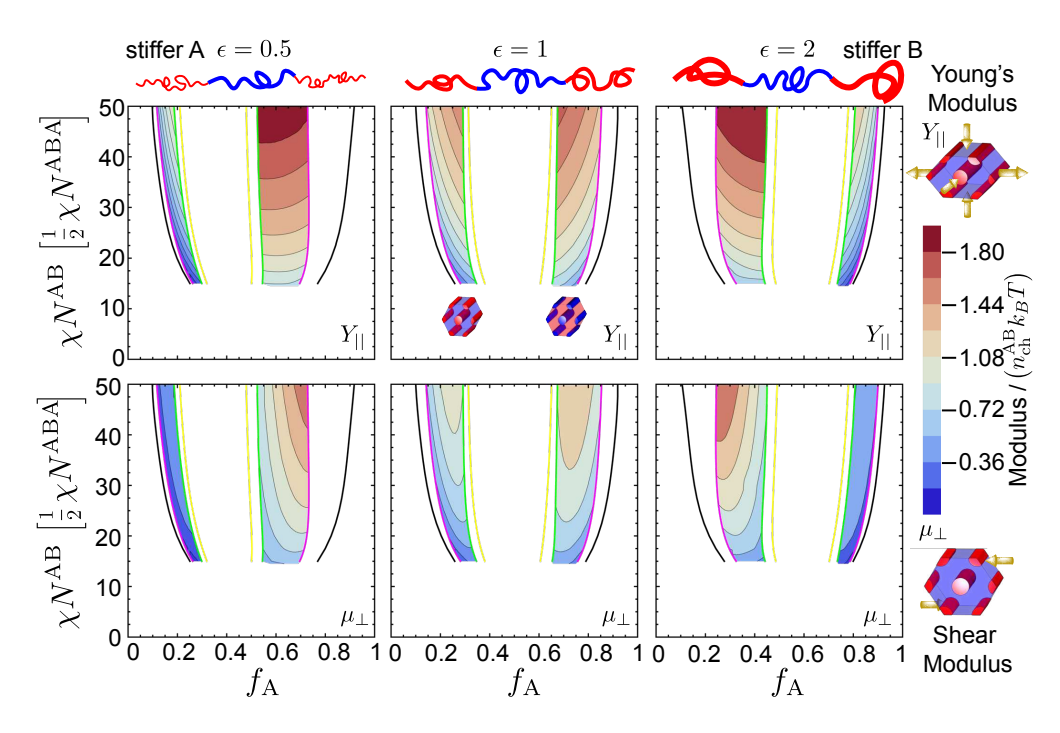


Figure 3: Modulus heat map for 2D hexagonal cylinder phase for three elastic asymmetries for stable phase region, comparing Young's modulus (top) to shear modulus (bottom).

rection, the volume constraint implies that  $u_{xx} + u_{yy} = -u_{zz}$  so we can re-express the free energy in terms of a longitudinal Young's modulus  $Y_{\parallel}$  as

$$\Delta F_{\text{mix}} = V \left( \frac{Y_{\parallel}}{2} u_{zz}^2 + 2\mu_{\perp} u_{xy} u_{yx} \right) , \qquad (4)$$

where  $Y_{\parallel} \equiv \mu_{\perp} + \lambda_{\perp}$ , such that under an applied stress  $\sigma_{zz}$  along the z-axis, we recover the extensional stress-strain relationship  $\sigma_{zz} = Y_{\parallel}u_{zz}$ . To determine these parameters, we used two separate deformation protocols applied to a unit cell of the hexagonal cylinder phase. The first protocol increases the lattice parameter a while fixing b and  $\theta (= 2\pi/3)$ to be constant. The second protocol was an isotropic biaxial stretch of parameters a and b, effectively "swelling" the in-plane dimensions. Due to translational symmetry along the z-axis (i.e., the c axis), while these deformations change the cross-sectional area, the total volume can be preserved by freely re-scaling the height of the 3D unit cell, without altering the free energy per chain. As shown in SI Section S2, these two protocols provide enough information to determine  $Y_{\parallel}$  and  $\mu_{\perp}$ .

Modulus heat maps for Young's and shear modulus ( $Y_{\parallel}$  and  $\mu_{\perp}$ , respectively) are shown in Figure 3, plotted only in their stable phase regions, with moduli for metastable results shown in SI Figure S7. Shear moduli have local maxima with respect to slices at various  $\chi N$  within the stability window for  $\epsilon = 1$ , and local maxima on the phase boundary for  $\epsilon \neq 1$ , as illustrated in SI Tables S5-8. As with lamellae, the stiffest regions correspond to greater volume fraction of the stiffer block. For 2D and later 3D phases, we introduce the variable of matrix vs filler component; for the columnar phase, the stiffest response is achieved when the stiffer block is the matrix.

Considering both SI Figure S8 and SI Table S5, we can see that  $f_A$  at  $\mu_{\perp,\text{max}}$  ( $f_{A,\text{max}}$ ) is very similar for both ABA and AB, differing by only up to 0.03.  $f_{A,\text{max}}$  occurs at the same or very similar values for  $\epsilon = 1$  and 2 for B matrix (low  $f_A$ ), and the same  $f_A$  for  $\epsilon = 0.5$  and 1 for A matrix (high  $f_A$ ). While  $Y_{||}$  is greater for ABA than AB for  $\chi N^{AB} = 30$  for nearly all  $f_A$  and  $\epsilon$  (as was the case for lamellae),  $\mu_{\perp}$  is only greater for ABA for A matrix regions (all  $\epsilon$ ) and for  $\epsilon = 2$  for B matrix (see SI Figure S9). This indicates an unexpected "softness" of the ABA system relative to the AB system, which we explore further in the Discussion section.

Both shear and Young's moduli are smaller for columnar phase than the extensional modulus for lamellae. This can be rationalized by the variability of chain orientation that exists for the cylindrical melt: while the lamellar extensional modulus describes the stiffness of the melt when layer spacing is strained, the strain applied to the cylindrical phase involves stretching only subset of chains. As shown in SI Figures S10-11 the lamellar stiffness is approached under biaxial (i.e., transverse-isotropic) deformations of the cylinder phase, when all chain orientations are subject to the same strain. Such effects of directional variation will be revisited in our discussion of polycrystalline averages.

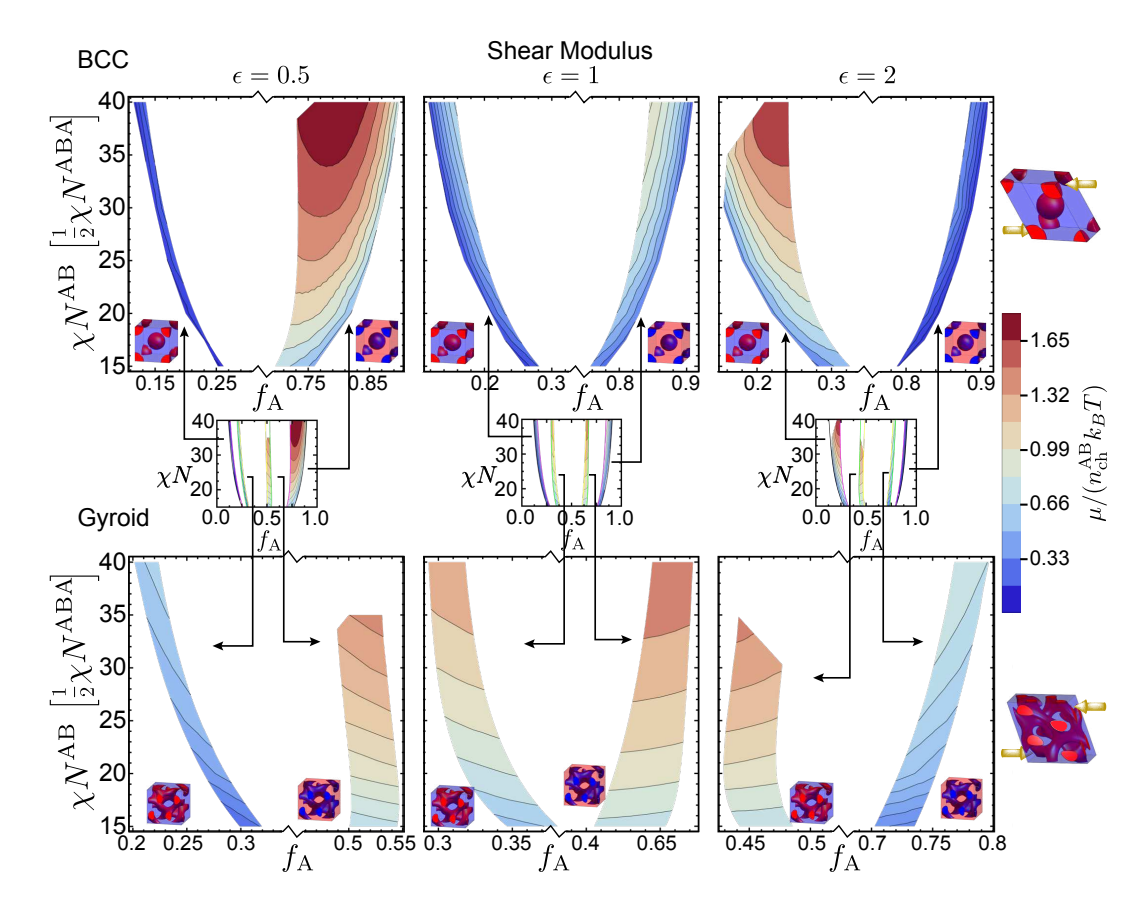


Figure 4: Modulus heat map for 3D cubic phases for three elastic asymmetries for stable phase region, highlighting shear modulus for BCC (top) and gyroid (bottom).

## 3D: Cubic rigidity

The deformation free energy per chain for 3D cubic structures can be written as

$$\frac{\Delta F_{\text{mix}}}{V} = \frac{Y}{9} \left( (u_{xx} - u_{yy})^2 + (u_{yy} - u_{zz})^2 + (u_{zz} - u_{xx})^2 \right) 
+ 2\mu \left( u_{xy} u_{yx} + u_{yz} u_{zy} + u_{zx} u_{xz} \right) ,$$
(5)

where the bulk modulus is excluded due to the volume constraint (constant volume bulk moduli are undefined). While this is not an isotropic system, we define Y as an effective Young's modulus, chosen such that under uniaxial stress  $\sigma_{zz}$ , the stress-strain relation is  $\sigma_{zz} = Yu_{zz}$ ; similarly  $\mu$  is a shear modulus. These moduli are calculated using a pair of deformation protocols, where protocol (i) is a volume-preserving uniaxial strain and protocol (ii) is a volume-preserving simple shear; see SI Section S1 for more details. Notably, there

are no "liquid directions" for cubic structures—these 3D phases obey the rules of crystal elasticity rather than liquid crystal elasticity. Rather, the liquid response gives rise to nonaffine internal rearrangements, captured with a "liquid network" description <sup>62</sup> that is distinct from the liquid crystal behavior of the lamellar and columnar phases. These deformations were performed on  $\chi N^{ABA} = 30 - 80$  in increments of 10 with  $f_A$  spacings of 0.02 - 0.04, or 0.01 for high interest regions (i.e., within stable phase windows). Shear moduli for BCC spheres and double gyroid network phases within their stability windows are plotted in Figure 4 on condensed  $f_A$  axes, with Young's moduli plotted in SI Figure S12. Heat maps plotted on the full  $f_A$  axis can be found in SI Figure S13 for a to-scale comparison, and metastable moduli are shown in SI Figures S14-15. Note that the Young's modulus is found to be less than the shear modulus  $(Y/\mu < 1)$  for this system. For 3D isotropic materials  $Y/\mu = 2(1 + \nu)$  for Poisson ratio  $\nu$ , so  $Y/\mu < 1$  would imply an auxetic response. We emphasize that this bound does not hold for our calculations owing to the constant volume (isochoric) conditions under which the moduli are calculated; under these conditions the Poisson ratio is not defined.

For  $\epsilon=1$ , gyroid had higher moduli than BCC, and in both cases, the stiffness is larger for the case of an A-block matrix (the "inverted" structures with  $f_A \gtrsim 0.5$ ) than the case of a B-block matrix (structures with  $f_A \lesssim 0.5$ ). Interestingly, whereas the moduli for gyroid have little variation with  $f_A$ , there is a strong variation of the BCC moduli with  $f_A$ . This is likely due to the proximity of the BCC structures to the disordered phase, where the response of the melt to applied deformations can destroy the ordered phase. Indeed, we find that the modulus drops rapidly for all phases as their composition reaches the edge of the range for which ordered solutions to the SCFT calculations were found, hinting at loss of stability of the ordered phases. This is particularly true for all Y, and for  $\mu$  for  $\epsilon=1$  and the smaller portion of phase diagram for  $\epsilon\neq 1$  (B matrix for  $\epsilon=0.5$ , A matrix for  $\epsilon=2$ ). For BCC, the values of  $\mu$  for  $\epsilon\neq 1$  find distinct maxima within the stable phase region whenever the matrix block is stiffer than the minority block (see SI Tables S9-11 and SI Figure S16);

similar trends can be seen in the shear modulus of the cylinder phase (i.e., the shape of the  $\mu$  heat map is comparable for both columnar and cubic phases). The maxima for gyroid  $\mu$  are less well defined due to the narrow phase stability window, although when extending the calculations into metastable regions, we were able to locate distinct maxima for each  $\chi N$  (see SI Tables S12-14 and SI Figure S17). Note that our calculations for the gyroid phase encountered convergence issues for  $\epsilon \neq 1$ , particularly for structures with a stiffer matrix block.

As with the columnar phase, ABA moduli show similar trends as AB moduli, although there is a slight asymmetry where the moduli are shifted to slightly higher values with increasing  $f_A$ . For both gyroid and BCC, Young's moduli are greater for ABA than AB at  $\chi N^{AB} = 30$ , and shear moduli are greater for A matrix for all  $\epsilon$  and also B matrix for  $\epsilon = 2$  (see SI Figures S18-19). Interestingly, the magnitude of the moduli is on a similar scale to columnar phases, and about 1/4 that of lamellae. Since cubic structures are expected to be the stiffest, this demonstrates that ideal structures without defects or different orientations produce different results than intuitive expectations. This can be adjusted for by taking polycrystalline averages, as discussed below.

# Discussion

#### Rule of mixtures for 1D lamellae

The mechanics of BCP melts are often understood in the context of composites: a rubbery block and a glassy block respectively correspond to the soft and hard components of a composite. Accordingly, it is expected that the macroscopic stiffness of the material can be represented as an average over the stiffnesses of the component blocks. In the case of a 1D lamellar phase, the layers are stretched in series, and thus one might consider that the layers are under an isostress condition. However, due to the local volume balance constraint, in straining the interlayer spacing from D to D', the A-block subdomain is strained from

 $f_{\rm A}D$  to  $f_{\rm A}D'$ , so the B-block subdomain must be strained from  $(1-f_{\rm A})D$  to  $(1-f_{\rm A})D'$ . Therefore, the lamellar phase is in an isostrain condition under longitudinal deformations, and thus it is expected that the longitudinal modulus obey the rule of mixtures, namely  $C_{\parallel} \approx C_{\rm A} f_{\rm A} + C_{\rm B} (1-f_{\rm B})$ , where  $C_{\rm A}$  and  $C_{\rm B}$  are the pure-A block and pure-B block moduli, respectively.

In order to approximate the single-block stiffnesses  $C_{\alpha}$  (for  $\alpha=A,B$ ), we turn to strong-segregation theory (SST) for AB diblocks, which is the asymptotic limit of SCFT when  $\chi N \to \infty$ .<sup>67</sup> Here, the IMDS is taken to be infinitely narrow, so that the enthalpic cost of mixing is  $H_{\text{mix}} = \gamma A = 2\gamma V/D$ , where A is the IMDS area and is a surface free energy, and V = AD is the unit cell volume. The single-block subdomains are then approximated as polymer brushes and the stretching free energy cost is computed using parabolic brush theory, yielding  $F_{\text{str.},\alpha} = (\pi^2/32)n_{\text{ch}}k_BTD^2f_{\alpha}^3/(N_{\alpha}\ell_{\alpha}^2)$ , where  $N_{\alpha}$  is the degree of polymerization and  $\ell_{\alpha}$  is the Kuhn length of block  $\alpha$ . As shown in SI Section S4, the longitudinal modulus can then be expressed as

$$C_{\parallel}^{\text{SST}} = \frac{4\gamma}{D} + 2\kappa \frac{D^2}{N\ell_{\text{A}}^2} f_{\text{A}} + 2\kappa \frac{D^2}{N\ell_{\text{B}}^2} (1 - f_{\text{A}}) , \qquad (6)$$

where  $\kappa \equiv (\pi^2/32) n_{\rm ch} k_B T$ . Note that the last two terms have the form of a rule of mixtures, where the entropic stiffness of a polymer with degree of polymerization N and Kuhn length  $\ell_{\alpha}$  is given by  $\kappa D^2/(N\ell_{\alpha}^2)$ . While the entropic stiffness of Gaussian chains that appears in Flory's theory of rubber elasticity scales with  $R^2/(N\ell^2)$ , where R is the separation length of chain ends, parabolic brush theory allows for a variety of chain ends to be sampled, so that this length is re-expressed as the domain spacing D, along with a numerical prefactor. Importantly, the stiffness of microphase separated domains acquires an additional dependence on the effective enthalpy of mixing, as represented by the first term. This describes how volume-preserving deformations that extend the domain spacing D must also decrease the area A of the IMDS. As the interface is always assumed to exist within SST, regardless of

 $f_{\rm A}$ , this term falls outside of the rule of mixtures.

For comparison with the SCFT results where the domain spacing D is unconstrained, chosen such that the free energy of mixing is minimized, we solve for the equilibrium spacing, yielding a new expression for the equilibrium longitudinal stiffness,

$$C_{\parallel}^{\text{SST}}\big|_{D^*} = \kappa^* \times \left[ \sqrt{N\ell_{\text{A}}^2} \sqrt{N\ell_{\text{B}}^2} \left( \frac{f_{\text{A}}}{N\ell_{\text{A}}^2} + \frac{1 - f_{\text{A}}}{N\ell_{\text{B}}^2} \right) \right]^{1/3}$$
$$= \kappa^* \times \left( \frac{f_{\text{A}}}{\epsilon} + \epsilon (1 - f_{\text{A}}) \right)^{1/3} , \tag{7}$$

where  $\kappa^* \equiv \left(\frac{9\pi^2}{8}\right)^{1/3} n_{\rm ch} k_B T(\chi N)^{1/3}$ . Note that the rule of mixtures, based on a simple arithmetic average of block stiffnesses, is absent in its usual form. Instead, there is a weighting factor that depends on the geometric average of Kuhn lengths, arising from the enthalpic cost of interaction between chains. 54,69 This combination acquires a nonlinearity—the cube root—that accounts for the effect of changes in equilibrium spacing based on the balance of interfacial enthalpy and entropic costs of chain stretching. This new average can be expressed completely in terms of  $f_{\rm A}$  and the conformational asymmetry  $\epsilon$ . Despite the loss of the traditional rule of mixtures, we still find a monotonic dependence of the melt stiffness with  $f_{\rm A}$  at fixed  $\epsilon$ . However, the nonlinearity of this relationship points to parameter regions where relatively large changes in melt stiffness can be achieved with small changes in  $f_A$ ; this is particularly true for cases of large conformational asymmetry  $\epsilon \gg 1$  or  $1/\epsilon \gg 1$ . Importantly, the stiffness of the melt is expected to be constant with  $f_A$  for  $\epsilon = 1$ , which is consistent with SCFT measurements within the stability range for lamellae; the SST predictions fail as the phase loses stability or approaches the order/disorder transition. While this result was derived for AB diblock copolymer melts, the key takeaways should hold for ABA melts as well; as we show below, however, the presence of bridging chains can dramatically alter melt stiffness, particularly in non-lamellar melts. Finally, note that the overall prefactor  $\kappa^*$ accounts for the usual scaling with chain density and temperature, along with a factor of  $(\chi N)^{1/3}$ ; as shown in SI Figure S6, our SCFT results are consistent with this scaling for high

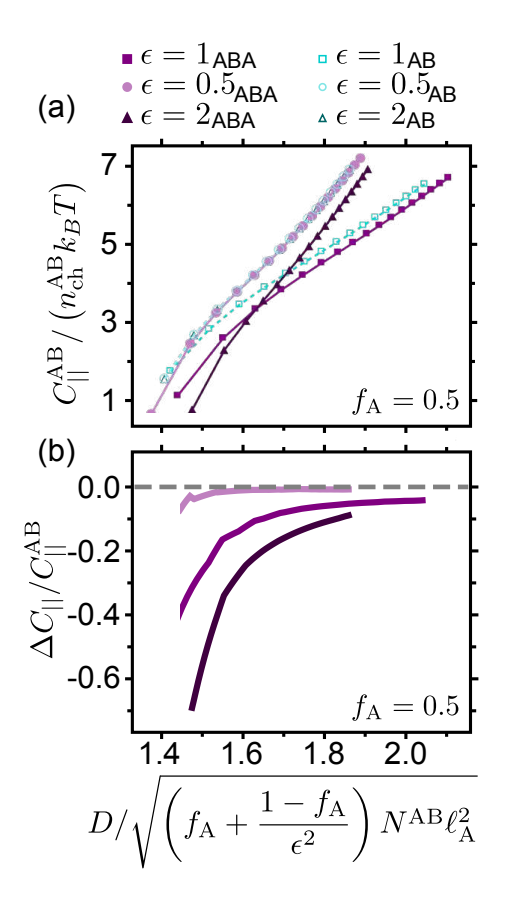


Figure 5: (a) Plot showing the scaling of longitudinal modulus with domain spacing for lamellae at  $f_A = 0.5$ , with domain spacing normalized by  $\epsilon$  and  $f_A$ . (b) Plot showing the percent difference between  $C_{||}$  for ABA and AB, where  $\Delta C_{||} = C_{||}^{ABA} - C_{||}^{AB}$ .

enough segregation strengths.

## Domain spacing

It is widely accepted that the D-spacing of a BCP melt plays a key role in determining the melt's stiffness. <sup>70</sup> In general, ABA and AB melts can have different D-spacings at equivalent molecular parameters and segregation strengths. To assess the degree to which additional contributions arising from polymer architecture may affect melt stiffness, we compare ABA and AB melts as a function of D. The D-spacing is determined in units of the RMS radius of the polymer coil,  $\sqrt{(f_A + (1 - f_A)/\epsilon^2) N^{AB} \ell_A^2}$ . The longitudinal modulus for lamellae is plotted with respect to normalized D-spacing for  $f_A = 0.5$  (Figure 5(a), see SI Figure S20 for  $f_A = 0.3, 0.7$ ). We find that the longitudinal modulus monotonically increases with D

for the range of  $\chi N$  values sampled, consistent with expectations of eq. 6. Interestingly, the longitudinal modulus is consistently greater for AB than ABA with respect to D for all  $\epsilon$  as clearly demonstrated in Figure 5(b). Our results show that the stiffness comparisons between ABA and AB melts require care: if compared at fixed  $\chi N$ , ABA melts are stiffer, whereas AB melts are stiffer when compared at fixed D-spacing. The key difference between ABA and AB melts is the presence of the middle B block, which we can regard as a cross-linking site between the ends of two B blocks for a pair of AB chains. This added constraint should affect chain packing statistics and thus melt thermodynamics. This is confirmed by the fact that the difference in melt stiffness is greatest for  $\epsilon > 1$ , when the B block is stiffer than the A block, magnifying differences in chain stretching costs. Meanwhile, the difference is minimized for  $\epsilon < 1$ , when the A block is stiffer; since the A block is identical for ABA and AB systems, the difference in comparative melt stiffness approaches zero. Further, note that the difference in melt stiffness seems to approach zero as the D-spacing becomes large. Since the D-spacing increases with  $\chi N$ , this points to key differences in melt stiffness arising from finite segregation effects.

## Polycrystalline Averages

While we report the anisotropic elastic moduli for perfect grains of each of the canonical equilibrium linear BCP phases, real materials are polycrystalline, containing multiple grain orientations, as well as defects such as dislocations and grain boundaries. <sup>10–19</sup> The terminal mechanics of real systems ultimately depends on the statistics of grain orientation and defect distributions, which in turn depends on material processing. Moreover, the scale of the SCFT computations required to capture these behaviors is prohibitive, although progress has been made in the cases of lamellar and cylindrical phases. <sup>71–73</sup> Nonetheless, we can obtain upper and lower bound estimates of polycrystalline melt stiffness, based on averages of anisotropic moduli over a distribution of grain orientations. Since a uniform distribution of grain orientations is assumed, there are no symmetry assumptions for the resulting

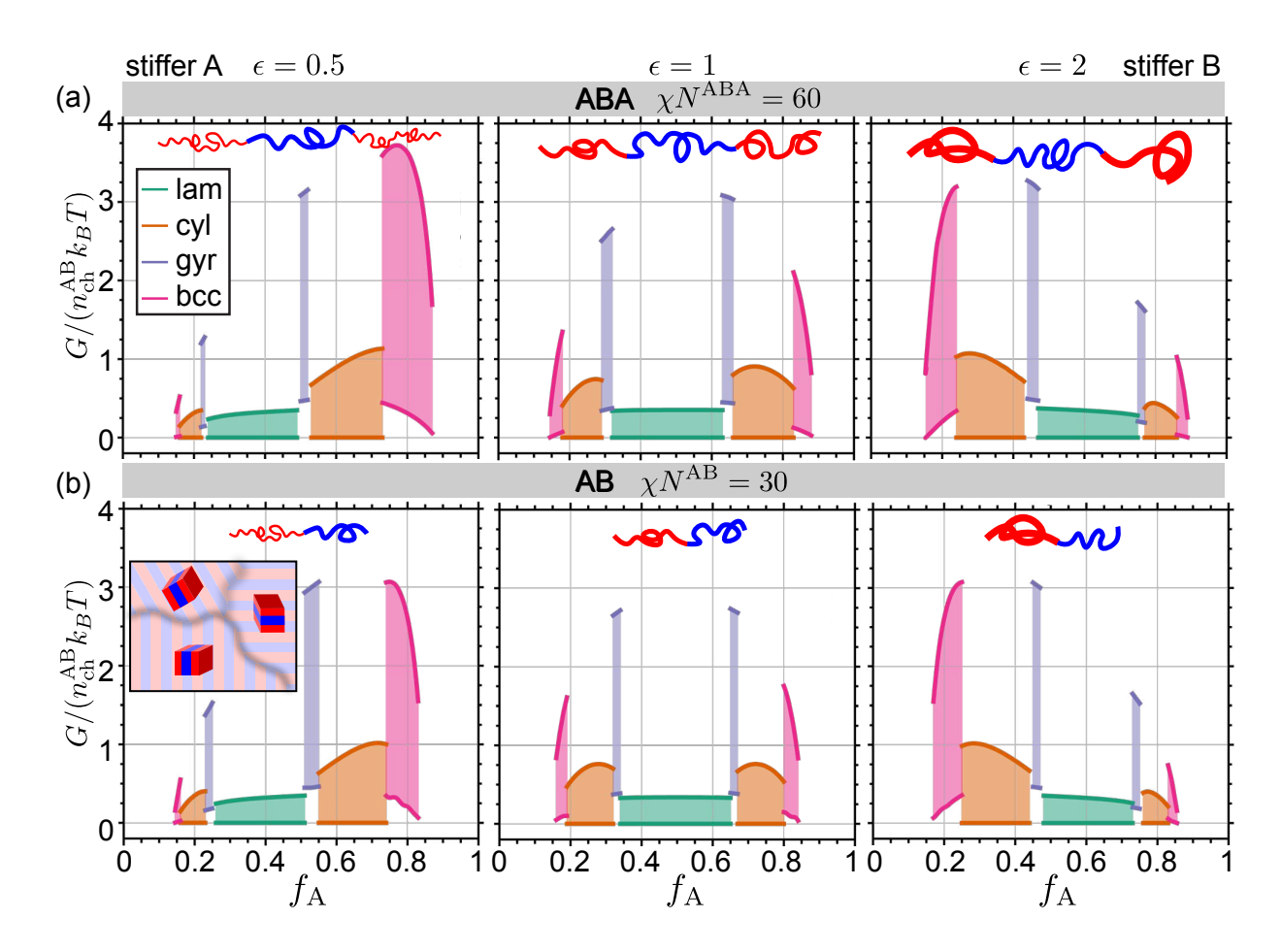


Figure 6: Comparison of polycrystalline average modulus bounds (upper bound  $G_V$ , lower bound  $G_R$ ) for all phases for (a) ABA and (b) AB melts at  $\chi N^{AB}$ =30.

polycrystal, so it is expected to behave like a 3D isotropic elastic medium, and is therefore characterized in terms of two elastic moduli. As one of these moduli can be taken to be the bulk modulus, which is undefined for our volume-constrained calculations, it is sufficient to determine the macroscopic shear modulus G. Treating the lamellar and cylindrical phases as lower-dimensional slices of 3D materials with an orthorhombic unit cell, we calculated the Voigt  $G_V$  and Reuss  $G_R$  averages of the macroscopic shear modulus <sup>74</sup> (see SI Section S5 for details) and plotted the results in their stable regions for fixed  $\chi N$  in Figure 6 (for a full heat map across  $\chi N$ , see SI Figure S21).

Comparing the upper polycrystalline average to perfectly-ordered structures, we note that the lamellar moduli were drastically reduced and relatively flattened, whereas columnar moduli were relatively consistent and cubic were increased. Notably, the Reuss bound is zero for lamellae and columnar phases, as they have liquid-like directions that dominate the response under isostress conditions. This suggests that while all structured phases display nonterminal behavior, 1D and 2D ultimately fail to be rigid due to an almost-certain presence of a grain orientation that allows for liquid-like flow. However, Reuss bounds for cubic phases are nonzero, suggesting a plateau behavior at terminal times (i.e., zero-frequency response,  $\omega \to 0$ ).

Experimental testing on ceramic composites demonstrates that gyroid is inherently mechanically superior to BCC,  $^{75}$  and it is notable our results do agree with this despite the long timescales assumed for our computations (with the exception of a range of high- $f_A$  structures when  $\epsilon = 0.5$ ). However, in the case of BCPs, this may also be partly due to greater volume fraction asymmetry for BCC compared to gyroid: approaching the disordered ("miscible") phase lowers the stiffness of the material, apart from the inherent mechanical properties of the morphology itself, since the terminal rigidity relies on the existence of microphase separated domains. Indeed, the composite stiffness, while dependent on morphology, adopts an overall trend that conforms to the expected BCP miscibility gap. We note that in all cases, cubic is stiffer than 2D is stiffer than 1D structures, in agreement with Kossuth, et al.  $^8$  (viz., Figure  $^1$ (a)).

As hinted in Figure 6, the Voigt (upper) bounds for the 3D phases form a rather smooth "envelope" that is concave down, centered around  $f_A = 0.55$  for  $\epsilon = 1$ , and shifted to higher and lower  $f_A$  for  $\epsilon = 0.5, 2$  respectively. This result is born out in heat maps of Voigt (upper) modulus bounds for each  $\epsilon$  shown in SI Figure S21: level sets seemingly match across phase boundaries, albeit with drastically different absolute values of modulus. Taking the convex hull of gyroid and BCC Voigt bounds gives a smooth curve as shown in SI Figure S22, indicating a characteristic upper bound modulus for 3D BCP phases that is not expected to be particularly sensitive to the underlying morphology, although we have not confirmed that the envelope accurately predicts the stiffness of competing 3D phases. Nevertheless, we

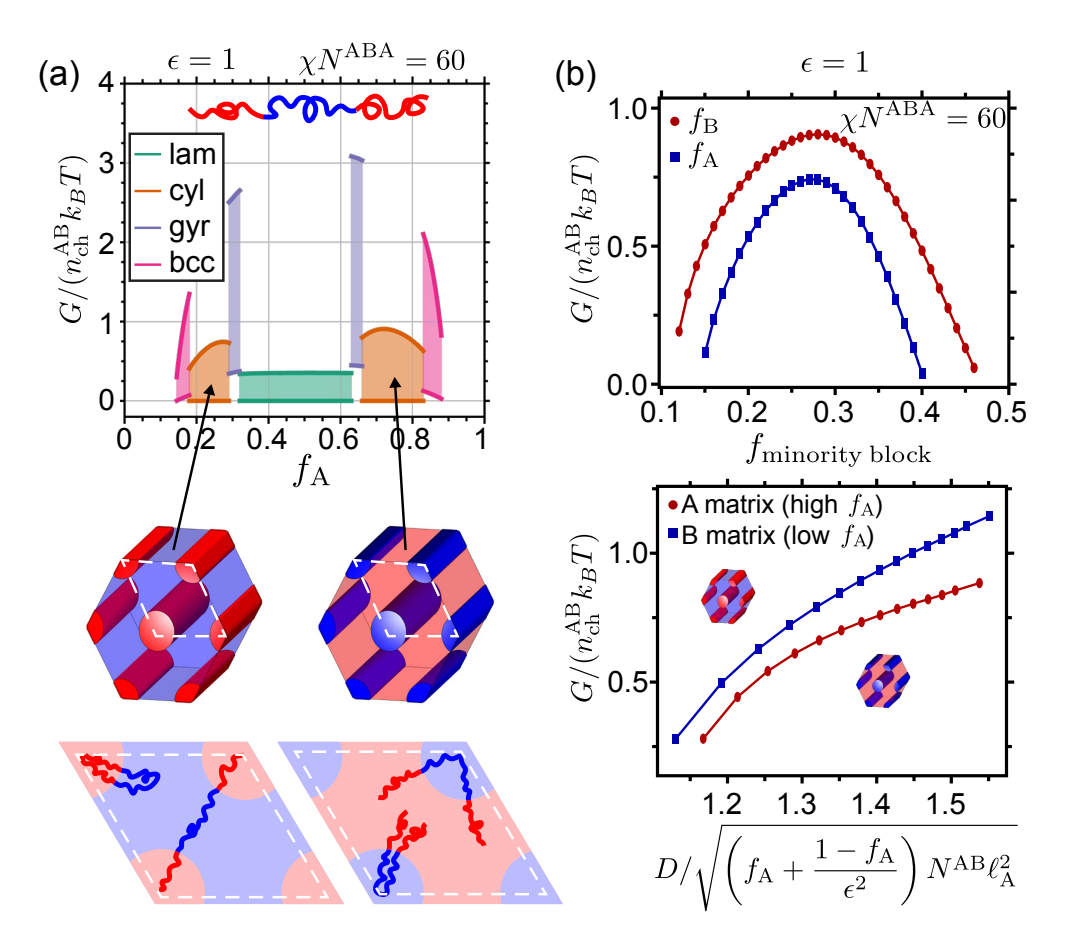


Figure 7: Modulus asymmetry for ABA triblocks, as illustrated in the case of columnar phase for  $\chi N^{\rm ABA} = 60$ ,  $\epsilon = 1$ . (a) Modulus plot for all phases, illustrating the difference between B matrix (left) with bridging and looping chains vs A matrix (right) without bridging chains. (b, top) Modulus for columnar phase plotted against  $f_{\rm minority \, block}$  with minority A as blue squares and minority B as red circles. (b, bottom) Modulus plotted against domain spacing, D, normalized by  $f_{\rm A}$  and  $\epsilon$ , separated into A matrix ( $f_{\rm A} = 0.7$ , red circles) and B matrix ( $f_{\rm A} = 0.3$ , blue squares).

propose that this convex hull would include any long-lived response of metastable 3D phases, such as the double diamond network phase or more exotic sphere phases.

As discussed in the case of both columnar and cubic rigidity, for ABA melts, larger  $f_A$  structures are stiffer for  $\epsilon = 1$  and equivalent  $f_A$  for  $\epsilon = 0.5, 2$ . In particular if we study the case of  $\epsilon = 1$ , it is counterintuitive that A matrix melts are stiffer than B matrix since there are no bridging chains in that case. Indeed, bridging chains are commonly used to stiffen and toughen thermoplastics,  $^{76,77}$  and yet the stiffer melt is achieved in the inverted phases, in which there are no bridging chains, as illustrated in Figure 7(a). In order to

further probe this unintuitive result, we compared the modulus for each conformation with respect to domain spacing D (tuned via segregation strength  $\chi N$ ), not just  $f_A$ , shown in Figure 7(b). This comparison revealed that bridging conformations have greater modulus with respect to D than non-bridging conformations, further demonstrating the importance of D when comparing moduli of "equivalent" systems. Thus, complementary methods of designing melts—direct control over minority domain block fraction or indirect control over D (e.g. via segregation strength  $\chi N$ )—alters the projected response of the melt.

To confirm that the modulus calculations involve bridging chains, we use the method described by Matsen and Thompson<sup>4</sup> (see SI Section S6 for more details) to compute chain bridging fractions, finding that the "normal" low- $f_A$  cylinder phase consistently has bridging fractions in the range of 60 - 75%, as shown in SI Figure S23(b). As we discuss below, since the terminal rigidity quantifies the ability for melts to undergo long-time relaxation under fixed strain, we can attribute this unexpected softening effect of bridging chains to an additional structural relaxation that they enable.

## Organization of chains around slip surfaces

Building on our earlier result that bridging conformations exhibit a higher effective modulus than non-bridging ones when fixing domain size, we next consider where that added stiffness resides in the lamellar profile and how modest deformation (10% strain) is accommodated. For BCP melts, the presence of bridging chains ensures that neighboring microphase separated domains form a connected network of material. These bridging chains form connections across terminal boundaries  $^{52}$ —slip surfaces that exist between domains, where the ends of one brush meets the ends of an opposite-facing brush (or chain midpoints for ABA), such as the configuration shown in Figure 8(a). Without bridging chains, the primary interaction across slip surfaces comes through the form of steric repulsion.  $^{78,79}$  For AB copolymers, the B-block slip surface is truly a "terminal" boundary, consisting of a distribution of free chain ends  $g_{\text{end}}(x/D)$  coming from either brush. Meanwhile, the B-block slip surface for ABA

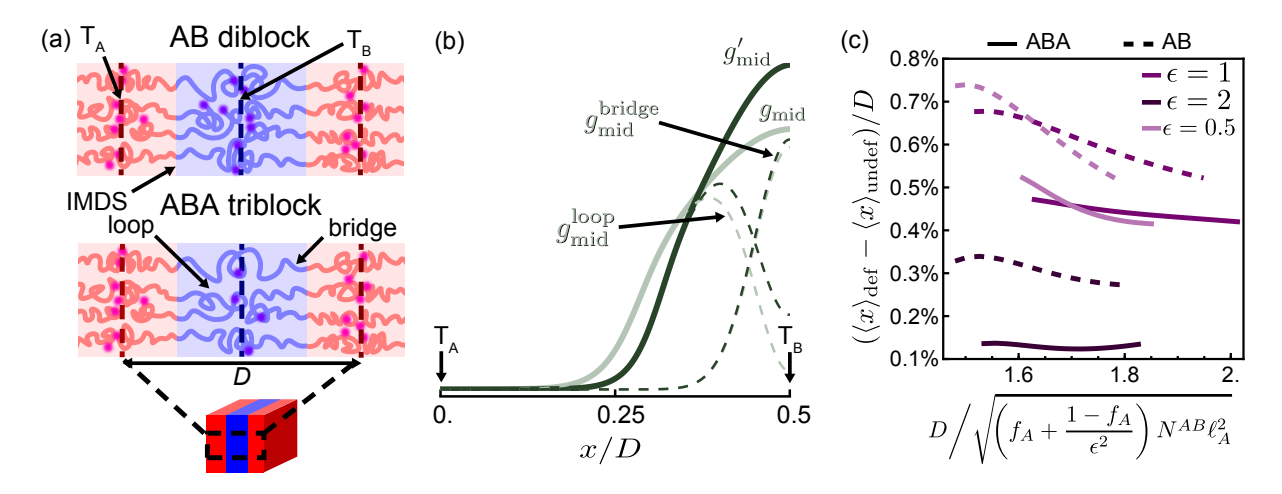


Figure 8: (a) Depiction of polymer chains in lamellar phase for AB and ABA, with looping and bridging conformations shown for ABA and with chain ends (AB) and chain midpoints (ABA) highlighted, along with the terminal boundaries. (b) Cartoon schematic for the chain midpoint distribution of ABA, comparing the undeformed with the deformed configurations (see SI for actual data). Solid curves show total chain distribution  $g_{\text{mid}}$ ; the matching dashed curves denote bridging  $g_{\text{mid}}^{\text{bridge}}$  and looping  $g_{\text{mid}}^{\text{loop}}$  contributions to this distribution. (c) Comparison of change in chain stretch between the deformed (10% strain) and undeformed states as a function of scaled domain spacing for AB (dashed) and ABA (solid) systems.

copolymers is demarcated by the distribution of chain midpoints  $g_{\text{mid}}(x/D)$ , consisting of looping chain and bridging chain midpoints.

In order to assess the response of chains to uniaxial deformations of lamellae, consider that chains must stretch in order to maintain the incompressibility of the melt, filling in any void potentially opened up in the terminal boundary between brush layers. Much of our intuition is derived from the Alexander-de Gennes  $^{80-82}$  picture of polymer brushes, in which chain ends uniformly extend from the grafting surface to the maximum extent of the brush. However, a more complete physical picture based in parabolic brush theory  $^{83,84}$  shows that chains have a non-uniform distribution of stretching costs. Since the stretching cost scales with end-to-end separation distance, we can view the chain end or midpoint distribution as a proxy for chain stretching. For lamellae assembled by a monodisperse collection of linear chains, distributions are unimodal, with maxima at the B-block terminal boundary  $T_B$ . The average chain stretch  $\langle x \rangle/D$  is given by the end-to-end (or end-to-midpoint) separation

averaged over the distribution g(x/D), viz.,

$$\frac{\langle x \rangle}{D} = \frac{\int_0^{1/2} du \, u \, g(u)}{\int_0^{1/2} du \, g(u)}, \tag{8}$$

where we have defined  $u \equiv x/D$ . If the distribution is narrow, then chain ends are focused about the terminal boundary; the Alexander-de Gennes case has a  $\delta$  distribution,  $g(x/D) = \delta(x/D-1/2)$ . The average stretching cost of chains is reduced for broader distributions since  $\langle x \rangle/D$  is pushed to lower values  $\langle x \rangle/D \leq 1/2$ , with the upper bound of 1/2 representing the Alexander-de Gennes limit.

Under a uniaxial deformation of the lamellae, the average stretch is expected to increase, as chains ends are drawn towards the terminal boundary in order to maintain the melt's incompressibility. This increased stretch is also required to maintain mechanical equilibrium: since an imposed deformation of the melt puts it in a state of stress, this stress is balanced by an increase in chain tension. Consequently, the difference in stretch between the undeformed and deformed states,  $(\langle x \rangle_{\text{def}} - \langle x \rangle_{\text{undef}})/D$ , is positive for extensile deformations, reflecting the narrowing of g(x/D), as illustrated in Figure 8(b). As shown in Figure 8(c), AB melts undergo larger changes in average stretch that ABA melts. This is consistent with our observations that, at fixed D-spacing, AB melts are somewhat stiffer than ABA melts. To explain this, note that the chain midpoint distributions for ABA copolymers have a slightly different shape than AB chain end distributions; see SI Figure S24 for comparisons. The ABA distribution can be decomposed into the sum of two parts: a midpoint distribution for looping chains  $g_{\text{mid}}^{\text{loop}}$  and one for bridging chains  $g_{\text{mid}}^{\text{bridge}}$ . As depicted in Figure 8(b), the bridging chains are expected to have midpoints that form a narrow distribution about the terminal surface, depleting the distribution of looping chain midpoints from the terminal boundary. We find that lamellae maintain a bridging fraction  $\nu_b \approx 48 - 52\%$  both before and after deformation over a range of compositions and conditions, consistent with theoretical predictions of strongsegregation theory (see SI Figure S23(a)). 85-88 In fact, for any single melt, we find that the change in bridging chains  $\Delta\nu_b$  is small, typically  $\Delta\nu_b \lesssim 0.5\%$  for 10% strain. This shows that the contribution of looping chains to the midpoint distribution is both significant and relatively static under deformation. Consequently, any changes to the midpoint distribution are dominated by the looping configurations. Since the midpoints of these looping chains are significantly depleted from the terminal boundary, their re-distribution is constrained relative to the ability of AB chains to be drawn to the terminal boundary. Therefore, the ability of ABA lamellae to increase average chain stretching is comparatively reduced under equivalent conditions to AB lamellae. We emphasize, however, that undeformed ABA melts have a larger average chain stretch than undeformed AB melts owing to the population of bridging chains.

Notably, we find that the change in bridging fraction for a columnar system is much larger, often on the order of a few percent for 10% uniaxial strain. It has recently been shown shown that there is significant exchange of chains between domains over timescales that exceed the typical macroscopic stress relaxation time. Exchanges of bridging chains can take the form of exchange of bridge ends between different domains as well as bridge-loop interconversion. Our observation of reduced bridging conformations under deformation indicates a net flux of the population of bridging chains converting to looping chains.

# Conclusions and Outlook

We have demonstrated that self-consistent field theory (SCFT) can be used to probe the terminal mechanics of ABA and AB BCP melts, rapidly iterating over multiple configurations and segregation strengths. Specifically, SCFT can reproduce certain expected results for BCP stiffness, in particular for long time scales: (i) lamellae and columnar phases behave as liquid crystals, with a vanishing lower bound elastic modulus  $G_R$ ; (ii) the upper bound elastic modulus  $G_V$  increases in the order of pattern dimensionality, from 1D lamellae to 2D cylinders to 3D cubic phases. We find that terminal stiffness comparisons between ABA and

AB melts as well as normal (bridging) vs inverse (non-bridging) phases are complicated by preferred representation of information. The materials structure representation of stiffness as a function of D-spacing—often used for the design of thermoplastics  $^{70,90}$ —shows that AB melts are stiffer than ABA melts and inverse phases of ABA melts are less stiff than the normal phases; the synthetic chemistry representation as a function of  $f_A$  reports opposite results. In particular, the observed reduction in stiffness due to bridging chains at fixed  $f_A$  is counter-intuitive, as bridging chains constrain relaxation of slip surfaces (i.e., terminal boundaries). We propose that while bridging chains indeed increase the stiffness of the melt for short-to-intermediate times, their softening effect over longer timescales comes from (i) reduction in the average stretch of chains under deformation due to depletion of the looping chains at the terminal boundary; (ii) long-time relaxation of the melt due to interconversion between bridging and looping chains and re-distribution of bridging chains.

The equilibrium assumption of SCFT calculations requires that polymers have had sufficient time to sample a large number of microstates. Thus, there is no real distinction between rubbery and glassy polymers. However, the dynamical rigidity plays an important role in the design of widely-used BCPs such as PDMS-PEO (rubbery-rubbery), SBS (glassy-rubbery), and PS-PMMA (glassy-glassy). To experimentally corroborate our results, ideally rubbery BCPs (amorphous polymers with glass transition temperatures below room temperature — i.e., PB, PEO, PDMS, amorphous PE) may be synthesized with targeted microphase based on  $\chi N$ ,  $f_A$  and Kuhn length ratio  $\epsilon$  and characterized via TEM or SAXS, with deformations studied under shear rheology at various temperatures and shear rates. Time-temperature superposition can provide  $\chi$  (if unknown) for higher frequencies and also provide low-frequency modulus, which can be compared with the results discussed herein and possibly build out the full frequency-modulus plot as illustrated in Figure 1. A detailed description of helpful methodologies to characterize the effect of polymer microstructure on deformation response is outlined by Honeker and Thomas <sup>76</sup> and would be useful to further advance this research. A more detailed understanding of BCP terminal mechanics with respect to microstructure

and associated design parameters (segregation strength, volume fraction and Kuhn length of respective blocks) is advantageous for polymer systems for use in extended lifetime or high temperature applications, such as structural engineering designs (buildings, bridges) or automotive industry (break and engine parts). This study paves the way to understanding failure mechanics in BCP melts, addressing creep in shear and extension modes. Using the inherent microphase separation of BCP melts to achieve arrested creep and enhanced toughness has several advantages over chemically-crosslinked thermoset materials, including no need for potentially toxic additives (e.g., crosslinkers and initiators) and enhanced degradability profile.

Finally, this work can be regarded as a study of mass transport and how equilibrium mass exchange between domains and along interfaces—known to be highly morphology-dependent  $^{91}$ —determines the quasistatic response of polymer melts. The liquid-like response of lamellar and columnar morphologies, along with long-time activated exchange of bridging chains between domains, helps expose a picture of equilibration of BCP melts across scales that has been recently developed by theoretical  $^{62,92}$  and experimental  $^{18,89,93}$  efforts. We leave a more in-depth exploration of how domain structure, topology, and deformation affect chain exchange and loop  $\Leftrightarrow$  bridge interconversion for future study.

# Acknowledgement

The authors would like to thank E. L. Thomas, F. Bates, B. R. Greenvall, and R. Mathew for useful discussions.

# Supporting Information Available

Supplementary text can be found at [[to be added]]. Data and code can be found at [[to be added]].

## References

- (1) Doi, M.; Edwards, S. F. *The theory of polymer dynamics*; International series of monographs on physics; Oxford Univ. Press: Oxford, 1986.
- (2) Jeong, D.; Cui, S.; Jahan, N.; Ellison, C. J.; Bates, F. S. Compatibilization of iPP/PS Blends with Diblock and Triblock Copolymers. *Macromolecules* **2025**, *58*, 10026–10036.
- (3) Ruzette, A.-V.; Leibler, L. Block copolymers in tomorrow's plastics. *Nature Materials* **2005**, *4*, 19–31.
- (4) Matsen, M. W.; Thompson, R. B. Equilibrium behavior of symmetric ABA triblock copolymer melts. *The Journal of Chemical Physics* **1999**, *111*, 7139–7146.
- (5) Matsen, M. W. The standard Gaussian model for block copolymer melts. *Journal of Physics: Condensed Matter* **2001**, *14*, R21.
- (6) Matsen, M. W.; Bates, F. S. Origins of complex self-assembly in block copolymers.

  \*Macromolecules 1996, 29, 7641–7644.
- (7) Dimitriyev, M. S.; Reddy, A.; Grason, G. M. Medial packing, frustration, and competing network phases in strongly segregated block copolymers. *Macromolecules* 2023, 56, 7184–7202.
- (8) Kossuth, M. B.; Morse, D. C.; Bates, F. S. Viscoelastic behavior of cubic phases in block copolymer melts. *Journal of Rheology* **1999**, *43*, 167–196.
- (9) Chaikin, P. M.; Lubensky, T. C. *Principles of Condensed Matter Physics*; Cambridge University Press, 1995; p 288–352.
- (10) Read, D. J.; Duckett, R. A.; Sweeney, J.; McLeish, T. C. B. The chevron folding instability in thermoplastic elastomers and other layered materials. *Journal of Physics* D: Applied Physics 1999, 32, 2087.

- (11) Knoll, A.; Horvat, A.; Lyakhova, K. S.; Krausch, G.; Sevink, G. J. A.; Zvelindovsky, A. V.; Magerle, R. Phase behavior in thin films of cylinder-forming block copolymers. *Phys. Rev. Lett.* 2002, 89, 035501.
- (12) Jinnai, H.; Sawa, K.; Nishi, T. Direct observation of twisted grain boundary in a block copolymer lamellar nanostructure. *Macromolecules* **2006**, *39*, 5815–5819.
- (13) Mareau, V. H.; Akasaka, S.; Osaka, T.; Hasegawa, H. Direct visualization of the perforated layer/gyroid grain boundary in a polystyrene-block-polyisoprene/polystyrene blend by electron tomography. *Macromolecules* **2007**, *40*, 9032–9039.
- (14) Kim, J.; Green, P. F. Directed assembly of nanoparticles in block copolymer thin films: Role of defects. *Macromolecules* **2010**, *43*, 10452–10456.
- (15) Pezzutti, A. D.; Vega, D. A.; Villar, M. A. Dynamics of dislocations in a two-dimensional block copolymer system with hexagonal symmetry. *Philosophical Transactions of the Royal Society A: Mathematical, Physical and Engineering Sciences* **2011**, *369*, 335–350.
- (16) Ryu, H. J.; Fortner, D. B.; Lee, S.; Ferebee, R.; De Graef, M.; Misichronis, K.; Avgeropoulos, A.; Bockstaller, M. R. Role of grain boundary defects during grain coarsening of lamellar block copolymers. *Macromolecules* **2013**, *46*, 204–215.
- (17) Li, W.; Müller, M. Defects in the Self-Assembly of Block Copolymers and Their Relevance for Directed Self-Assembly. *Annual Review of Chemical and Biomolecular Engineering* **2015**, *6*, 187–216.
- (18) Feng, X.; Zhuo, M.; Guo, H.; Thomas, E. L. Visualizing the double-gyroid twin. *Proceedings of the National Academy of Sciences* **2021**, *118*, e2018977118.
- (19) Feng, X.; Dimitriyev, M. S.; Thomas, E. L. Soft, malleable double diamond twin.

  Proceedings of the National Academy of Sciences 2023, 120, e2213441120.

- (20) Dimitriyev, M. S.; Greenvall, B. R.; Mathew, R.; Grason, G. M. Not Even Metastable: Cubic Double-Diamond in Diblock Copolymer Melts. ACS Macro Letters 2025, 14, 1291–1298.
- (21) Holden, G. In *Rubber Technology*; Morton, M., Ed.; Springer Dordrecht, 1999; pp 465–481.
- (22) Rubinstein, M.; Colby, R. H. *Polymer Physics*, 1st ed.; Oxford University Press, 2003; pp 49–96.
- (23) Milner, S. T. Chain Architecture and Asymmetry in Copolymer Microphases. *Macro-molecules* **1994**, *27*, 2333–2335.
- (24) Wei, P.; Bhat, G. A.; Cipriani, C. E.; Mohammad, H.; Schoonover, K.; Pentzer, E. B.; Darensbourg, D. J. 3D Printed CO2-based triblock copolymers and post-printing modification. *Angewandte Chemie International Edition* **2022**, *61*, e202208355.
- (25) Schoonover, K. G.; Hsieh, C.-M.; Sengoden, M.; Ahmed, N.; Kalairaj, M. S.; Ware, T. H.; Darensbourg, D. J.; Pentzer, E. B.; Wei, P. Bridging polymer architecture, printability, and properties by digital light processing of block copolycarbonates. Chemical Science 2024, 15, 14228–14240.
- (26) Graessley, W. W. Statistical mechanics of random coil networks. *Macromolecules* 1975, 8, 186–190.
- (27) Deng, J.; Tabei, J.; Shiotsuki, M.; Sanda, F.; Masuda, T. Conformational transition between random coil and helix of poly(N-propargylamides). *Macromolecules* **2004**, *37*, 1891–1896.
- (28) Tracy, M.; Pecora, R. Dynamics of rigid and semirigid rodlike polymers. *Annual Review of Physical Chemistry* **1992**, *43*, 525–557.

- (29) Hu, X.-D.; Jenkins, S. E.; Min, B. G.; Polk, M. B.; Kumar, S. Rigid-Rod polymers: synthesis, processing, simulation, structure, and properties. *Macromolecular Materials and Engineering* **2003**, *288*, 823–843.
- (30) Wang, D. H.; Jiang, H.; Wade Adams, W. Encyclopedia of Polymer Science and Technology; John Wiley & Sons, Ltd, 2011.
- (31) Bates, F. S.; Hillmyer, M. A.; Lodge, T. P.; Bates, C. M.; Delaney, K. T.; Fredrickson, G. H. Multiblock polymers: Panacea or Pandora's Box? *Science* **2012**, *336*, 434–440.
- (32) Bates, C. M.; Maher, M. J.; Janes, D. W.; Ellison, C. J.; Willson, C. G. Block copolymer lithography. *Macromolecules* **2014**, *47*, 2–12.
- (33) Sinturel, C.; Bates, F. S.; Hillmyer, M. A. High  $\chi$ -low N block polymers: How far can we go? ACS Macro Letters **2015**, 4, 1044–1050.
- (34) Durand, W. J.; Blachut, G.; Maher, M. J.; Sirard, S.; Tein, S.; Carlson, M. C.; Asano, Y.; Zhou, S. X.; Lane, A. P.; Bates, C. M.; Ellison, C. J.; Willson, C. G. Design of high-χ block copolymers for lithography. *Journal of Polymer Science Part A: Polymer Chemistry* 2015, 53, 344–352.
- (35) Pino, G.; Cummins, C.; Mantione, D.; Demazy, N.; Alvarez-Fernandez, A.; Guldin, S.; Fleury, G.; Hadziioannou, G.; Cloutet, E.; Brochon, C. Design and morphological investigation of high-χ catechol-containing styrenic block copolymers. *Macromolecules* 2022, 55, 6341–6350.
- (36) Yang, Z.; Zhang, T.; Zhan, D.; Qian, X.; Deng, H. High-χ poly(fluorinated methacrylate)-block-poly(acetoxystyrene) block copolymers for sub-5 nm nanopatterning. ACS Applied Materials & Interfaces 2025, 17, 39514–39525.

- (37) Sunday, D. F.; Chang, A. B.; Liman, C. D.; Gann, E.; Delongchamp, D. M.; Thomsen, L.; Matsen, M. W.; Grubbs, R. H.; Soles, C. L. Self-Assembly of ABC bottlebrush triblock terpolymers with evidence for looped backbone conformations. *Macromolecules* **2018**, *51*, 7178–7185.
- (38) Parkatzidis, K.; Wang, H. S.; Truong, N. P.; Anastasaki, A. Recent developments and future challenges in controlled radical polymerization: A 2020 update. *Chem* **2020**, *6*, 1575–1588.
- (39) Zhou, Y.-N.; Li, J.-J.; Wang, T.-T.; Wu, Y.-Y.; Luo, Z.-H. Precision polymer synthesis by controlled radical polymerization: Fusing the progress from polymer chemistry and reaction engineering. *Progress in Polymer Science* **2022**, *130*, 101555.
- (40) Destarac, M. Controlled radical polymerization: Industrial stakes, obstacles and achievements. *Macromolecular Reaction Engineering* **2010**, *4*, 165–179.
- (41) Braunecker, W. A.; Matyjaszewski, K. Controlled/living radical polymerization: Features, developments, and perspectives. *Progress in Polymer Science* **2007**, *32*, 93–146, 50 years of living polymerization.
- (42) Hoogenboom, R. In *Handbook of ring-opening polymerization*; Dubois, P., Coulembier, O., Raquez, J.-M., Eds.; Wiley-VCH, 2009; Chapter Polyethers and polyoxazolines.
- (43) Coulembier, O.; Dubois, P. In Handbook of ring-opening polymerization; Dubois, P., Coulembier, O., Raquez, J.-M., Eds.; Wiley-VCH, 2009; Chapter Polyesters from βlactones.
- (44) Bielawski, C. W.; Grubbs, R. H. Living ring-opening metathesis polymerization.

  Progress in Polymer Science 2007, 32, 1–29, 50 years of living polymerization.

- (45) Schrock, R. R. Synthesis of stereoregular polymers through ring-opening metathesis polymerization. *Accounts of Chemical Research* **2014**, *47*, 2457–2466.
- (46) Mandal, H.; Ogunyemi, O. J.; Nicholson, J. L.; Orr, M. E.; Lalisse, R. F.; Rentería-Gómez, A.; Gogoi, A. R.; Gutierrez, O.; Michaudel, Q.; Goodson, T. I. Linear and non-linear optical properties of all-cis and all-trans poly(p-phenylenevinylene). The Journal of Physical Chemistry C 2024, 128, 2518–2528.
- (47) Yang, J. S.-J.; Fang, L. Conjugated ladder polymers: Advances from syntheses to applications. *Chem* **2024**, *10*, 1668–1724.
- (48) Dietz, J. D.; Nan, K.; Hoy, R. S. Unexpected ductility in semiflexible polymer glasses with entanglement length equal to their kuhn length. *Phys. Rev. Lett.* **2022**, *129*, 127801.
- (49) Voigt, W. Ueber die Beziehung zwischen den beiden Elasticitätsconstanten isotroper Körper. Annalen der Physik 1889, 274, 573–587.
- (50) Reuss, A. Calculation of the flow limits of mixed crystals on the basis of the plasticity of monocrystals. Z. Angew. Math. Mech 1929, 9, 49–58.
- (51) Hill, R. The Elastic Behaviour of a Crystalline Aggregate. *Proceedings of the Physical Society. Section A* **1952**, *65*, 349.
- (52) Reddy, A.; Feng, X.; Thomas, E. L.; Grason, G. M. Block copolymers beneath the surface: measuring and modeling complex morphology at the subdomain scale. *Macro-molecules* **2021**, *54*, 9223–9257.
- (53) O'Connor, T. C.; Hopkins, A.; Robbins, M. O. Stress Relaxation in Highly Oriented Melts of Entangled Polymers. *Macromolecules* **2019**, *52*, 8540–8550.
- (54) Helfand, E. Theory of inhomogeneous polymers: Fundamentals of the Gaussian random-walk model. *The Journal of Chemical Physics* **1975**, *62*, 999–1005.

- (55) Arora, A.; Qin, J.; Morse, D. C.; Delaney, K. T.; Fredrickson, G. H.; Bates, F. S.; Dorfman, K. D. Broadly accessible self-consistent field theory for block polymer materials discovery. *Macromolecules* 2016, 49, 4675–4690.
- (56) Thompson, R. B.; Rasmussen, K. O.; Lookman, T. Elastic moduli of multiblock copolymers in the lamellar phase. *The Journal of Chemical Physics* **2004**, *120*, 3990–3996.
- (57) Zhang, L.; Lin, J.; Lin, S. Elastic properties of graft copolymers in the lamellar phase studied by self-consistent field theory. *Soft Matter* **2009**, *5*, 173–181.
- (58) Zhu, X.; Wang, L.; Lin, J. Distinct elastic response to hierarchical nanostructures.

  \*Macromolecules\*\* 2011, 44, 8314–8323.
- (59) Chu, X.; Xu, Z.; Cao, Y.-c.; Li, W. Simulation study on the mechanical properties of lamella-forming ABABA linear multiblock copolymers. *Macromolecules* **2024**, *57*, 9536–9545.
- (60) Chen, G.; Zhang, H.; Lu, T.; Jiang, Y. The stress deformation response influenced by the chain rigidity for mesostructures in diblock copolymers. *Phys. Chem. Chem. Phys.* **2021**, *23*, 22992–23004.
- (61) Tyler, C. A.; Morse, D. C. Linear elasticity of cubic phases in block copolymer melts by self-consistent field theory. *Macromolecules* **2003**, *36*, 3764–3774.
- (62) Dimitriyev, M. S.; Feng, X.; Thomas, E. L.; Grason, G. M. Nonaffinity of liquid networks and bicontinuous mesophases. *Phys. Rev. Lett.* **2024**, *132*, 218201.
- (63) Ajdari, A.; Leibler, L. Bending moduli and stability of copolymer bilayers. *Macro-molecules* **1991**, *24*, 6803–6805.
- (64) Cohen, Y.; Albalak, R. J.; Dair, B. J.; Capel, M. S.; Thomas, E. L. Deformation of Oriented Lamellar Block Copolymer Films. *Macromolecules* **2000**, *33*, 6502–6516.

- (65) Man, X.; Tang, J.; Zhou, P.; Yan, D.; Andelman, D. Lamellar Diblock Copolymers on Rough Substrates: Self-Consistent Field Theory Studies. *Macromolecules* 2015, 48, 7689–7697.
- (66) Gennes, P. G. D.; Prost, J. *The Physics of Liquid Crystals*; Oxford University Press, 1993.
- (67) Semenov, A. Contribution to the theory of microphase layering in block-copolymer melts. Sov Phys JETP 1985, 61, 733.
- (68) Landau, L. D.; Lifshitz, E. M.; Kosevich, A. M.; Pitaevskii, L. P. *Theory of elasticity*; Course of theoretical physics; Butterworth-Heinemann, 1986.
- (69) Helfand, E.; Sapse, A. M. Theory of unsymmetric polymer–polymer interfaces. *The Journal of Chemical Physics* **1975**, *62*, 1327–1331.
- (70) Kossuth, M. B.; Morse, D. C.; Bates, F. S. Viscoelastic behavior of cubic phases in block copolymer melts. *Journal of Rheology* **1999**, *43*, 167–196.
- (71) Nagpal, U.; Müller, M.; Nealey, P. F.; de Pablo, J. J. Free Energy of Defects in Ordered Assemblies of Block Copolymer Domains. *ACS Macro Letters* **2012**, *1*, 418–422.
- (72) Li, W.; Müller, M. Thermodynamics and Kinetics of Defect Motion and Annihilation in the Self-Assembly of Lamellar Diblock Copolymers. *Macromolecules* 2016, 49, 6126–6138.
- (73) Blagojevic, N.; Müller, M. Multiscale Modeling of Grain-Boundary Motion in Cylinder-Forming Block Copolymers. *ACS Polymers Au* **2023**, *3*, 96–117.
- (74) Berryman, J. G. Bounds and self-consistent estimates for elastic constants of polycrystals composed of orthorhombics or crystals with higher symmetries. *Physical Review E* **2011**, 83.

- (75) Sokollu, B.; Gulcan, O.; Konukseven, E. I. Mechanical properties comparison of strutbased and triply periodic minimal surface lattice structures produced by electron beam melting. *Additive Manufacturing* **2022**, *60*, 103199.
- (76) Honeker, C. C.; Thomas, E. L. Impact of morphological orientation in determining mechanical properties in triblock copolymer systems. Chemistry of Materials 1996, 8, 1702–1714.
- (77) Eagan, J. M.; Xu, J.; Girolamo, R. D.; Thurber, C. M.; Macosko, C. W.; La-Pointe, A. M.; Bates, F. S.; Coates, G. W. Combining polyethylene and polypropylene: Enhanced performance with PE/iPP multiblock polymers. Science 2017, 355, 814–816.
- (78) Zhulina, E. B.; Borisov, O. V.; Priamitsyn, V. A. Theory of steric stabilization of colloid dispersions by grafted polymers. *Journal of Colloid and Interface Science* 1990, 137, 495–511.
- (79) Milner, S. T. Polymer Brushes. *Science* **1991**, *251*, 905–914.
- (80) De Gennes, P.-G. Scaling theory of polymer adsorption. *Journal de Physique* **1976**, *37*, 1445–1452.
- (81) Alexander, S. Adsorption of chain molecules with a polar head a scaling description.

  Journal de Physique 1977, 38, 983–987.
- (82) de Gennes, P.-G. Conformations of Polymers Attached to an Interface. *Macromolecules* **1980**, *13*, 1069–1075.
- (83) Semenov, A. N. Contribution to the theory of microphase layering in block-copolymer melts. *Journal of Experimental and Theoretical Physics* **1985**, *88*, 1242.
- (84) Milner, S. T.; Witten, T. A.; Cates, M. E. Theory of the grafted polymer brush. *Macro-molecules* **1988**, *21*, 2610–2619.

- (85) Milner, S. T.; Witten, T. A. Bridging attraction by telechelic polymers. *Macromolecules* 1992, 25, 5495–5503.
- (86) Semenov, A. N.; Joanny, J.-F.; Khokhlov, A. R. Associating polymers: Equilibrium and linear viscoelasticity. *Macromolecules* **1995**, *28*, 1066–1075.
- (87) Björling, M. Using End-Confined Chains To Model End-Absorbing, Triblock Copolymers: 1. Analytical Approach. *Macromolecules* **1998**, *31*, 9026–9032.
- (88) Björling, M.; Stilbs, P. Using End-Confined Chains To Model End-Absorbing, Triblock Copolymers: 2. Numerical Approach. *Macromolecules* **1998**, *31*, 9033–9043.
- (89) White, J. M.; Kim, T.; Bates, F. S.; Lodge, T. P. How does the rate of chain exchange relate to stress relaxation in triblock copolymer networks? *ACS Central Science* **2025**, 11, 422–430.
- (90) Mamodia, M.; Panday, A.; Gido, S. P.; Lesser, A. J. Effect of Microdomain Structure and Process Conditions on the Mechanical Behavior of Cylindrical Block Copolymer Systems. *Macromolecules* 2007, 40, 7320–7328.
- (91) Shen, K.-H.; Brown, J. R.; Hall, L. M. Diffusion in Lamellae, Cylinders, and Double Gyroid Block Copolymer Nanostructures. *ACS Macro Letters* **2018**, *7*, 1092–1098.
- (92) Reddy, A.; Buckley, M. B.; Arora, A.; Bates, F. S.; Dorfman, K. D.; Grason, G. M. Stable Frank-Kasper phases of self-assembled, soft matter spheres. Proceedings of the National Academy of Sciences 2018, 115, 10233–10238.
- (93) Feng, X.; Burke, C. J.; Zhuo, M.; Guo, H.; Yang, K.; Reddy, A.; Prasad, I.; Ho, R.-M.; Avgeropoulos, A.; Grason, G. M.; Thomas, E. L. Seeing mesoatomic distortions in soft-matter crystals of a double-gyroid block copolymer. *Nature* 2019, 575, 175–179.

# Supplementary Information: Structural Relaxation and Anisotropic Elasticity of Ordered Block Copolymer Melts

Krista G. Schoonover, <sup>1</sup> Gaurav Rawat, <sup>2</sup> Emily B. Pentzer, <sup>1</sup>, <sup>2</sup> and Michael S. Dimitriyev<sup>2</sup>, \*

<sup>1</sup> Department of Chemistry, Texas A&M University, College Station, TX 77843, USA

<sup>2</sup> Department of Materials Science and Engineering,

Texas A&M University, College Station, TX 77843, USA

Polymer	Structure	$C_{\infty}$	b (Å)	$\rho \; (\mathrm{gcm}^{-3})$	$M_0 \; (\mathrm{gmol}^{-1})$
1,4-Polyisoprene (PI)	$-(CH_2CH=CHCH(CH_3))-$	4.6	8.2	0.830	113
1,4-Polybutadiene (PB)	$-(CH_2CH=CHCH_2)-$	5.3	9.6	0.826	105
Polypropylene (PP)	$-(\mathrm{CH_2CH_2}(\mathrm{CH_3}))-$	5.9	11	0.791	180
Poly(ethylene oxide) (PEO)	$-(\mathrm{CH_2CH_2O})-$	6.7	11	1.064	137
Poly(dimethyl siloxane) (PDMS)	$-(\mathrm{OSi}(\mathrm{CH}_3)_2)-$	6.8	13	0.895	381
Polyethylene (PE)	$-(\mathrm{CH_2CH_2})-$	7.4	14	0.784	150
Poly(methyl methacrylate)	$-(\mathrm{CH_2C}(\mathrm{CH_3})(\mathrm{COOCH_3})) -$	9.0	17	1.13	655
Atactic polystyrene (PS)	$-(\mathrm{CH_2CHC_6H_5})-$	9.5	18	0.969	720

TABLE S1. Characteristic ratios  $(C_{\infty})$ , Kuhn lengths (b), densities  $(\rho)$ , and molar masses of Kuhn monomers  $(M_0)$  for common polymers. Reproduced from Rubinstein textbook [1].

# S1. PARAMETERS USED FOR SCFT CALCULATIONS

In order to allow for a more general set of relaxation modes under deformation, we lifted constraints on the symmetry groups of the microphase separated patterns. This is done after first determining the free energy, monomer distributions, and chemical potential fields in the highest symmetry, undeformed "reference" configurations. For details about the symmetry group conversions, see table S2.

For the internal parameters used by the PSCF software [2], we used the following values:

- The internal ds parameter (corresponding to step sizes in the integrals over the chain backbone) is given by 0.01, increased to 0.05 for most cubic deformations with negligible impact on results as tested on gyroid structure at  $\epsilon = 1$ ,  $\chi N^{\rm ABA} = 30$ .
- Mesh size, specified by mesh, ranged from 40 for lamellae,  $48 \times 48$  up to  $80 \times 80$  for hexagonal cylinders, and  $64 \times 64 \times 64$  up to  $100 \times 100 \times 100$  for cubic structures.
- Maximum history, specified by maxHist, ranged from 10 (the set value during phase sweeps) to 30 for most deformations, with high  $\chi N$  cubic structures requiring above 200 to converge.

	Undeformed ("1	reference") configuration	Deformed ("target") configuration			
#D	Lattice Type	Symmetry Group	Lattice Type	Symmetry Group		
1D	lamellar	$Par{1}$	lamellar	$P\bar{1}$		
2D	hexagonal	p6mm	oblique	p1		
3D	cubic	$Ia\bar{3}d$ // $Im\bar{3}m$	triclinic	P1		

TABLE S2. Table showing the conversions between symmetry groups for the undeformed-deformed configurations.

<sup>\*</sup> msdim@tamu.edu

• Convergence threshold, specified by epsilon, was set at  $1 \times 10^{-5}$  for all phase sweeps and deformations.

The deformation cell parameters are given by

$$a = (1+s)a_0 \tag{S1}$$

for lamellae, where  $a_0$  is the initial lattice parameter and s is the incremental deformation, here s = 0 - 0.1 in increments of 0.01. Hexagonal deformation cell parameters are given by

$$a = (1+s)a_0$$

$$b = a_0$$

$$\gamma = \frac{2\pi}{3}$$
(S2)

for uniaxial stretch and

$$a = b = (1+s)a_0$$

$$\gamma = \frac{2\pi}{3}$$
(S3)

for isotropic biaxial stretch. A number of shear stretches were performed to evaluate monomer density relaxation as follows:

$$a = b = a_0$$

$$\gamma = (1+s)\frac{2\pi}{3}.$$
(S4)

Deformations for cubic geometries are given by the following lattice parameters for simple shear:

$$a = c = a_0$$

$$b = \frac{a_0}{\sin \gamma}$$

$$\alpha = \beta = 0$$

$$\gamma = \arctan(\frac{1}{s}).$$
(S5)

and the following lattice parameters for simple extension:

$$a = (1+s)a_0$$

$$b = c = \frac{a_0}{\sqrt{1+s}}$$

$$\alpha = \beta = 0$$

$$\gamma = \frac{\pi}{2}.$$
(S6)

## S2. EXTRACTING 2D MODULI FROM SCFT

Two protocols are used here: uniaxial stretching of one axis and isotropic biaxial stretching in 2D.

#### A. Uniaxial stretch

In the case of uniaxial stretching the lattice parameters are determined as a function of the stretch parameter s as follows:

$$a = a_0(1+s)$$

$$b = a_0$$

$$\theta = \frac{2\pi}{3}$$
(S7)

Therefore, the strain is given by

$$\mathbf{u} \approx \begin{pmatrix} s & 0 \\ 0 & 0 \end{pmatrix} \tag{S8}$$

The deformation free energy per volume is then given by

$$\Delta \mathcal{F} = \frac{1}{2} \left[ 2\mu_{\perp} (u_{xx}^2 + u_{yy}^2 + 2u_{xy}u_{yx}) + \lambda_{\perp} (u_{xx} + u_{yy})^2 \right]$$

$$= \frac{1}{2} \left[ 2\mu_{\perp} s^2 + \lambda_{\perp} s^2 \right]$$

$$= \frac{1}{2} (2\mu_{\perp} + \lambda_{\perp}) s^2 = \frac{1}{2} A_1 s^2$$
(S9)

## B. Isotropic biaxial stretch

In the case of uniaxial stretching the lattice parameters are determined as a function of the stretch parameter s as follows:

$$a = a_0(1+s)$$

$$b = a_0(1+s)$$

$$\theta = \frac{2\pi}{3}$$
(S10)

Therefore, the strain is given by

$$\mathbf{u} \approx \begin{pmatrix} s & 0 \\ 0 & s \end{pmatrix} \tag{S11}$$

The deformation free energy per volume is then given by

$$\Delta \mathcal{F} = \frac{1}{2} \left[ 2\mu_{\perp} (u_{xx}^2 + u_{yy}^2 + 2u_{xy}u_{yx}) + \lambda_{\perp} (u_{xx} + u_{yy})^2 \right]$$

$$= \frac{1}{2} \left[ 4\mu_{\perp} s^2 + 4\lambda_{\perp} s^2 \right]$$

$$= 2(\mu_{\perp} + \lambda_{\perp}) s^2 = \frac{1}{2} A_2 s^2$$
(S12)

## C. Deriving moduli from applied stretches

Together, the applied uniaxial and isotropic biaxial stretches provide a system of 2 equations with 2 unknowns, for which we can solve  $\lambda_{\perp}$  and  $\mu_{\perp}$ . Subtracting  $2 \times 89$  from 812 gives

$$\lambda_{\perp} = -A_1 + \frac{1}{2}A_2 \tag{S13}$$

and subtracting S12 from  $4 \times S9$  gives

$$\mu_{\perp} = A_1 - \frac{1}{4}A_2 \tag{S14}$$

The shear modulus is given by  $\mu$  and the Young's modulus by  $Y_{\parallel}=\lambda_{\perp}+\mu_{\perp}$ . For any  $f_{\rm A}$  with converged uniaxial and isotropic biaxial stretches, we can now calculate  $Y_{\parallel}$  and  $\mu_{\perp}$  for the 2D case.

# S3. RIGIDITY FIGURES AND TABLES

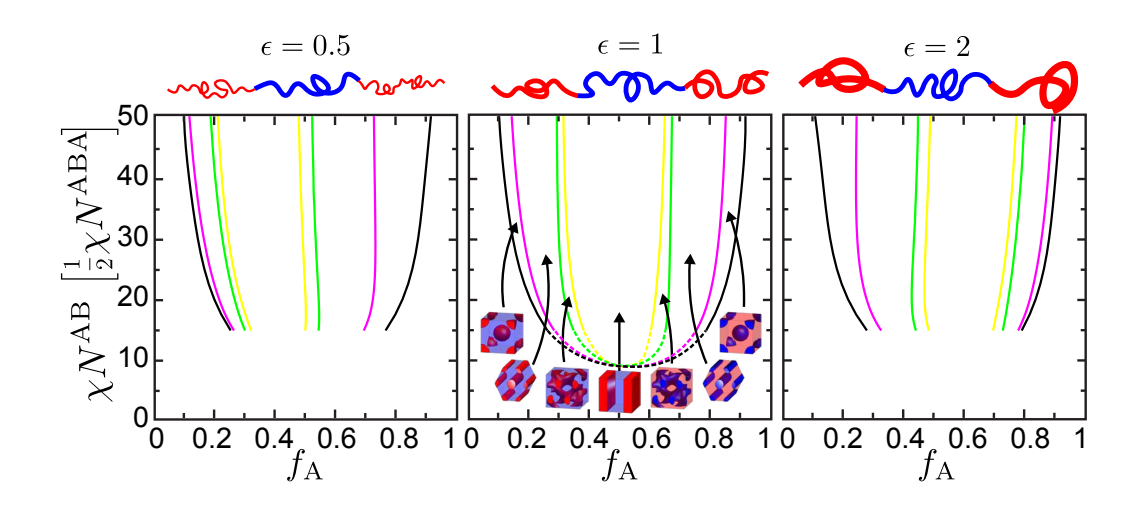


FIG. S1. Phase diagrams for all 3  $\epsilon$ .

## A. Lamellae

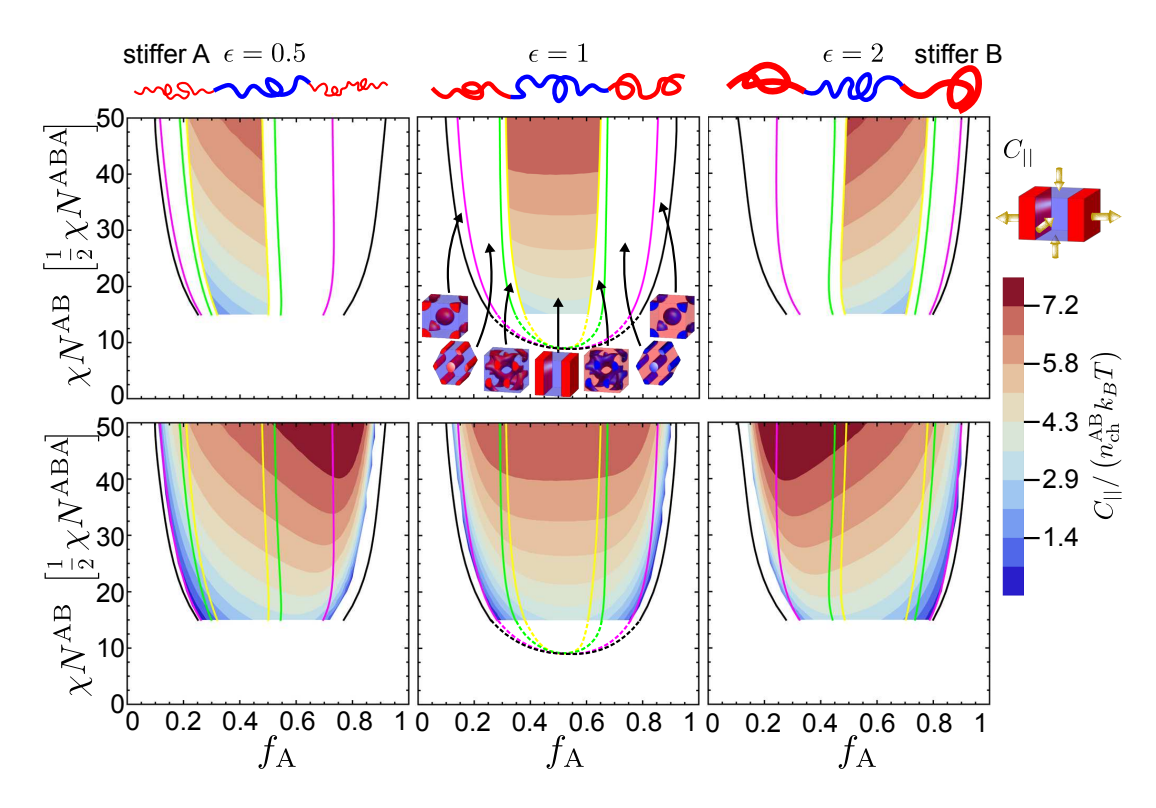


FIG. S2. Lamellar heat maps of longitudinal modulus for ABA, comparing results within the stability window (top) to the full metastable region (bottom).

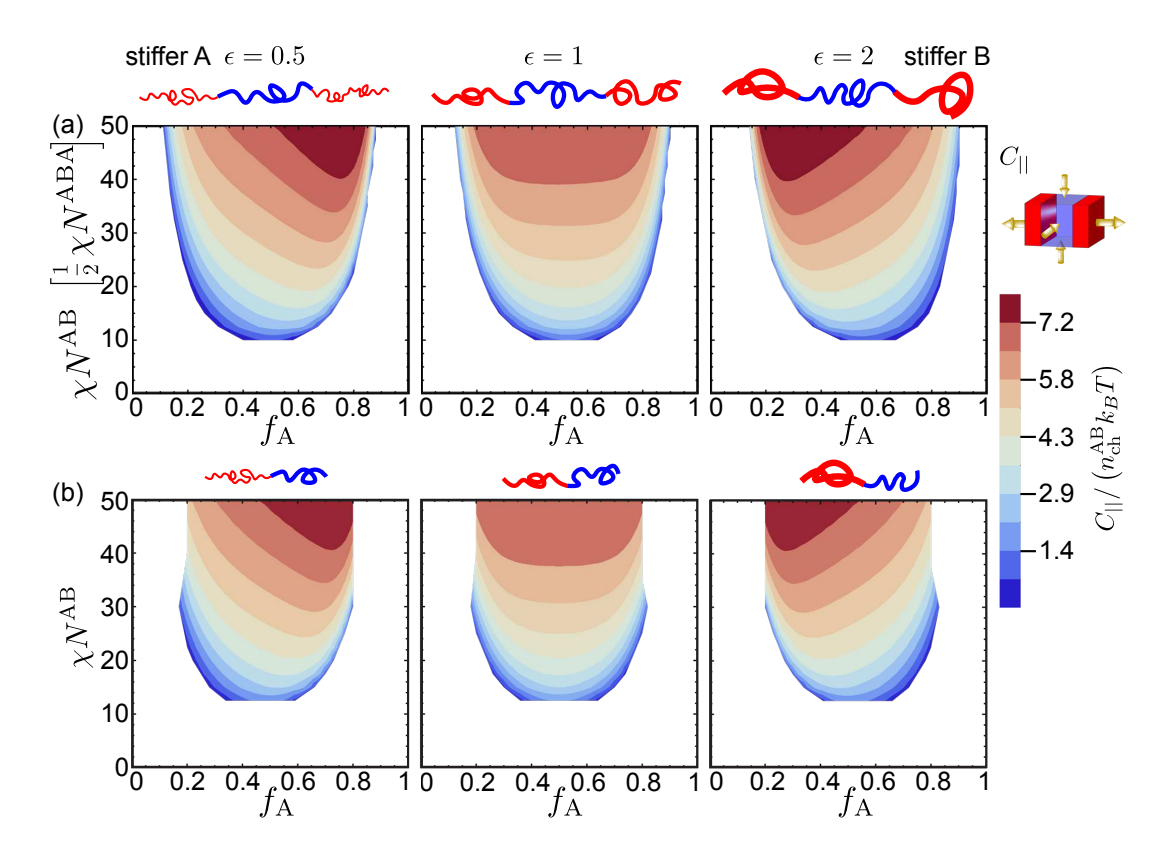


FIG. S3. Lamellar heat maps of longitudinal modulus for (a) ABA and (b) AB, plotted on the same modulus scale.

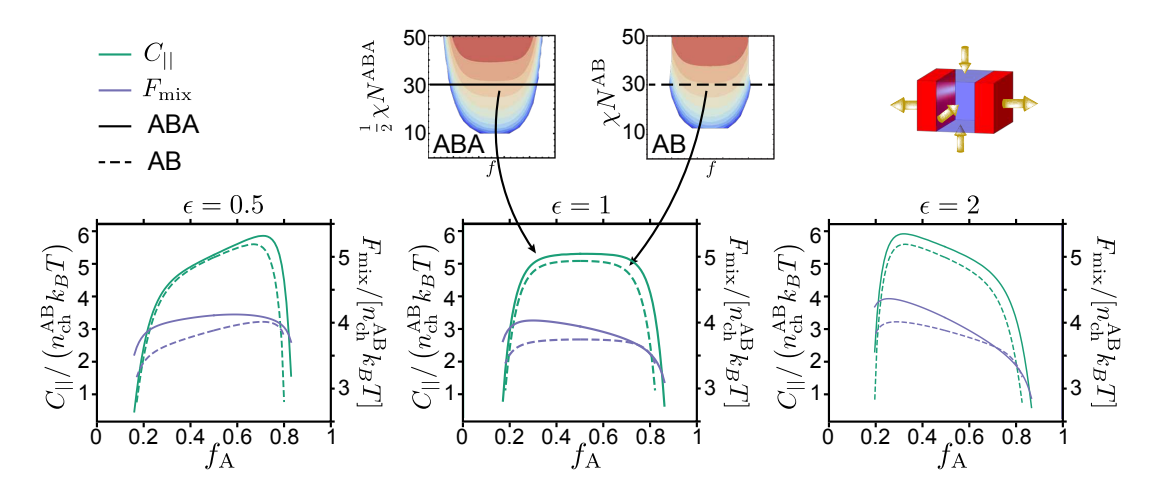


FIG. S4. Lamellar plots of longitudinal modulus and free energy vs  $f_{\rm A}$  for  $\chi N^{\rm AB}=30.$ 

The maximum longitudinal moduli,  $C_{||,\text{max}}$ , and  $f_A$  at  $C_{||,\text{max}}$  are shown in Tables S3 (for ABA) and S4 (for AB). It is our hope that these values can serve as a useful guide for future theoretical and experimental studies. A graphical representation of  $C_{||,\text{max}}$  and associated  $f_A$  is shown in Figure S5. Notably,  $f_A$  have some numerical fluctuations at high  $\chi N$  for ABA and AB for  $\epsilon = 1$ , but in general  $f_A^{AB} = 0.5$  whereas  $f_A^{ABA} \neq 0.5$ . For configurational asymmetry,  $f_A$  increases with  $\chi N$  for  $\epsilon = 0.5$  with a greater effect for ABA than AB, whereas  $f_A$  decreases with  $\chi N$  for  $\epsilon = 2$  and is overlapping for ABA and AB.

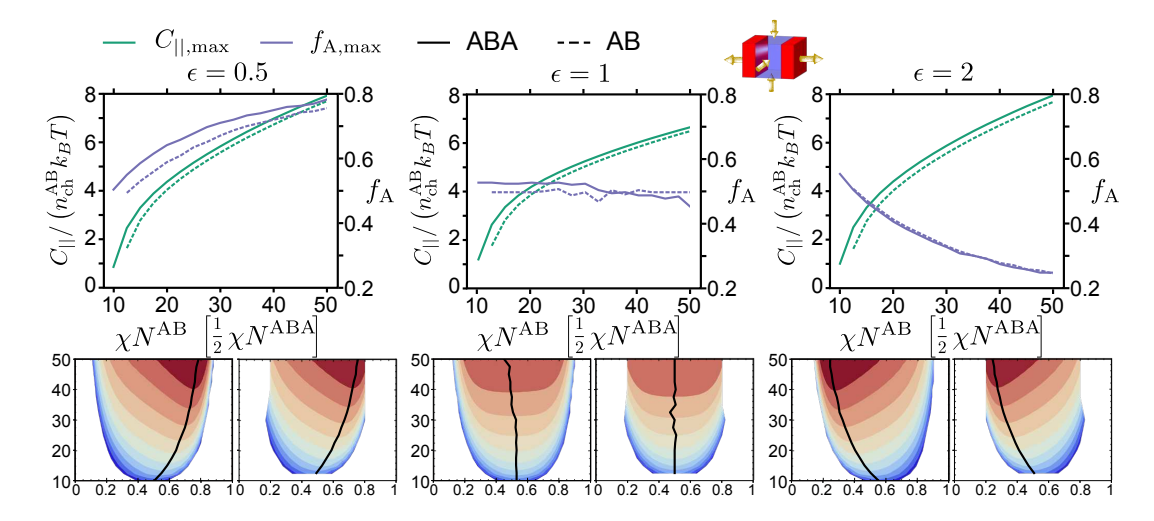


FIG. S5.  $C_{||, \mathrm{max}}$  and  $f_{\mathrm{max}}$  for ABA and AB lamellae, plotted against  $\chi N^{\mathrm{AB}}$ .

$ABA_{1D}$	$\epsilon = 0.5$		$\epsilon =$	1	$\epsilon =$	2
$\chi N$	$C_{  ,\max}$	$f_{ m A}$	$C_{  ,\max}$	$f_{ m A}$	$C_{  ,\max}$	$f_{ m A}$
12.5	2.439	0.549	2.655	0.530	2.499	0.504
15	3.281	0.585	3.386	0.527	3.322	0.465
17.5	3.876	0.615	3.868	0.527	3.919	0.435
20	4.359	0.642	4.238	0.530	4.408	0.405
22.5	4.777	0.658	4.546	0.527	4.831	0.382
25	5.158	0.678	4.818	0.530	5.215	0.362
27.5	5.508	0.698	5.062	0.523	5.566	0.342
30	5.835	0.711	5.289	0.527	5.895	0.325
32.5	6.147	0.721	5.499	0.507	6.204	0.306
35	6.444	0.734	5.700	0.497	6.499	0.299
37.5	6.721	0.741	5.889	0.500	6.776	0.289
40	6.992	0.751	6.071	0.490	7.037	0.272
42.5	7.242	0.761	6.243	0.490	7.293	0.262
45	7.489	0.764	6.405	0.480	7.538	0.256
47.5	7.722	0.771	6.564	0.487	7.767	0.246
50	7.947	0.784	6.716	0.450	7.992	0.246

TABLE S3.  $f_A$  and modulus in units of  $n_{ch}^{AB}k_BT$  for the maximum longitudinal modulus for ABA lamellae.

$AB_{1D}$	$\epsilon = 0.5$		$\epsilon =$	: 1	$\epsilon =$	: 2
$\chi N$	$C_{  ,\max}$	$f_{ m A}$	$C_{  ,\max}$	$f_{ m A}$	$C_{  ,\mathrm{max}}$	$f_{ m A}$
12.5	1.602	0.493	1.780	0.500	1.602	0.507
15	2.758	0.529	2.852	0.500	2.758	0.471
17.5	3.481	0.559	3.481	0.500	3.481	0.441
20	4.027	0.589	3.923	0.500	4.027	0.411
22.5	4.479	0.608	4.273	0.503	4.478	0.388
25	4.879	0.635	4.570	0.510	4.880	0.368
27.5	5.241	0.651	4.833	0.490	5.242	0.349
30	5.580	0.671	5.073	0.500	5.579	0.329
32.5	5.898	0.688	5.293	0.470	5.897	0.312
35	6.197	0.701	5.502	0.507	6.197	0.299
37.5	6.475	0.711	5.700	0.493	6.475	0.289
40	6.745	0.721	5.883	0.507	6.745	0.276
42.5	7.005	0.731	6.064	0.500	7.003	0.269
45	7.251	0.744	6.233	0.500	7.249	0.256
47.5	7.492	0.747	6.399	0.500	7.489	0.253
50	7.721	0.757	6.553	0.500	7.720	0.243

TABLE S4.  $f_{\rm A}$  and modulus in units of  $n_{\rm ch}^{\rm AB}k_BT$  for the maximum longitudinal modulus for AB lamellae.

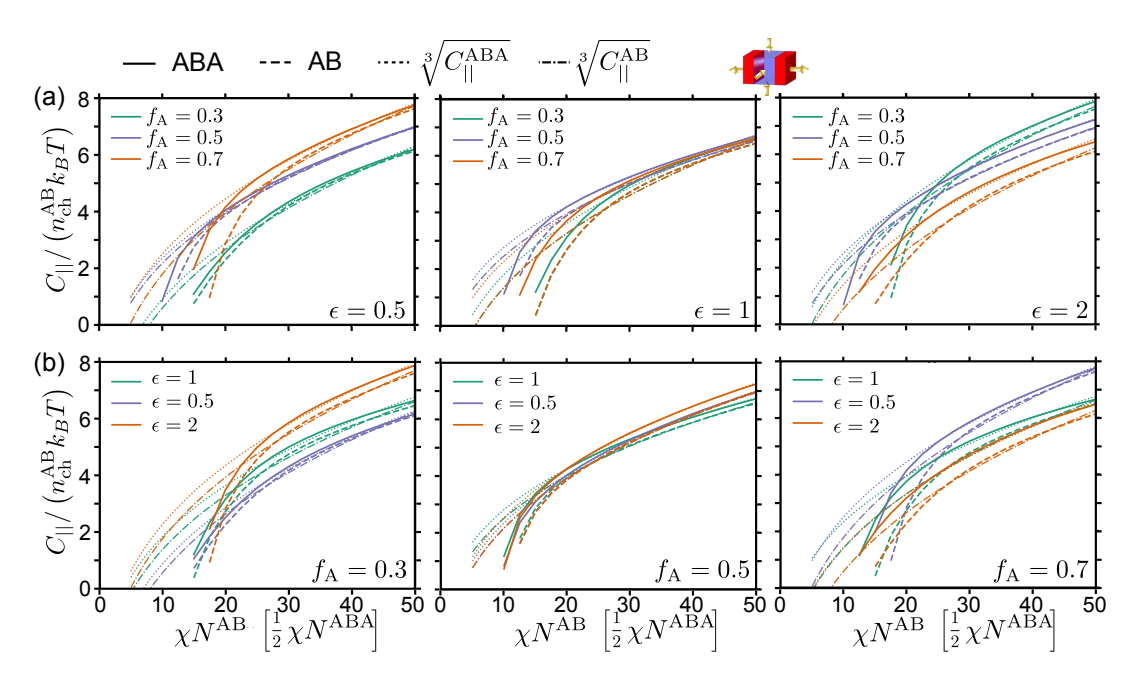


FIG. S6. 1D  $\chi N$  vs longitudinal modulus, grouped by (a)  $\epsilon$  or (b)  $f_{\rm A}$  value.

## B. Columnar Phase

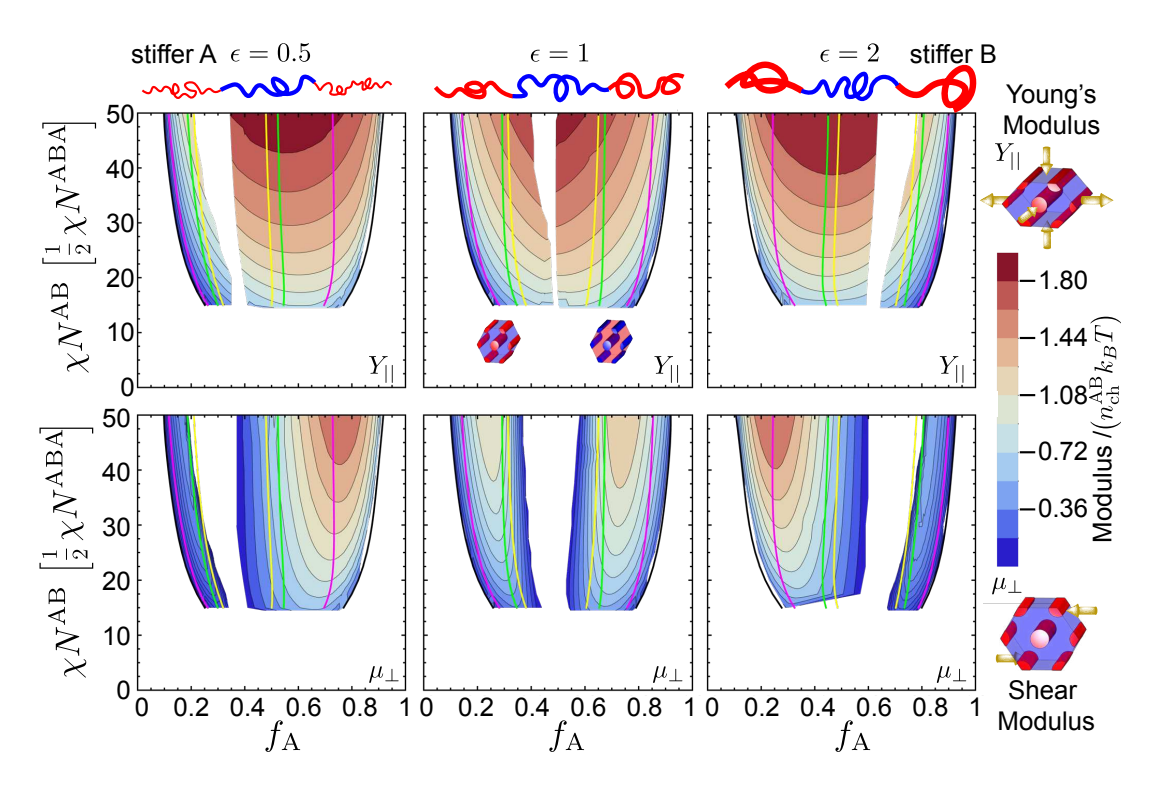


FIG. S7. Full modulus heat map for columnar phase, including metastable regions. Results plotted into middle of lamellar region, or to ends of converged structures.

The maximum Young's and shear moduli,  $Y_{||}$  and  $\mu_{\perp}$ , and  $f_{\rm A}$  at the respective maxima are shown in Tables S6 - S8, grouped by  $\epsilon$ , with an overview for  $\chi N^{\rm AB} = 30$  shown in Table S5. A graphical representation of  $Y_{||,\rm max}$ ,  $f_{Y,\rm max}$  and  $\mu_{\perp,\rm max}$ ,  $f_{\mu,\rm max}$  is shown in Figure S8.

2D		AI	AB					
		low $f_{\rm A}$		high $f_{\rm A}$	low	$f_{ m A}$	high $f_{\rm A}$	
$\epsilon$	$\mu_{\perp}$	$f_{\rm A}$ (bounds)	$\mu_{\perp}$ $f_{\rm A}$ (bounds)		$\mu_{\perp}$	$f_{ m A}$	$\mu_{\perp}$	$f_{ m A}$
0.5	0.35	0.22 (0.16-0.22)	1.21	0.74 (0.53-0.73)	0.41	0.23	1.08	0.72
1.0	0.78	0.27 (0.18-0.30)	0.95	$0.72 \ (0.67 - 0.83)$	0.80	0.28	0.80	0.72
2.0	1.14 0.27 (0.25-0.44)		0.44	0.80 (0.78-0.86)	1.08	0.28	0.41	0.77

TABLE S5. Maximum shear modulus and associated  $f_A$  for the given  $\epsilon$  at  $\chi N^{AB} = 30$  for columnar ABA and AB.

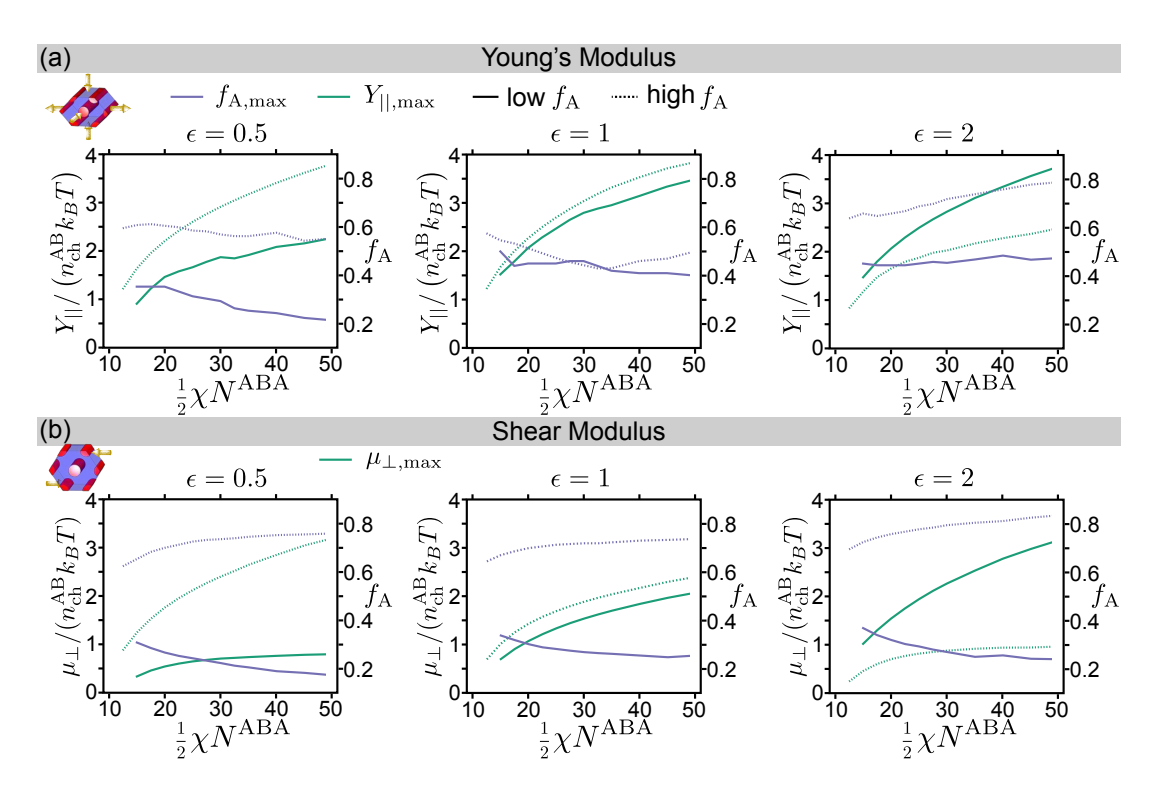


FIG. S8.  $Y_{\parallel,\text{max}}$  and  $\mu_{\perp,\text{max}}$  and their corresponding  $f_{\text{max}}$  for ABA cylinders, plotted against  $\chi N$ .

$2D \epsilon = 1$		low $f_{\rm A}$ (E	3 matrix)			high $f_{\rm A}$ (A	A matrix)	
$\chi N^{ m AB}$	$Y_{  }$	$f_{ m A}$	$\mu_{\perp}$	$f_{ m A}$	$Y_{  }$	$f_{ m A}$	$\mu_{\perp}$	$f_{ m A}$
12.5					1.223	0.575	0.706	0.647
15	1.524	0.500*	0.711	0.340	1.675	0.546	1.029	0.673
17.5	1.791	0.440*	0.920	0.321	2.005	0.533	1.265	0.689
20	2.072	0.450*	1.087	0.304	2.274	0.513	1.445	0.702
22.5	2.288	0.450*	1.228	0.291	2.501	0.493	1.588	0.709
25	2.471	0.450*	1.350	0.284	2.700	0.473	1.706	0.716
27.5	2.654	0.460*	1.458	0.277	2.879	0.456	1.810	0.719
30	2.799	0.460*	1.552	0.271	3.041	0.443	1.901	0.722
32.5	2.886	0.440*	1.637	0.267	3.190	0.430*	1.982	0.722
35	2.957	0.420*	1.715	0.264	3.323	0.430*	2.055	0.726
40	3.147	0.410*	1.855	0.257	3.533	0.460*	2.186	0.733
45	3.342	0.410*	1.981	0.250	3.719	0.470*	2.312	0.736
50	3.491	0.400*	2.088	0.257	3.850	0.500*	2.415	0.740

TABLE S6. Maximum shear and Young's moduli (in units of  $n_{\rm ch}k_BT$ ) and their associated  $f_{\rm A}$  for  $\epsilon=1$  for columnar ABA. \* corresponds to values that were not local maxima, but simply the limit of computational testing (deformations failed for B matrix f\*). For reference,  $f_{\rm A}$  stability region bounds for  $\chi N^{\rm AB}=30$  are 0.18-0.30 for low  $f_{\rm A}$  and 0.67-0.83 for high  $f_{\rm A}$ .

$2D \epsilon = 0.5$		low $f_{\rm A}$ (E	3 matrix)			high $f_{\rm A}$ (.	A matrix)	
$\chi N^{ m AB}$	$Y_{  }$	$f_{ m A}$	$\mu_{\perp}$	$f_{ m A}$	$Y_{  }$	$f_{ m A}$	$\mu_{\perp}$	$f_{ m A}$
12.5					1.198	0.593	0.866	0.625
15	0.895	0.350*	0.320	0.306	1.627	0.606	1.238	0.655
17.5	1.208	0.350*	0.444	0.283	1.944	0.610	1.526	0.685
20	1.451	0.350*	0.529	0.264	2.198	0.603	1.761	0.702
22.5	1.567	0.330*	0.589	0.250	2.411	0.597	1.957	0.715
25	1.653	0.310*	0.635	0.240	2.596	0.583	2.125	0.728
27.5	1.766	0.300*	0.667	0.230	2.760	0.580	2.275	0.735
30	1.863	0.290*	0.694	0.220	2.908	0.567	2.408	0.738
32.5	1.838	0.260*	0.709	0.209	3.044	0.560	2.528	0.742
35	1.907	0.250*	0.725	0.202	3.171	0.560	2.655	0.748
40	2.076	0.240*	0.751	0.186	3.407	0.574	2.863	0.755
45	2.150	0.220*	0.773	0.179	3.616	0.541	3.060	0.758
50	2.263	0.210*	0.786	0.169	3.806	0.551	3.210	0.762

TABLE S7. Maximum shear and Young's moduli (in units of  $n_{\rm ch}k_BT$ ) and their associated  $f_{\rm A}$  for  $\epsilon=0.5$  for columnar ABA. \* corresponds to values that were not local maxima, but simply the limit of computational testing (deformations failed for B matrix f\*.) For reference,  $f_{\rm A}$  stability region bounds for  $\chi N^{\rm AB}=30$  are 0.16-0.22 for low  $f_{\rm A}$  and 0.53-0.73 for high  $f_{\rm A}$ .

$2D \epsilon = 2$		low f <sub>A</sub> (I	3 matrix)			high $f_{\rm A}$ (A	A matrix)	
$\chi N^{ m AB}$	$Y_{  }$	$f_{ m A}$	$\mu_{\perp}$	$f_{ m A}$	$Y_{  }$	$f_{ m A}$	$\mu_{\perp}$	$f_{ m A}$
12.5					0.840	0.640*	0.250	0.697
15	1.481	0.453	1.029	0.371	1.182	0.660*	0.466	0.727
17.5	1.807	0.446	1.309	0.342	1.485	0.650*	0.612	0.746
20	2.076	0.446	1.552	0.322	1.661	0.660*	0.712	0.760
22.5	2.306	0.446	1.763	0.305	1.803	0.670*	0.778	0.770
25	2.506	0.453	1.954	0.295	1.886	0.690*	0.827	0.780
27.5	2.682	0.460	2.126	0.282	1.989	0.700*	0.861	0.787
30	2.840	0.456	2.278	0.272	2.037	0.720*	0.888	0.797
35	3.123	0.470	2.545	0.252	2.182	0.740*	0.927	0.807
40	3.355	0.486	2.792	0.258	2.291	0.760*	0.950	0.814
45	3.578	0.469	2.993	0.244	2.379	0.780*	0.953	0.828
50	3.775	0.476	3.174	0.242	2.498	0.790*	0.974	0.838

TABLE S8. Maximum shear and Young's moduli (in units of  $n_{\rm ch}k_BT$ ) and their associated  $f_{\rm A}$  for  $\epsilon=2$  for columnar ABA. \* corresponds to values that were not local maxima, but simply the limit of computational testing (deformations failed for B matrix f\*.) For reference,  $f_{\rm A}$  stability region bounds for  $\chi N^{\rm AB}=30$  are 0.25-0.44 for low  $f_{\rm A}$  and 0.78-0.86 for high  $f_{\rm A}$ .

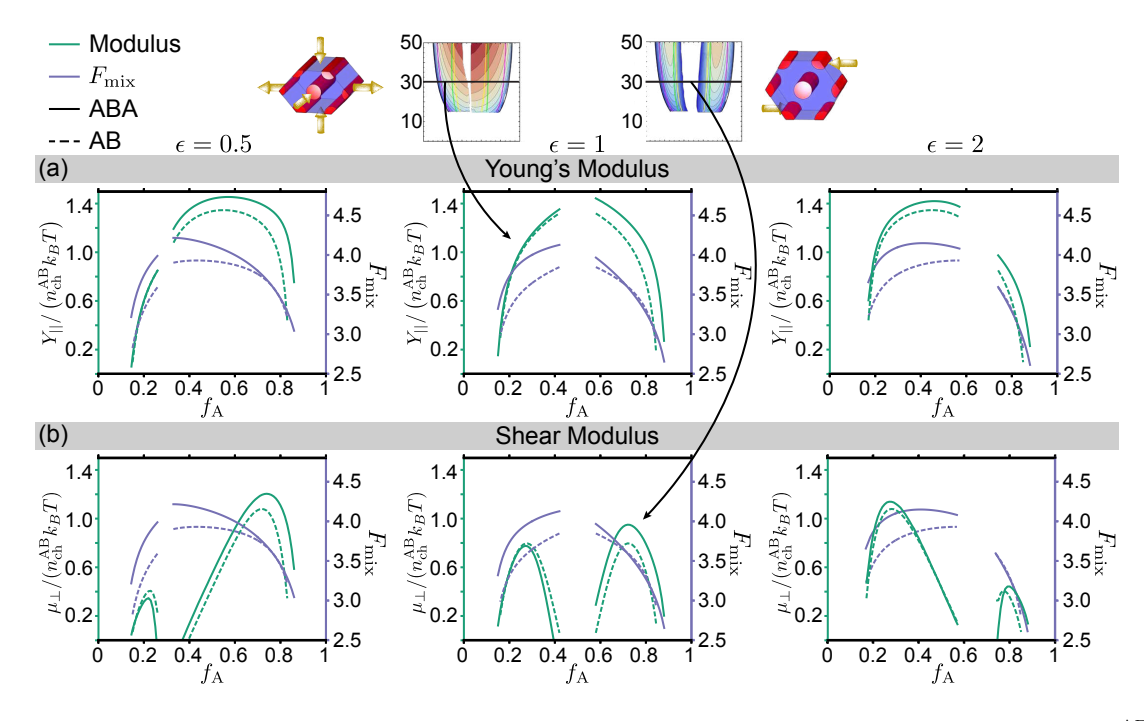


FIG. S9. Plots of (a) Young's modulus and free energy and (b) shear modulus and free energy vs  $f_A$  for  $\chi N^{AB}=30$  for columnar phase, comparing ABA and AB.

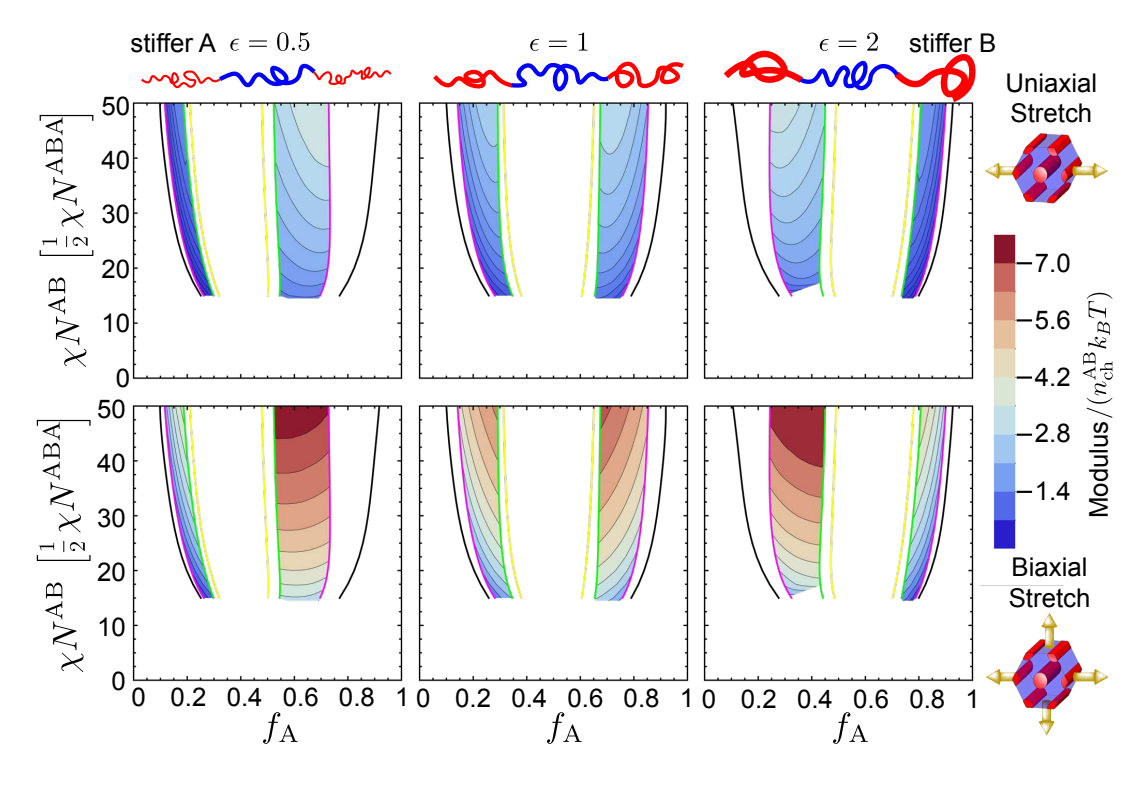


FIG. S10. Modulus heat map for columnar phase for original deformations (uniaxial and biaxial stretch), plotted within the stable phase regions.

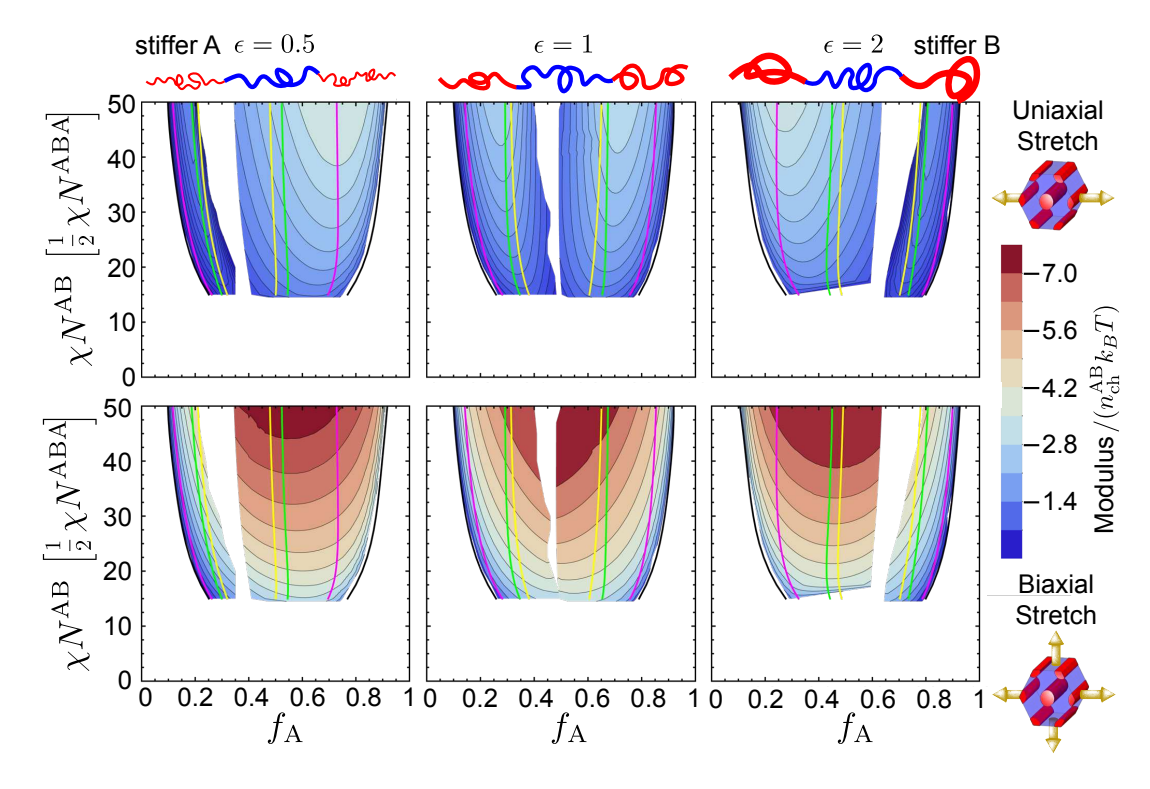


FIG. S11. Full modulus heat map for columnar phase for original deformations (uniaxial and biaxial stretch), including metastable regions. Results plotted into middle of lamellar region, or to ends of converged structures.

# C. Cubic Phases

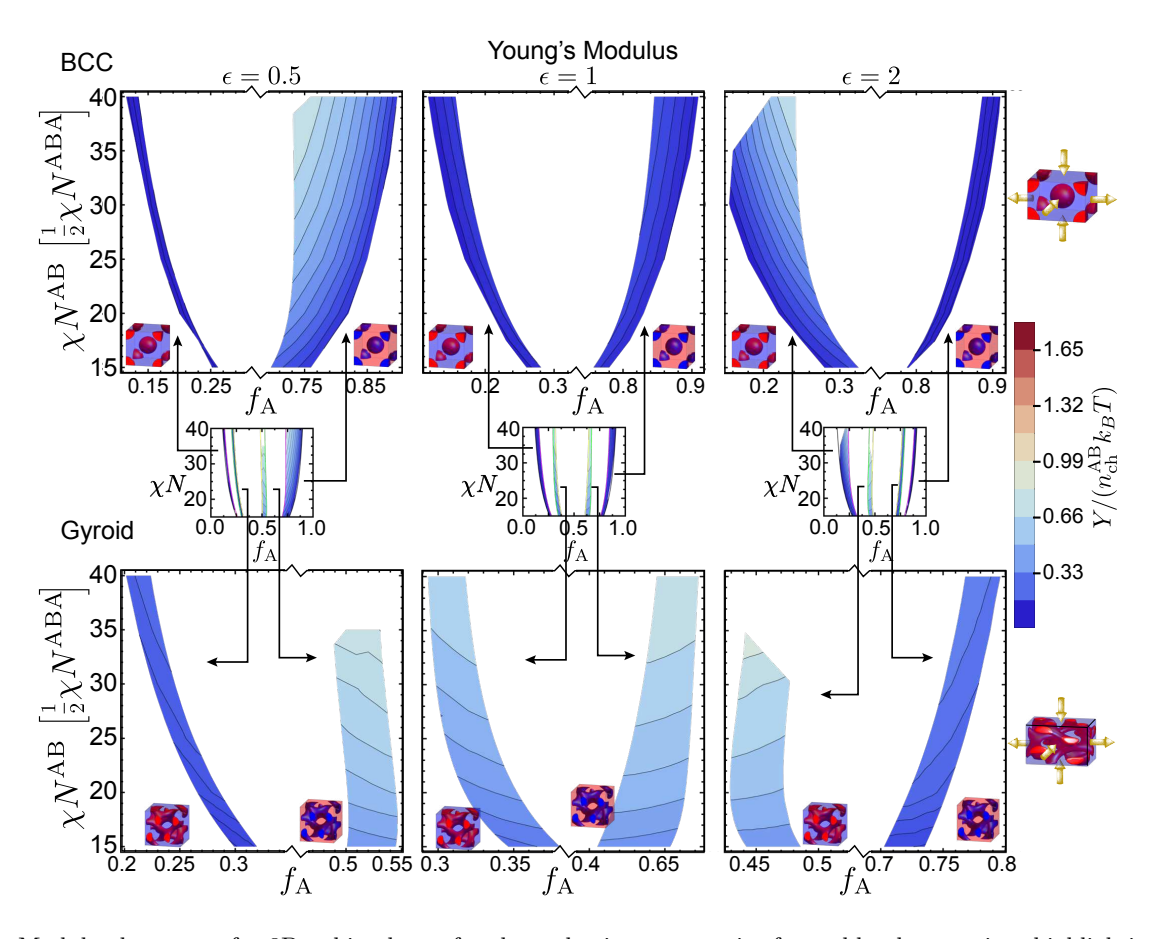


FIG. S12. Modulus heat map for 3D cubic phases for three elastic asymmetries for stable phase region, highlighting Young's modulus for BCC (top) and gyroid (bottom).

BCC: $\epsilon = 1$		low f <sub>A</sub> (I	3 matrix)		high $f_{\rm A}$ (A matrix)			
$\chi N^{ m AB}$	Y	$f_{ m A}$	$\mu$	$f_{ m A}$	Y	$f_{ m A}$	$\mu$	$f_{ m A}$
15	0.305	0.410	0.549	0.354	0.114	0.730	0.316	0.735
17.5	0.386	0.404	0.704	0.323	0.103	0.770	0.268	0.781
20	0.453	0.379	0.844	0.296	0.130	0.750	0.317	0.792
25	0.571	0.361	1.093	0.265	0.115	0.785	0.370	0.822
30	0.673	0.329	1.307	0.252	0.106	0.810	0.490	0.835
35	0.624	0.250	1.491	0.234	0.096	0.830	0.394	0.859
40	0.711	0.250	1.648	0.224	0.103	0.830	0.437	0.866

TABLE S9.  $f_A$  and modulus in units of  $n_{ch}k_BT$  for the maximum shear and Young's modulus for  $\epsilon=1$  for BCC spheres ABA. \* corresponds to values that were not local maxima, but simply the limit of computational testing (deformations failed for B matrix  $f^*$ .

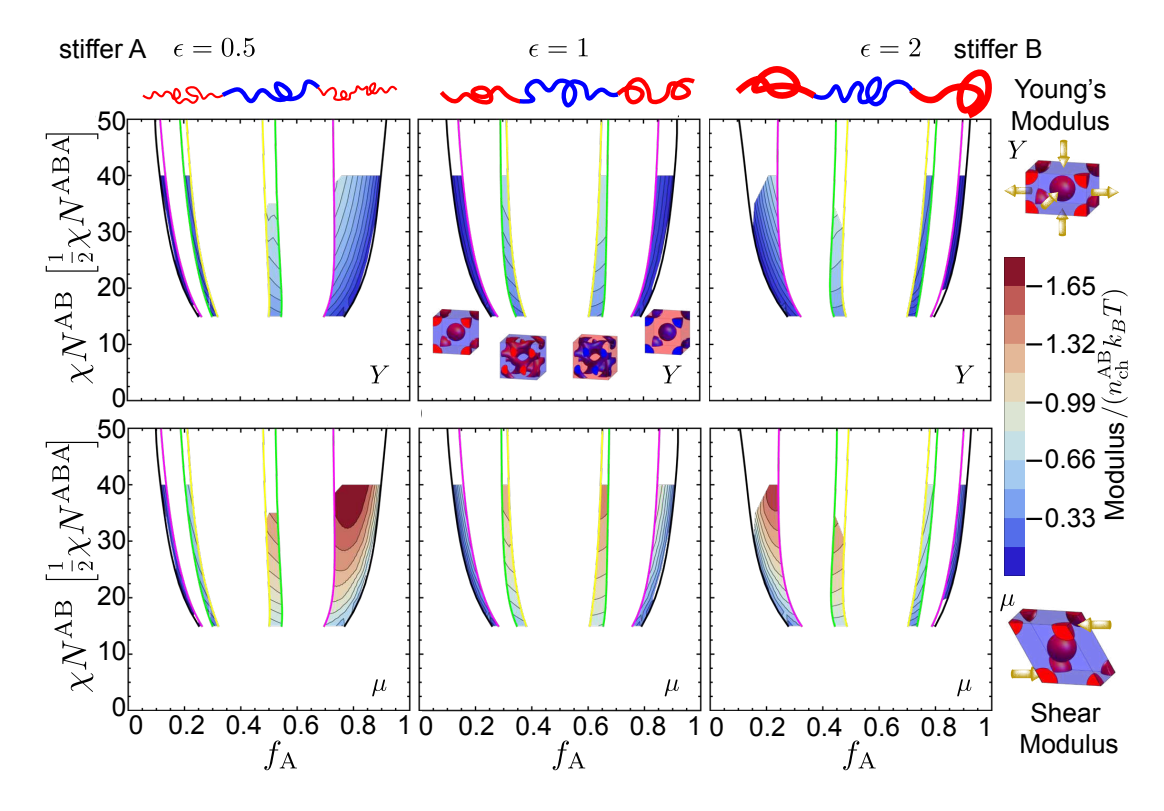


FIG. S13. Modulus heat map for 3D cubic phases for three elastic asymmetries for stable phase region, highlighting Young's modulus (top) and shear modulus (bottom) on regular scale  $f_A$ .

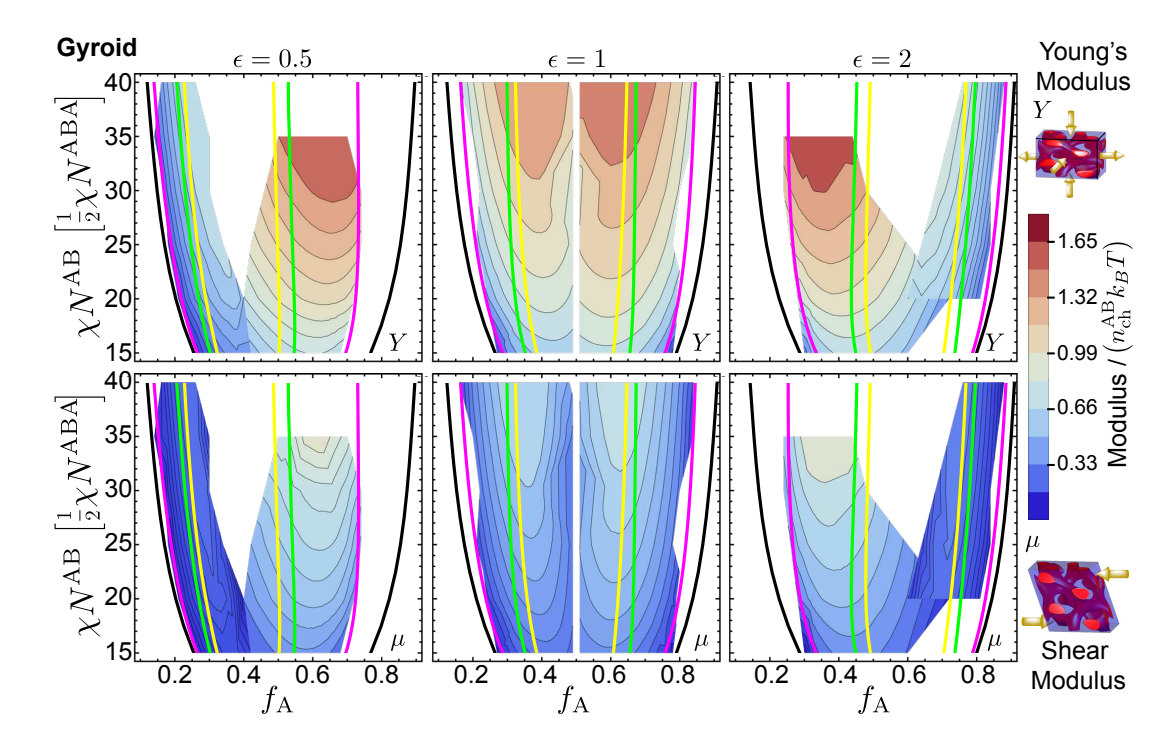


FIG. S14. Modulus heat map for gyroid phase for three elastic asymmetries including metastable regions, separated into Young's modulus (top) and shear modulus (bottom).

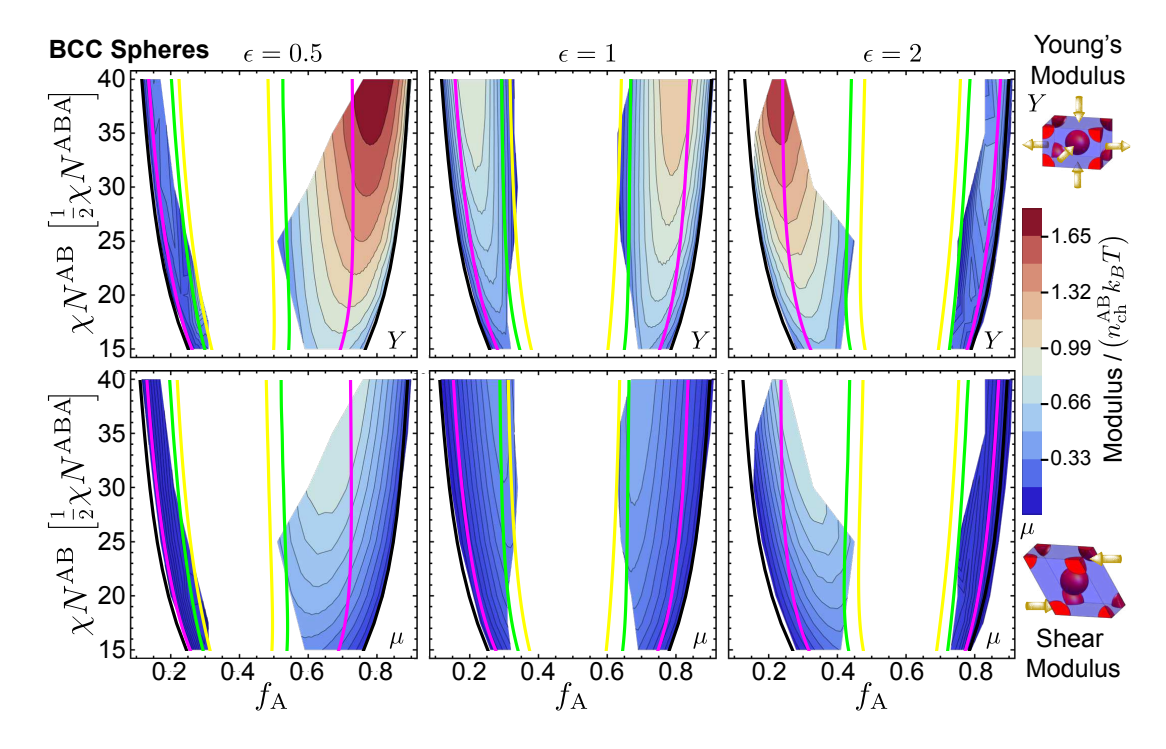


FIG. S15. Modulus heat map for BCC spheres for three elastic asymmetries including metastable regions, separated into Young's modulus (top) and shear modulus (bottom).

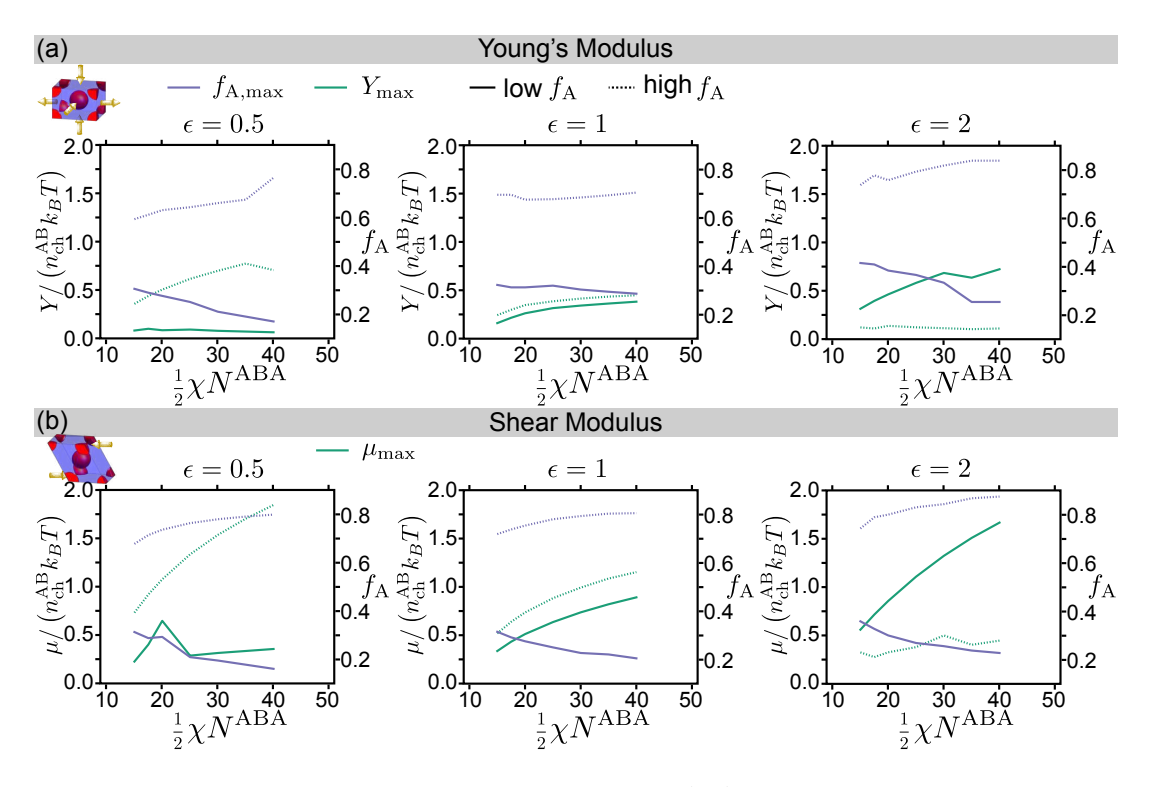


FIG. S16.  $Y_{\rm max}$  and  $\mu_{\rm max}$  and their corresponding  $f_{\rm max}$  for ABA BCC spheres, plotted against  $\chi N$ .

BCC: $\epsilon = 0.5$		low $f_{\rm A}$ (I	3 matrix)		high $f_{\rm A}$ (A matrix)				
$\chi N^{ m AB}$	Y	$f_{ m A}$	$\mu$	$f_{ m A}$	Y	$f_{ m A}$	μ	$f_{\mathrm{A}}$	
15	0.356	0.590	0.724	0.672	0.082	0.304	0.222	0.310	
17.5	0.436	0.608	0.910	0.708	0.100	0.288	0.396	0.285	
20	0.502	0.627	1.066	0.730	0.085	0.275	0.640	0.290	
25	0.612	0.639	1.322	0.757	0.092	0.250	0.283	0.207	
30	0.695	0.656	1.522	0.773	0.079	0.210	0.310	0.193	
40	0.702	0.760	1.829	0.792	0.064	0.170	0.351	0.159	

TABLE S10.  $f_A$  and modulus in units of  $n_{ch}k_BT$  for the maximum shear and Young's modulus for  $\epsilon=0.5$  for BCC spheres ABA. \* corresponds to values that were not local maxima, but simply the limit of computational testing (deformations failed for B matrix f\*.

BCC: $\epsilon = 2$		low $f_{\rm A}$ (I	3 matrix)		high $f_{\rm A}$ (A matrix)				
$\chi N^{ m AB}$	Y	$f_{ m A}$	$\mu$	$f_{ m A}$	Y	$f_{ m A}$	$\mu$	$f_{ m A}$	
15	0.240	0.690	0.511	0.712	0.158	0.320	0.330	0.311	
17.5	0.295	0.690	0.630	0.731	0.213	0.310	0.426	0.288	
20	0.343	0.670	0.726	0.747	0.259	0.310	0.504	0.272	
25	0.382	0.672	0.872	0.773	0.312	0.317	0.627	0.247	
30	0.410	0.679	0.981	0.786	0.338	0.301	0.727	0.224	
35	0.430	0.688	1.074	0.796	0.359	0.292	0.810	0.218	
40	0.444	0.699	1.140	0.798	0.378	0.284	0.881	0.202	

TABLE S11.  $f_A$  and modulus in units of  $n_{ch}k_BT$  for the maximum shear and Young's modulus for  $\epsilon=2$  for BCC spheres ABA. \* corresponds to values that were not local maxima, but simply the limit of computational testing (deformations failed for B matrix  $f_*$ .

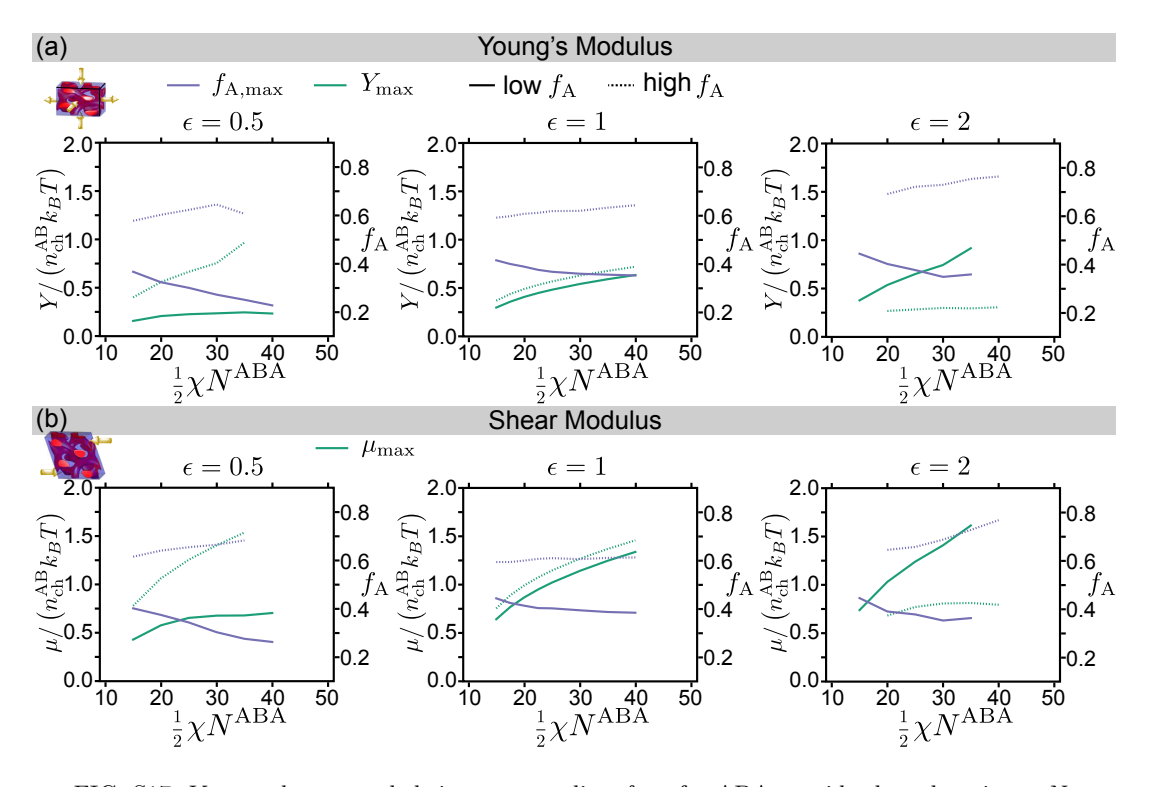


FIG. S17.  $Y_{\text{max}}$  and  $\mu_{\text{max}}$  and their corresponding  $f_{\text{max}}$  for ABA gyroid, plotted against  $\chi N$ .

GYR: $\epsilon = 1$		low $f_{\rm A}$ (	B matrix)		high $f_{\rm A}$ (A matrix)				
$\chi N^{ m AB}$	Y	$f_{ m A}$	$\mu$	$f_{ m A}$	Y	$f_{ m A}$	$\mu$	$f_{ m A}$	
15	0.610	0.416	1.266	0.439	0.752	0.591	1.489	0.588	
17.5	0.730	0.401	1.515	0.420	0.888	0.597	1.756	0.588	
20	0.827	0.390	1.712	0.409	0.991	0.607	1.958	0.594	
22.5	0.908	0.377	1.876	0.399	1.074	0.611	2.124	0.601	
25	0.977	0.371	2.018	0.397	1.146	0.618	2.267	0.605	
30	1.094	0.357	2.257	0.380*	1.267	0.619	2.508	0.600*	
35	1.191	0.357	2.466	0.383	1.362	0.632	2.709	0.605	
40	1.278	0.354	2.647	0.380	1.448	0.642	2.885	0.607	

TABLE S12.  $f_A$  and modulus in units of  $n_{ch}k_BT$  for the maximum shear and Young's modulus for  $\epsilon=1$  for gyroid ABA. \* corresponds to values that were not local maxima, but simply the limit of computational testing (deformations failed for B matrix f\*.

GYR: $\epsilon = 0.5$	low $f_{\rm A}$ (B matrix)				high $f_{\rm A}$ (A matrix)			
$\chi N^{ m AB}$	Y	$f_{ m A}$	$\mu$	$f_{ m A}$	Y	$f_{ m A}$	$\mu$	$f_{ m A}$
15	0.335	0.368	0.847	0.398	0.820	0.578	1.543	0.610
20	0.434	0.322	1.134	0.360	1.133	0.603	2.105	0.635
25	0.473	0.303	1.294	0.340	1.343	0.623	2.488	0.649
30	0.491	0.275	1.339	0.300	1.521	0.645	2.785	0.659
35	0.511	0.254	1.345	0.273	1.944	0.607	3.046	0.677
40	0.487	0.231	1.394	0.260				

TABLE S13.  $f_A$  and modulus in units of  $n_{ch}k_BT$  for the maximum shear and Young's modulus for  $\epsilon = 0.5$  for gyroid ABA. \* corresponds to values that were not local maxima, but simply the limit of computational testing (deformations failed for B matrix  $f_*$ .

GRY: $\epsilon = 2$	low $f_{\rm A}$ (B matrix)				high $f_{\rm A}$ (A matrix)			
$\chi N^{ m AB}$	Y	$f_{ m A}$	$\mu$	$f_{ m A}$	Y	$f_{ m A}$	$\mu$	$f_{ m A}$
15	0.759	0.443	1.454	0.440				
20	1.073	0.401	2.034	0.385	0.541	0.688	1.341	0.638
25	1.299	0.376	2.448	0.373	0.573	0.718	1.519	0.650
30	1.484	0.348	2.784	0.348	0.603	0.726	1.590	0.680
35	1.829	0.358	3.191	0.358	0.594	0.750	1.600	0.720
40					0.616	0.760	1.564	0.760

TABLE S14.  $f_A$  and modulus in units of  $n_{ch}k_BT$  for the maximum shear and Young's modulus for  $\epsilon=2$  for gyroid ABA. \* corresponds to values that were not local maxima, but simply the limit of computational testing (deformations failed for B matrix f\*.

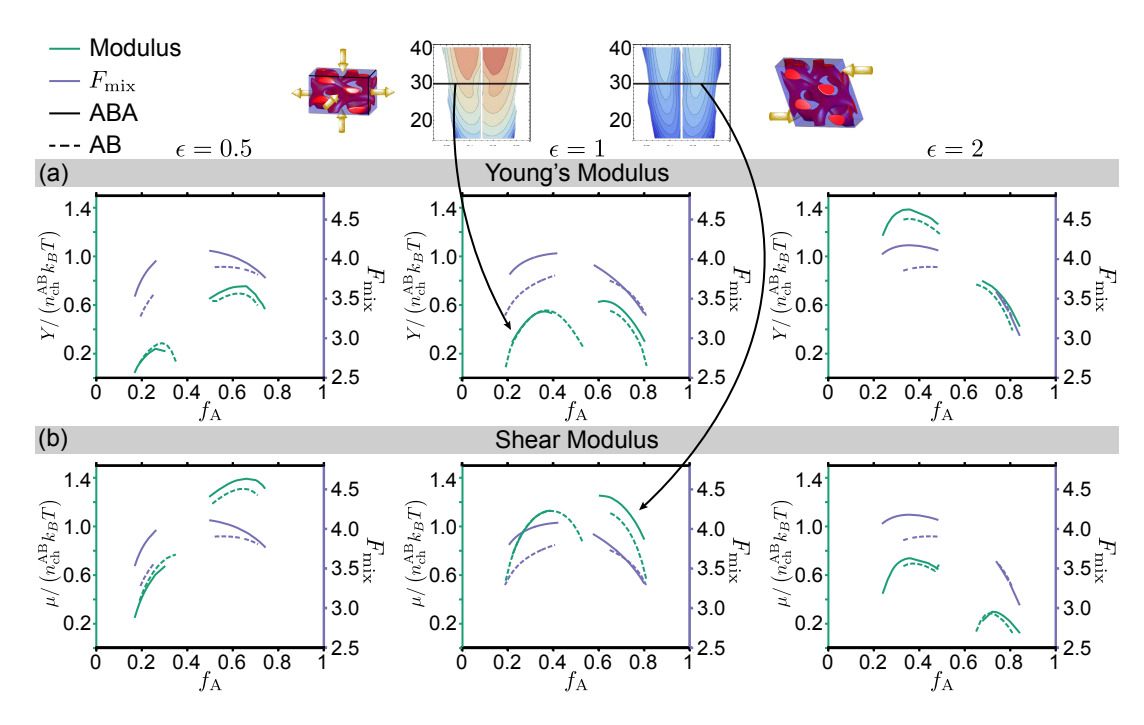


FIG. S18. Plots of (a) Young's modulus and free energy and (b) shear modulus and free energy vs  $f_A$  for  $\chi N^{AB} = 30$  for gyroid phase, comparing ABA and AB.

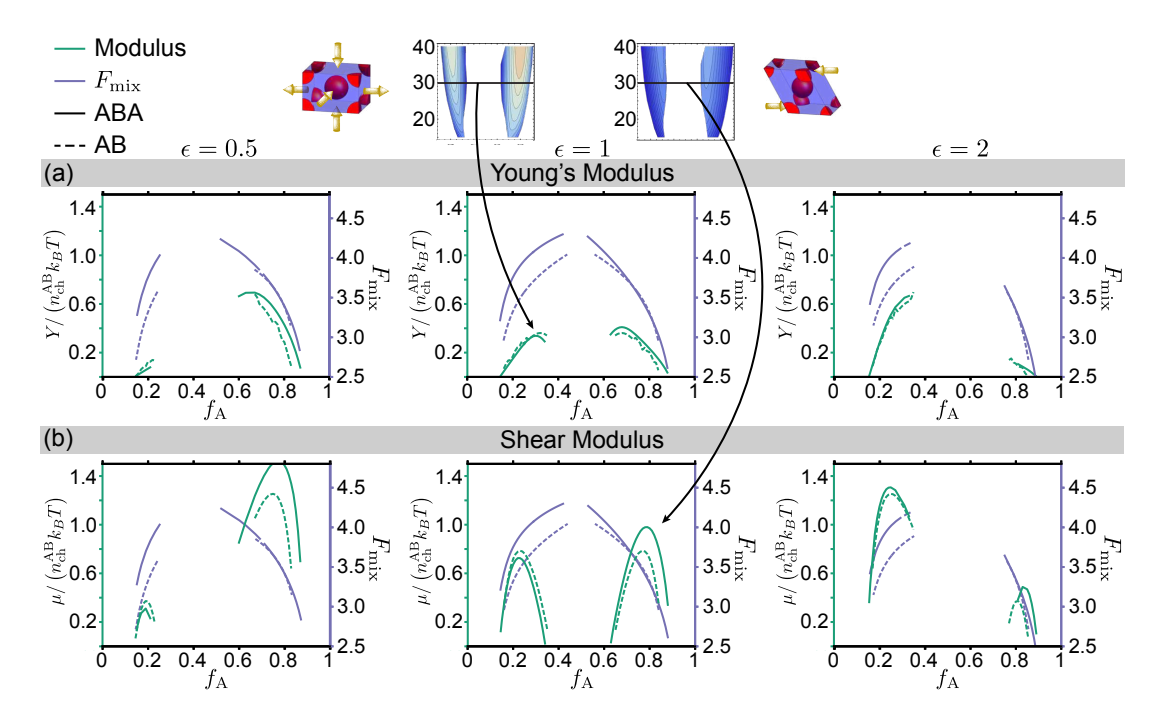


FIG. S19. Plots of (a) Young's modulus and free energy and (b) shear modulus and free energy vs  $f_A$  for  $\chi N^{AB}=30$  for BCC spheres, comparing ABA and AB.

#### S4. STRONG SEGREGATION THEORY CALCULATIONS

The strong segregation theory (SST) free energy is given by

$$F^{\text{SST}} = \gamma A + \frac{1}{2} \kappa_{\text{A}} I_{\text{A}} + \frac{1}{2} \kappa_{\text{B}} I_{\text{B}}$$

where  $\gamma$  is an interfacial free energy density,  $\kappa_{A,B} = (3\pi^2 \rho k_B T)/(4N_{A,B}^2 \ell_{A,B}^2)$  are entropic rigidities, and  $I_{A,B}$  are second moments of volume, corresponding to the geometric dependence of brush stretching from parabolic brush theory [3]. For lamellae, the thickness of the A block brush is  $h_A$  and the thickness of the B block brush is  $h_B$ . Due to incompressibility of the melt, the brush thicknesses is related to the total lamellar thickness h by  $h_A = f_A h$  and  $h_B = (1 - f_A)h$ . The volume of the lamellar structure is given in terms of thickness h = D/2 and cross-section area A by V = AD. Then the second moments of volume are given by

$$I_{A} = \int dV z^{2} = A \int_{0}^{h_{A}} dz z^{2} = \frac{1}{3} A h_{A}^{3} = \frac{1}{24} V f_{A}^{3} D^{2}$$
$$I_{B} = \int dV z^{2} = A \int_{0}^{h_{B}} dz z^{2} = \frac{1}{3} A h_{B}^{3} = \frac{1}{24} V f_{B}^{3} D^{2}$$

The SST free energy of the unit cell is therefore

$$F^{\text{SST}} = 2\gamma A + \frac{1}{24} V \kappa_{\text{A}} f_{\text{A}}^{3} D^{2} + \frac{1}{24} V \kappa_{\text{B}} f_{\text{B}}^{3} D^{2}$$

$$= \frac{2\gamma V}{D} + \frac{V}{24} \left[ \frac{3\pi^{2} \rho k_{\text{B}} T}{4N_{\text{A}}^{2} \ell_{\text{A}}^{2}} f_{\text{A}}^{3} + \frac{3\pi^{2} \rho k_{\text{B}} T}{4N_{\text{B}}^{2} \ell_{\text{B}}^{2}} f_{\text{B}}^{3} \right] D^{2}$$

$$= \frac{2\gamma V}{D} + V \kappa \left[ \frac{f_{\text{A}}}{N \ell_{\text{A}}^{2}} + \frac{f_{\text{B}}}{N \ell_{\text{B}}^{2}} \right] D^{2}$$

where  $\kappa \equiv \frac{\pi^2 \rho k_B T}{32N} = (\pi^2/32) n_{\rm ch} k_B T$ , where  $n_{\rm ch} = \rho/N$  is the chain density. The free energy per volume  $\mathcal{F}^{\rm SST} = F^{\rm SST}/V$  is therefore

$$\mathcal{F}^{\text{SST}} = \frac{2\gamma}{D} + \kappa \left[ \frac{f_{\text{A}}}{N\ell_{\text{A}}^2} + \frac{f_{\text{B}}}{N\ell_{\text{B}}^2} \right] D^2$$

In order to extract the elastic modulus at constant volume, consider the deformation free energy per chain  $\Delta \mathcal{F}^{\text{SST}}$  due to stretching the lamellae  $D \mapsto \lambda D$ , given by

$$\Delta \mathcal{F}^{\text{SST}} = \mathcal{F}^{\text{SST}}(\lambda D) - \mathcal{F}^{\text{SST}}(D)$$
$$= \frac{2\gamma}{D} \left(\frac{1}{\lambda} - 1\right) + \kappa \left[\frac{f_{\text{A}}}{N\ell_{\text{A}}^2} + \frac{f_{\text{B}}}{N\ell_{\text{B}}^2}\right] D^2(\lambda^2 - 1)$$

The elastic modulus  $C_{\parallel}$  is therefore

$$\begin{split} C_{\parallel}^{\rm SST}(D) &= \frac{\mathrm{d}^2 \mathcal{F}^{\rm SST}}{\mathrm{d}\lambda^2} \bigg|_{\lambda=1} \\ &= \frac{4\gamma}{D} + 2\kappa \left[ \frac{f_{\rm A}}{N\ell_{\rm A}^2} + \frac{f_{\rm B}}{N\ell_{\rm B}^2} \right] D^2 \end{split}$$

Now, to determine the rigidity at equilibrium, the equilibrium lamellar spacing is found by minimizing  $\mathcal{F}^{\text{SST}}(D)$  with respect to D:

$$\frac{\mathrm{d}\mathcal{F}^{\mathrm{SST}}}{\mathrm{d}D}\bigg|_{D^*} = 0 = -\frac{2\gamma}{(D^*)^2} + 2\kappa \left[\frac{f_{\mathrm{A}}}{N\ell_{\mathrm{A}}^2} + \frac{f_{\mathrm{B}}}{N\ell_{\mathrm{B}}^2}\right]D^*$$

so

$$D^* = \left(\frac{\gamma}{\kappa} \frac{N}{f_{\rm A} \ell_{\rm A}^{-2} + f_{\rm B} \ell_{\rm B}^{-2}}\right)^{1/3}$$

The equilibrium rigidity is therefore

$$C_{\parallel}^{\text{SST}}(D^{*}) = \frac{4\gamma}{D^{*}} + 2\kappa \left[ \frac{f_{\text{A}}}{N\ell_{\text{A}}^{2}} + \frac{f_{\text{B}}}{N\ell_{\text{B}}^{2}} \right] (D^{*})^{2}$$

$$= 4\gamma \left( \frac{\kappa}{\gamma} \frac{f_{\text{A}}\ell_{\text{A}}^{-2} + f_{\text{B}}\ell_{\text{B}}^{-2}}{N} \right)^{1/3} + 2\kappa \left[ \frac{f_{\text{A}}}{N\ell_{\text{A}}^{2}} + \frac{f_{\text{B}}}{N\ell_{\text{B}}^{2}} \right] \left( \frac{\gamma}{\kappa} \frac{N}{f_{\text{A}}\ell_{\text{A}}^{-2} + f_{\text{B}}\ell_{\text{B}}^{-2}} \right)^{2/3}$$

$$= 6 \left[ \kappa \gamma^{2} \left( \frac{f_{\text{A}}}{N\ell_{\text{A}}^{2}} + \frac{f_{\text{B}}}{N\ell_{\text{B}}^{2}} \right) \right]^{1/3}$$

Note that, following Helfand and Sapse [4, 5] we can express  $\gamma = k_B T \rho \sqrt{\ell_A \ell_B} \sqrt{\chi/6} = n_{\rm ch} k_B T N \sqrt{\ell_A \ell_B} \sqrt{\chi/6}$ , allowing us to re-write the rigidity as

$$C_{\parallel}^{\rm SST}(D^*) = \left(\frac{9\pi^2}{8}\right)^{1/3} (\chi N)^{1/3} n_{\rm ch} k_B T \left[\sqrt{N\ell_{\rm A}^2} \sqrt{N\ell_{\rm B}^2} \left(\frac{f_{\rm A}}{N\ell_{\rm A}^2} + \frac{f_{\rm B}}{N\ell_{\rm B}^2}\right)\right]^{1/3}.$$

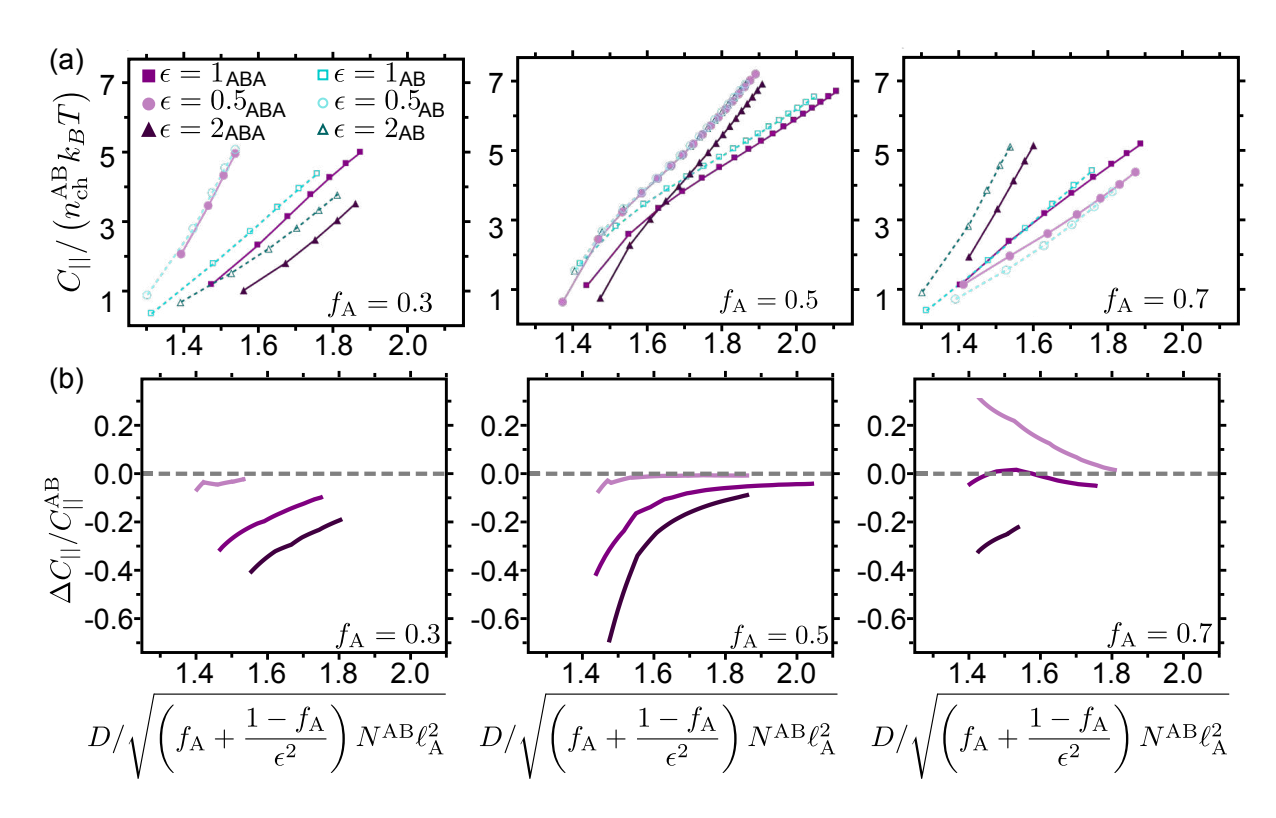


FIG. S20. (a) Plot showing the scaling of longitudinal modulus with domain spacing for lamellae at  $f_{\rm A}=0.3,0.5$ , and 0.7, with domain spacing normalized by  $\epsilon$  and  $f_{\rm A}$ . (b) Plot showing the percent difference between  $C_{||}$  for ABA and AB, where  $\Delta C_{||}=C_{||}^{\rm ABA}-C_{||}^{\rm AB}$ .

#### S5. POLYCRYSTALLINE AVERAGES

Using the Voigt notation for symmetric tensors, we define linear elastic stiffness tensor components  $C_{IJ} = C_{ijkl}$  associated with a given free energy F and deformation u as follows:

$$C_{11} = \frac{\partial^2 F}{\partial u_{xx}^2} \qquad C_{22} = \frac{\partial^2 F}{\partial u_{yy}^2} \qquad C_{33} = \frac{\partial^2 F}{\partial u_{zz}^2} \qquad C_{44} = \frac{\partial^2 F}{\partial u_{xy}^2} \qquad C_{55} = \frac{\partial^2 F}{\partial u_{yz}^2} \qquad C_{66} = \frac{\partial^2 F}{\partial u_{zx}^2}$$

$$C_{12} = C_{21} = \frac{\partial^2 F}{\partial u_{xx} \partial u_{yy}} \qquad C_{23} = C_{32} = \frac{\partial^2 F}{\partial u_{yy} \partial u_{zz}} \qquad C_{13} = C_{31} = \frac{\partial^2 F}{\partial u_{zz} \partial u_{xx}}$$
(S15)

For the following, we note that the lamellar, columnar, and cubic phases can all be regarded as limiting cases of orthorhombic materials. Following the method outlined by Berryman, [6], the Voigt and Reuss averages for overall shear response of orthorhombic systems is given by:

$$G_V = \frac{1}{5} \left[ 2G_{\text{eff}}^v + C_{44} + C_{55} + C_{66} \right] \tag{S16}$$

and

$$\frac{1}{G_R} = \frac{1}{5} \left[ \frac{2}{G_{\text{eff}}^r} + \frac{1}{C_{44}} + \frac{1}{C_{55}} + \frac{1}{C_{66}} \right], \tag{S17}$$

respectively. Here, the effective shear constants for orthorhombic systems can be defined as follows:

$$G_{\text{eff}}^v \equiv \frac{1}{6} \left[ C_{11} + C_{22} + C_{33} - C_{12} - C_{13} - C_{23} \right] \tag{S18}$$

and

$$\frac{3}{G_{\text{eff}}^r} \equiv \frac{2}{\Delta} \left[ C_{11}(C_{22} + C_{33}) + C_{22}(C_{33} + C_{13}) + C_{33}(C_{11} + C_{12}) - C_{13}(C_{13} + C_{12}) - C_{12}(C_{12} + C_{23}) - C_{23}(C_{23} + C_{13}) \right],$$
(S19)

where the factor  $\Delta$  is given by

$$\Delta = C_{11}C_{22}C_{33} + 2C_{12}C_{23}C_{13} - C_{11}C_{23}^2 - C_{22}C_{13}^2 - C_{33}C_{12}^2, \tag{S20}$$

which is the pertinent determinant of the upper left  $3 \times 3$  segment of the elastic constant matrix.

In order to apply these averages to our systems, we need to contend with two complications: (i) certain components  $C_{IJ}$  are zero, which can result in singular evaluations of the above relations; (ii) since volumes are constrained to remain constant, the effective bulk modulus K should be taken to be infinite. To address this, we will regularize both the vanishing moduli and diverging bulk moduli, taking the appropriate limits in the final evaluation.

# A. 1D polycrystals

In the text, we note that under constant volume conditions (tr  $\mathbf{u} = 0$ ), the free energy for the lamellar phase can be written as

$$\Delta \mathcal{F} = \frac{1}{2} C_{||} u_{zz}^2 \,.$$

First, add the ability to change volume back in. To respect the symmetries of the lamellae, we need add in a bulk modulus term K as well as a transverse modulus  $C_{\perp}$ , as

$$\Delta \mathcal{F} = \frac{1}{2} \left[ \left( C_{||} - C_{\perp} \right) u_{zz}^2 + C_{\perp} \left( u_{xx} + u_{yy} \right)^2 + K \left( u_{xx} + u_{yy} + u_{zz} \right)^2 \right] ,$$

where we note that we recover the original form in the limit that  $\operatorname{tr} \mathbf{u} \to 0$ . Note that the volume change will scale as  $\operatorname{tr} \mathbf{u} \sim 1/K$  under a finite pressure, so the  $\operatorname{tr} \mathbf{u} \to 0$  condition can be obtained in the  $K \to \infty$  limit.

Let us re-write this as an orthorhombic system:

$$\Delta \mathcal{F} = \frac{1}{2} \left[ C_{11} u_{xx}^2 + C_{22} u_{yy}^2 + C_{33} u_{yy}^2 + 2C_{12} u_{xx} u_{yy} + 2C_{23} u_{yy} u_{zz} + 2C_{31} u_{zz} u_{xx} + C_{44} u_{xy}^2 + C_{55} u_{yz}^2 + C_{66} u_{zx}^2 \right]$$

Matching coefficients, we find

$$\begin{split} C_{11} &= C_{\perp} + K \\ C_{22} &= C_{\perp} + K \\ C_{33} &= C_{\parallel} - C_{\perp} + K \\ C_{12} &= C_{\perp} + K + \varepsilon \\ C_{23} &= K \\ C_{31} &= K \\ C_{44} &= C_{55} = C_{66} = \delta \end{split}$$

where we have introduced constants  $\varepsilon$  and  $\delta$  as regularizing constants, such that the correct coefficient relations are found in the limit  $\varepsilon, \delta \to 0$ . Now, we evaluate the terms needed to compute the polycrystalline averages:

$$\begin{split} G_{\text{eff}}^v &= \frac{1}{6} \left( C_{\parallel} - \varepsilon \right) \\ G_V &= \frac{1}{15} \left( C_{\parallel} + 9\delta - \varepsilon \right) \\ \Delta &= 2 (C_{\perp}^2 - KC_{\parallel} - C_{\parallel}C_{\perp})\varepsilon + \mathcal{O}(\varepsilon^2) \\ G_{\text{eff}}^r &= \frac{-3 (C_{\perp}^2 - KC_{\parallel} - C_{\parallel}C_{\perp}^2)}{KC_{\perp} - 4KC_{\parallel} + 4C_{\perp}^2 - 4C_{\perp}C_{\parallel}}\varepsilon + \mathcal{O}(\varepsilon^2) \\ G_R &= \frac{-15 (C_{\perp}^2 - KC_{\parallel} - C_{\parallel}C_{\perp}^2)}{2KC_{\perp} - 8 (KC_{\parallel} - C_{\perp}^2 + C_{\perp}C_{\parallel})}\varepsilon + \mathcal{O}(\varepsilon^2) \end{split}$$

Note that the  $K \to \infty$  limit gives finite results for  $G_V$  and  $G_R$ . Finally, taking the  $\varepsilon, \delta \to 0$  limits, we find

$$G_V = \frac{1}{15}C_{\parallel}$$

$$G_R = 0$$
(S21)

### B. 2D polycrystals

The energy for 2D hexagonal cylinders is given by

$$\Delta \mathcal{F} = \frac{1}{2} \left[ 2\mu_{\perp} (u_{xx}^2 + u_{yy}^2 + 2u_{xy}u_{yx}) + \lambda_{\perp} (u_{xx} + u_{yy})^2 \right]$$
 (S22)

Once again, we modify this form by adding in terms that should disappear as  $\operatorname{tr} \mathbf{u} \to 0$ :

$$\Delta \mathcal{F} = \frac{1}{2} \left[ 2\mu_{\perp} (u_{xx}^2 + u_{yy}^2 + 2u_{xy}u_{yx}) + \eta u_{zz}^2 + (\lambda_{\perp} - \eta) (u_{xx} + u_{yy})^2 + K (u_{xx} + u_{yy} + u_{zz})^2 \right]$$

where K is the bulk modulus and  $\eta$  describes the stiffness along the z-axis. Matching coefficients, we find

$$\begin{split} C_{11} &= 2\mu_{\perp} + \lambda_{\perp} - \eta + K \\ C_{22} &= 2\mu_{\perp} + \lambda_{\perp} - \eta + K \\ C_{33} &= \eta + K \\ C_{12} &= 2\mu_{\perp} + \lambda_{\perp} - \eta + K + \varepsilon \\ C_{23} &= K \\ C_{31} &= K \\ C_{44} &= 4\mu_{\perp} \\ C_{55} &= C_{66} = \delta \end{split}$$

Now, we evaluate the terms needed to compute the polycrystalline averages:

$$\begin{split} G^v_{\text{eff}} &= \frac{1}{6} \left( 2\mu_\perp + \lambda_\perp - \varepsilon \right) \\ G_V &= \frac{1}{15} \left( 14\mu_\perp + \lambda_\perp - \varepsilon + 6\delta \right) \\ \Delta &= 2 \left( \left( \eta - 2\mu_\perp - \lambda_\perp \right) \eta - \left( 2\mu_\perp + \lambda_\perp \right) K \right) \varepsilon + \mathcal{O}(\varepsilon^2) \\ G^r_{\text{eff}} &= -\frac{3 \left( (2\mu_\perp + \lambda_\perp) (\eta + K) - \eta^2 \right)}{4 (2\mu_\perp + \lambda_\perp - \eta) \eta + \left( 3 (2\mu_\perp + \lambda_\perp) + \eta \right) K} \varepsilon + \mathcal{O}(\varepsilon^2) \\ G_R &= -\frac{15 \left( (2\mu_\perp + \lambda_\perp) (\eta + K) - \eta^2 \right)}{8 (2\mu_\perp + \lambda_\perp - \eta) \eta + 2 \left( 3 (2\mu_\perp + \lambda_\perp) + \eta \right) K} \varepsilon + \mathcal{O}(\varepsilon^2) \end{split}$$

Note that the  $K \to \infty$  limit gives finite results for  $G_V$  and  $G_R$ . Finally, taking the  $\varepsilon, \delta \to 0$  limits, we find

$$G_V = \frac{1}{15} \left( 14\mu_{\perp} + \lambda_{\perp} \right) = \frac{1}{15} \left( 13\mu_{\perp} + Y_{\parallel} \right)$$

$$G_R = 0$$
(S23)

# C. 3D polycrystals

The free energy per volume for cubic systems is given by

$$\Delta \mathcal{F} = \frac{Y}{9} \left( (u_{xx} - u_{yy})^2 + (u_{yy} - u_{zz})^2 + (u_{zz} - u_{xx})^2 \right) + 2\mu \left( u_{xy} u_{yx} + u_{yz} u_{zy} + u_{zx} u_{xz} \right) + \frac{1}{2} K (u_{xx} + u_{yy} + u_{zz})^2 ,$$
(S24)

which we extend to include a bulk rigidity. Matching coefficients, we find

$$C_{11} = C_{22} = C_{33} = \frac{4}{9}Y + K$$

$$C_{12} = C_{23} = C_{31} = -\frac{2}{9}Y + K$$

$$C_{44} = C_{55} = C_{66} = 4\mu$$

Now, we evaluate the terms needed to compute the polycrystalline averages:

$$G_{\text{eff}}^{v} = \frac{1}{3}Y$$

$$G_{V} = \frac{2}{15} (18\mu + Y)$$

$$\Delta = \frac{4}{3}Y^{2}K$$

$$G_{\text{eff}}^{r} = \frac{27YK}{4Y + 90K}$$

$$G_{R} = \frac{540\mu YK}{32\mu Y + 9(80\mu + 9Y)K}$$

Taking the  $K \to \infty$  limit, we find

$$G_V = \frac{2}{15} (18\mu + Y)$$

$$G_R = \frac{60\mu Y}{80\mu + 9Y}$$
(S25)

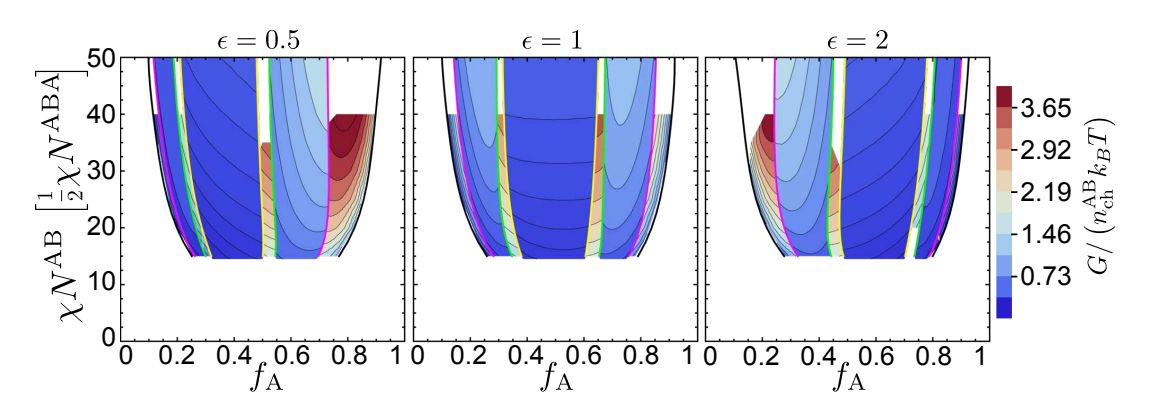


FIG. S21. Heat map of Voigt (upper) modulus bounds for each  $\epsilon$ .

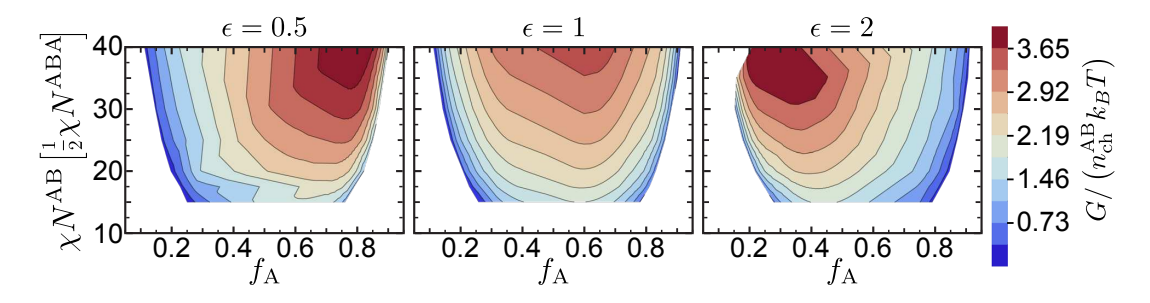


FIG. S22. Convex hull for each  $\epsilon$ .

#### S6. POLYMER BRIDGING CALCULATIONS

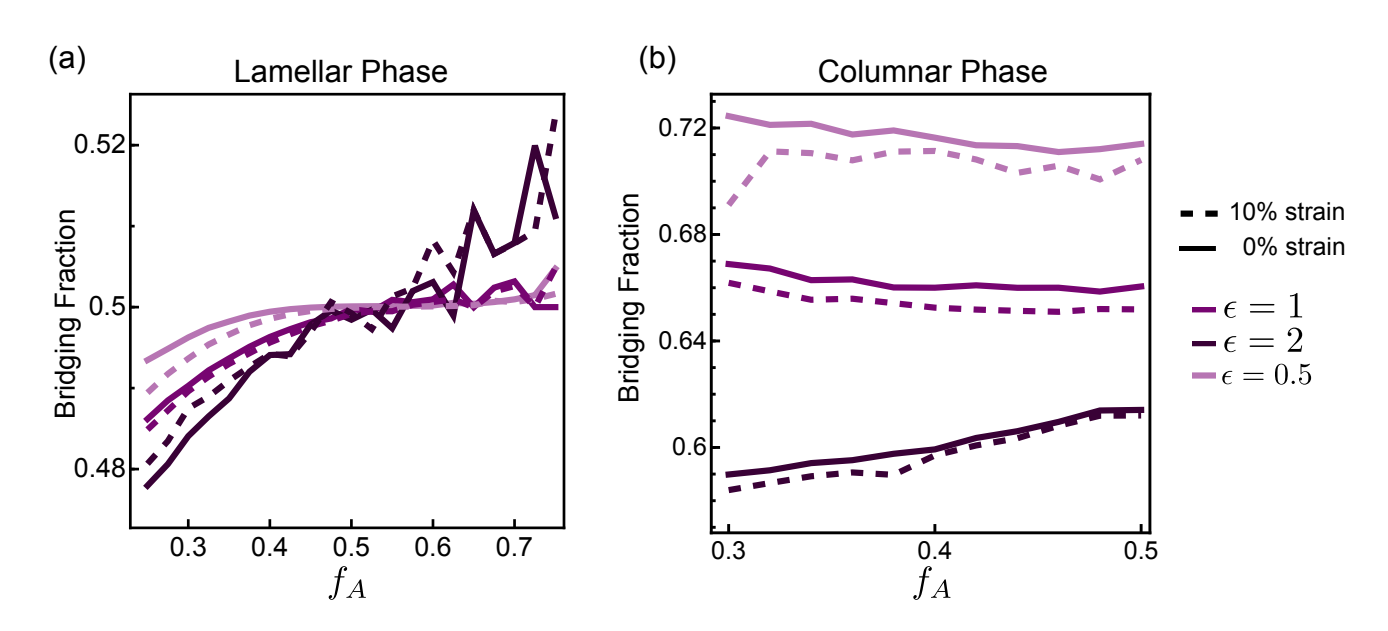


FIG. S23. Bridging fractions for ABA triblocks for lamellar and columnar phases.

In ABA triblock copolymers, we quantify the fraction of bridging chains following a standard chain propagator framework [7]. For each parameter set  $(f_A, \epsilon, \chi N)$ , we first obtain the self-consistent chemical potential fields  $\omega_A(r)$ ,  $\omega_B(r)$  using SCFT. We then compute the forward and backward single chain propagators q(r,s) and  $q^{\dagger}(r,s)$  by integrating the modified diffusion equation along the contour length  $s \in [0,1]$ ,

$$\partial_s q(r,s) = \frac{l_{j(s)}^2}{6} \nabla^2 q(r,s) - w_{j(s)}(r) q(r,s),$$
 (S26)

$$-\partial_{s} q^{\dagger}(r,s) = \frac{l_{j(s)}^{2}}{6} \nabla^{2} q^{\dagger}(r,s) - w_{j(s)}(r) q^{\dagger}(r,s)$$
 (S27)

with initial/terminal conditions q(r,0) = 1 and  $q^{\dagger}(r,1) = 1$ . The block label  $j(s) \in \{A,B\}$  is defined as,

$$j(s) = \begin{cases} B, & f_1 \le s \le f_2 \\ A, & \text{otherwise} \end{cases}$$

Here  $f_1$  and  $f_2$  are the contour length coordinates of the B-block entry and exit respectively, with  $0 < f_1 < f_2 < 1$ . With Q as the single chain partition function, the segment probability density is defined as,

$$\rho(r,s) = \frac{q(r,s)q^{\dagger}(r,s)}{Q} \tag{S28}$$

Now, to further resolve these chains as looping or bridging, we focus on the B block, i.e.  $s \in [f1, f2]$ , that spans the midblock. Starting from the B-block entrance (s=f1), we construct a function  $\bar{q}(r,s)$  as follows,

$$\bar{q}(r,s) = q(r,f_1); r \in 1^{\text{st}} \text{ unit cell,}$$
 (S29)

and 0 elsewhere. We propagate this function using the same modified diffusion equation (S26) from  $s = f_1$  to  $s = f_2$ , but with Neumann boundary conditions at the ends of the domain. We can therefore calculate the distribution  $\bar{\rho}(r,s)$ at the end of the B block domain by

$$\bar{\rho}(r, f_2) = \frac{\bar{q}(r, f_2)q^{\dagger}(r, f_2)}{Q}$$
 (S30)

The looping fraction  $\nu_L$  can be calculated by integrating  $\bar{\rho}(r, f_2)$  over the unit cell, i.e. chains that left the A domain, traversed the B block, and returned back to the same A domain:

$$\nu_L = \int_{\Omega_{\text{cell}}} \bar{\rho}(r, f_2) dr,$$
and 
$$\nu_B = 1 - \nu_L$$
(S31)

and 
$$\nu_B = 1 - \nu_L$$
 (S32)

Here,  $\nu_B$  is the bridging fraction. The bridging fractions for lamellar and columnar phases for a range of A-block fractions  $(f_A)$  are reported in Figure S23.

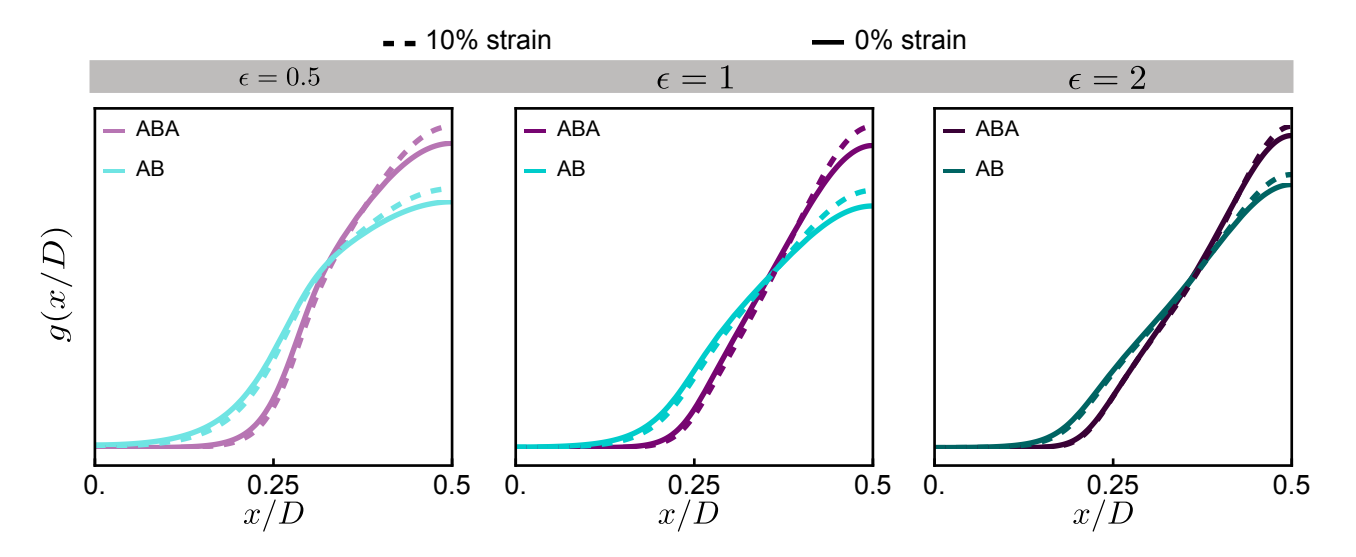


FIG. S24. Normalized segment distributions over half lamellar unit cell, for ABA (mid-chain segment in B) and AB (end chain segment in B), shown in the undeformed state (solid, 0% strain) and the deformed (dashed, 10% strain) for each  $\epsilon$ .

To further probe how the chain segments rearrange with strain, we evaluate the spatial profile of a single chain using these propagators. For a chosen contour position  $s^*$ , we normalize the segment probability density over one unit cell (domain size D) to obtain the distribution of the chain segment  $s^*$ ,

$$g(x/D) = \frac{\rho(x, s^*)}{\int_0^D \rho(x, s^*) dx},$$
 (S33)

so that  $\int_0^1 g(x/D) dx = 1$ . For AB diblocks we evaluate the chain end segment in the B domain  $(s^* = 1)$ , whereas for ABA triblocks we pick the mid-chain segment ( $s^* = 0.5$ ) of the B-block. For each  $\epsilon$ , we plot the undeformed (0%) strain) and deformed (10% strain) profiles, and compare the AB and ABA on the same axis (see Figure S24).

#### REFERENCES

[1] M. Rubinstein and R. H. Colby, Ideal chains, in *Polymer Physics* (Oxford University Press, 2003) 1st ed., pp. 49–96.

- [2] A. Arora, J. Qin, D. C. Morse, K. T. Delaney, G. H. Fredrickson, F. S. Bates, and K. D. Dorfman, Broadly accessible self-consistent field theory for block polymer materials discovery, Macromolecules 49, 4675 (2016).
- [3] S. T. Milner, T. A. Witten, and M. E. Cates, Theory of the grafted polymer brush, Macromolecules 21, 2610 (1988).
- [4] E. Helfand, Theory of inhomogeneous polymers: Fundamentals of the gaussian random-walk model, The Journal of Chemical Physics **62**, 999 (1975).
- [5] E. Helfand and A. M. Sapse, Theory of unsymmetric polymer–polymer interfaces, The Journal of Chemical Physics 62, 1327 (1975).
- [6] J. G. Berryman, Bounds and self-consistent estimates for elastic constants of polycrystals composed of orthorhombics or crystals with higher symmetries, Physical Review E 83, 10.1103/physreve.83.046130 (2011).
- [7] M. W. Matsen and R. B. Thompson, Equilibrium behavior of symmetric ABA triblock copolymer melts, The Journal of Chemical Physics 111, 7139 (1999).